Spatiotemporal metabolic organization during development of brain cell cultures

Dissertation

zur Erlangung des akademischen Grades

doctor rerum naturalium

(Dr. rer. nat.)

genehmigt durch die Fakultät für Naturwissenschaften

der Otto-von-Guericke-Universität Magdeburg

von   **M.Sc. Jiraporn Luengviriya**

geb. am   13.08.1972   in   Suphanburi, Thailand

Gutachter: Prof. Dr. Marcus Hauser

Prof. Dr. Wolfgang Hanke

eingereicht am: 28.10.2008

verteidigt am: 26.02.2009

In the loving memories of my mother

who has done all for me throughout her life

. . . long gone but never forgotten

Acknowledgements

Abstract

The brain requires a large amount of energy for proper functioning, thereby an increase of neuronal communication is constrains due to limited energy supply. This problem may be circumvented by optimizing the neuronal connection instead of increasing the number of neurons. Such a fine reorganization of the neuronal network is established during early postnatal brain development.

In this thesis, the developmental changes of the energy metabolism during neuronal network development have been investigated in order to get deeper insight into the impact of the energy metabolism for optimization of neuronal communication. Hippocampal cell cultures, containing both neurons and glia cells, were incubated in nutrition medium for the first three weeks *in vitro*. In this interval, the energy metabolism during neuronal network formation in rat hippocampal cell cultures has been studied by means of fluorescence imaging together with chemical stimulation. NAD(P)H and intracellular protons have been taken as a measure for the energy metabolism because they are produced by glycolysis and subsequently consumed by mitrocondrial respiration. NAD(P)H was recorded by its autofluorescent and protons were detected by using a suitable fluorescent pH-indicator dye.

Developmental changes of the energy metabolism were investigated. This process was traced by recording NAD(P)H fluorescence in response to NMDA-induced activation of neuronal activity. We observed progressive changes of stimulation evoked NAD(P)H signaling during the first three weeks *in vitro*. At day 7 and 16, this response was minimal, yielding a biphasic pattern that reproduced earlier findings of about developmental changes of population spike (a shift in electrical

potential as a consequence of the movement of ions involved in the generation and propagation of action potentials) amplitudes or glutamate release in young rats. Inhibition of mitochondrial respiration by KCN revealed that the NMDA-evoked stimulation of the energy metabolism is mainly due to an increase in glycolytic activity.

Imaging of intracellular pH (pH_i) revealed traveling proton waves which induced by blocking mitochondrial respiration with cyanide. These waves were accompanied by network oscillations in pH_i. During the observation period (3-22 day *in vitro* (DIV)), most of the observed cells showed a biphasic response which are characterized by an initial acid shift and subsequent alkalinization. It was during this alkalinization period that concomitant waves and network oscillations could be observed, however, only after 14 DIV. NMDA induced similar changes in pH_i except that propagating waves could not be observed. Our results indicate that the energy metabolism of hippocampal cells undergoes age-dependent dynamic instabilities leading to the formation of traveling proton waves.

Zusammenfassung

Das Gehirn benötigt für eine fehlerfreie Funktion einen großen Energieumsatz, wodurch eine Vergrößerung der neuronalen Kommunikation, allein schon durch die begrenzt Energiezufuhr, beschränkt wird. Dieses Problem kann durch eine Optimierung neuronaler Verbindungen, anstelle einer Zunahme von Neuronen, umgangen werden. Solch eine Reorganisation neuronaler Verbindungen findet während der frühen postnatalen Entwicklung des Gehirns statt.

In dieser Doktorarbeit wurden entwicklungsabhängige Änderungen des Energiestoffwechsels während der Ausbildung neuronaler Netzwerke untersucht, um tiefere Einblicke in die Bedeutung des Energiestoffwechsels für die Optimierung neuronaler Kommunikation zu erhalten. Hippokampale Zellkulturen neugeborener Ratten, welche Neuronen und Gliazellen enthielten, wurden in Nährmedium für 3 Wochen inkubiert. In dieser Zeit wurde der Energiestoffwechsel dieser Zellkulturen während der Ausbildung neuronaler Netzwerke durch Fluoreszenzmessungen verfolgt. Gleichzeitig erfolgte eine chemische Stimulierung der Zellen. Als Indikatoren für den Energiestoffwechsel wurden NAD(P)H und intrazelluläre Protonen gemessen, da diese während der Glykolyse produziert und NAD(P)H anschließend während der mitochondrialen Atmung wieder zu NAD(P)$^+$ oxidiert wird. NAD(P)H wurde über dessen Autofluoreszenz gemessen wohingegen zum Nachweis intrazellulärer Protonen (pH_i) ein pH-Indikator verwendet wurde.

Es wurden entwicklungsabhängige Änderungen des Energiestoffwechsels untersucht. Hierzu wurde durch Zugabe von NMDA eine neuronale Aktivität ausgelöst und die Antwort der Zellen mittels NAD(P)H-Fluoreszenz verfolgt. Es konnten progressive Änderungen der NMDA-evozierten Signale während der ersten drei

Wochen *in vitro* beobachtet werden. Dabei traten zwei Minima auf, am 7. Tag *in vitro* (DIV) und am 16 DIV, wodurch ein biphasischer Verlauf entstand, der frühere Messungen anderer Gruppen über den entwicklungsabhängigen Verlauf von Populations-Spike (d.h. eine Änderung des elektrischen Potentials als Folge der Bewegung von Ionen, die an der Entstchung und Propagation von Aktios-potentialen beteiligt sind) Amplituden oder Glutamat Freisetzung in neugeborenen Ratten reproduzierte. Versuche zur Inhibierung der mitochondrialen Atmung durch Kaliumcyanid ergaben, dass die NMDA-evozierte Stimulierung des Energiestoffwechsels hauptsächlich auf die Glykolyse zurück zu führen ist.

Durch Visualisierung des intrazellulären pH-Wertes konnten wandernde Protonenwellen nachgewiesen werden. Diese Wellen wurden durch Inhibierung der mitochondrialen Respiration durch Kaliumcyanid induziert. Gleichzeitig mit diesen Wellen traten auch Netzwerkoszillationen des pH_i auf. Während des Beobachtungszeitraumes (3 DIV-22 DIV) zeigten die meisten Zellen eine biphasische Antwort auf eine Kaliumcyanid-Zugabe. Diese war durch eine anfängliche Ansäuerung und eine nachfolgende Alkalisierung charakterisiert. Die Wellen und Netzwerkoszillationen traten während der Alkalisierungsphase auf, allerdings erst nach dem 14 DIV. NMDA induzierte ähnliche Änderungen im pH_i, mit Ausnahme der Entstehung von Wellen und Netzwerkoszillationen. Die Ergebnisse dieser Arbeit zeigen, dass der Energiestoffwechsel hippokampaler Zellkulturen neugeborener Ratten entwicklungsabhängige Änderungen durchläuft, die zu dynamischen Instabilitäten in Form von wandernden Protonenwellen und Netzwerkoszillationen führen.

Contents

List of Figures

Abbreviations

AMP	Adenosine monophosphate
ADP	Adenosine diphosphate
ATP	Adenosine triphosphate
ATPase	Adenosine triphosphatase
AMPA	Alpha-amino-3-hydroxy-5-methyl-4-isoxazolepropionic acid
ANOVA	Analysis of variance
CNQX	6-cyano-7-nitroquinoxaline-2,3-dione
CoASH	Coenzyme A
D-AP5	D(-)-2-amino-5-phosphonopentanoic acid
DMEM	Dulbecco's Modified Eagle Medium
DIV	Day *in vitro*
EPSP	Excitatory postsynaptic potential
EtOH	Ethanol
FAD	Flavin adenine dinucleotide (oxidized form)
FADH$_2$	Flavin adenine dinucleotide (reduced form)
GDP	Guanosine diphosphate
GTP	Guanosine triphosphate
HEPES	N-2-Hydroxyethylpiperazine-N-2-ethanesulfonic acid
KA	Kainate
LTP	Long term potential
NAD$^+$	Nicotinamide adenine dinucleotide (oxidized form)
NADH	Nicotinamide adenine dinucleotide (reduced form)
NADPH	Nicotinamide adenine dinucleotide phosphate (reduced form)
NAD(P)H	NADH+NADPH
NMDA	N-Methyl-D-aspartic acid
PFK	Phosphofructokinase
P$_i$	Inorganic phosphate
pH$_i$	Intracellular pH
PS	Population spike
PN	Postnatal day
SNARF-AM	Seminaphthorhodafluor Acetoxymethyl
TCA	Tricarboxylic acid cycle

Chapter 1

Introduction and goals

"Even at rest life is hard work" was pointed out by Ivanov in 1972: In a rest state, a human spends about 1.4 W/kg of energy or 1800 kcal/day [1].

Energy is undoubtfully essential for all of living organisms. They need energy for their activity, producing new cellular materials, maintaining the organization of membranes and organelles, and fueling movement and active transport. As thermodynamically open systems maintaining their nonequilibrium conditions, living organisms consume nutrients to produce the energy storage molecule ATP (adenosine triphosphate) via the energy metabolism which is categorized as glycolysis and respiration.

The brain requires a large amount of energy for proper functioning, typically 2% to 10% of the resting energy in animals [2]. Based on experimental findings and theoretical considerations, it has been suggested that neuronal communication is constrained by the energy supply to the brain [3]. This limitation implies that an increase in neuronal communication requires optimizing the efficiency of the neuronal network wiring instead of increasing the number of neurons. Such fine-tuning of neuronal networks is established during early postnatal brain development. Depending on the brain compartment, this process involves sensory, motor, cognitive and emotional learning events which induce the reorganization of the network architecture [4]. Since neuronal activity leads to an increased demand

for metabolic energy, it can be concluded that the energy metabolism also plays an important role for the development of neuronal networks.

The brain is an organ with a large capacity of information processing, usually accomplished by synaptic transmission of electrical signals. Due to this increased requirement for information processing, self-organized patterns may also occur in the brain. In fact, such patterns have been found, for example, as circular or spiral shaped calcium waves [5].

Spatiotemporal pattern formation, based on the principles of self-organization, is a property of biological systems which can result from the coupling of an autocatalytic reaction with diffusion. Examples for either intracellular or intercellular pattern formation of calcium in *Xenopus laevis* oocytes [6], AMP (adenosine monophosphate) in a colony of the slime mold *Dictyostelium discoideum* [7], ATP in retinal astrocytes [8], protons [9, 10] or NADH (Nicotinamide adenine dinucleotide) [9–11] in yeast extracts have been reported. Self-organization is a universal system property and hence not restricted to biological systems. Results from chemical and physical systems demonstrated that the pattern dynamics contained information about the state of systems [12–16]. Accordingly, such patterns may provide route for biological information processing, as has been already demonstrated for the life cycle of the slime mold *Dictyostelium discoideum* [7] or the electrical excitation of the heart muscle [17–19].

A local excitation of brain slices from the hippocampus, either by chemical or electrical stimulation, has been shown to evoke propagating NAD(P)H signals [20–22], i.e., a stimulation of the energy metabolism. This type of spatiotemporal dynamics of the energy metabolism in the brain is supported by the concept of metabolic compartmentation [23, 24]. It denotes the fact that most of the glycolytic activity occurs in glia cells, whereas the neurons are more active in respiration. The flow of energy between the two cell types is mediated by lactate. Activation of neurons stimulates glycolysis in the glia cells with concomitant increased extrusion of lactate. Such an energetic flow on demand may be well suited to support the formation of traveling waves of the energy metabolism. We would expect this type of pattern formation to occur especially in developing neuronal networks because

there the requirement for structure formation can be well supported by the organizing principles of self-organization. Since structure formation is associated with the need for energy, self-organized patterns of the energy metabolism, as they have been already demonstrated in neutrophil cells [10] or in yeast extract [9, 11], are good candidates for such patterns.

In this thesis we present research on the energy metabolism during neuronal network formation. We used primary hippocampal cell cultures from newborn rats and recorded the fluorescence of NAD(P)H, which is a common indicator of glycolytic and mitochondrial activity [25–27] during the first 3 weeks *in vitro*. Previously it has been shown that NAD(P)H waves are associated with proton waves [9, 10]. Therefore, we also observed the fluorescence of protons by using the SNARF dye as a fluorescing pH indicator, because the quantum yield of such a dye is markedly larger than that of NAD(P)H, i.e., fluorescence microscopy is facilitated. The rat hippocampal cell cultures were stimulated by evoking the neuronal activity with the neurotransmitter NMDA (N-Methyl-D-aspartic acid) and blocking mitochondrial respiration with cyanide.

This thesis is organized as follows. In Chapter 2, we introduce glycolysis and compartmentation of the metabolism in brain cells. Spatiotemporal dynamics in excitable media are briefly described in Chapter 3, whereas the basics of fluorescence spectroscopy and fluorescent pH indicators are presented in Chapter 4. Chapter 5 describes the experimental methods as well as data evaluation. The results and their discussion are presented in Chapter 6, while Chapter 7 provides some conclusions and future perspectives.

Chapter 2

Metabolism and Brain cells

2.1 Main metabolic pathways

Metabolic pathways are composed of a series of biochemical reactions that are connected by their intermediates: the reactants (or substrates) of one reaction are the products of the previous one, and so on. The main metabolism can be classified as following:

2.1.1 Glycolysis

Glycolysis is the primary pathway for generation of energy in living cells. It is the sequence of reactions which converts one molecule of glucose into two molecules of pyruvate with the concomitant net production of two molecules of adenosine triphosphate (ATP). Two molecules of NADH and proton are also produced. The overall reaction can be expressed as follows Eq. (2.1)

$$
\begin{aligned}
\text{Glucose} + 2\text{ADP} + 2\text{P}_i \quad &\rightarrow \quad 2\text{Pyruvate} + 2\text{ATP} + 2\text{NADH} \\
+2\text{NAD}^+ \quad &\quad +2\text{H}^+ + 2\text{H}_2\text{O}
\end{aligned}
\tag{2.1}
$$
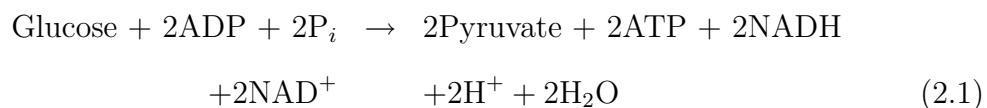
Both aerobic and anaerobic organisms use glycolysis to break down glucose as first step of their energy metabolism.Note that glycolysis itself is anaerobic, in that oxygen is not required. The pathway of glycolysis is presented in Figure 2.1.
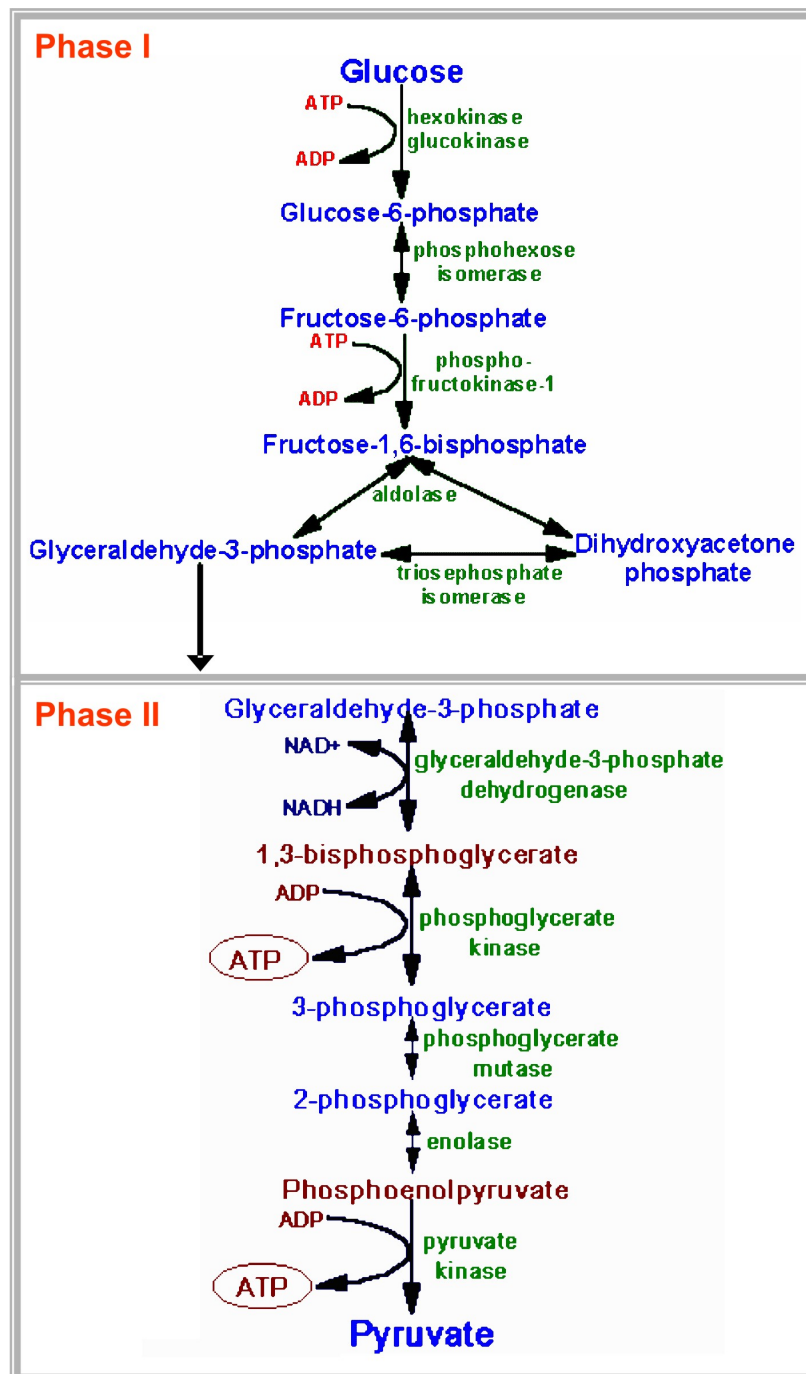
Figure 2.1: Pathway of glycolysis from glucose to pyruvate. It can be seen as consisting of 2 separate phases. In the first phase, 2 equivalents of ATP are used to convert glucose to fructose-1,6-bisphosphate (F-1,6-BP). In the second phase F-1,6-BP is degraded to pyruvate, with the production of 4 equivalents of ATP and 2 equivalents of NADH [28].

2.1.2 Fermentation and anaerobic respiration

If oxygen is absent, many cells are still able to use glycolysis to produce ATP. Two ways this can be done are through fermentation and anaerobic respiration.

Fermentation is the process by which the electrons and hydrogen ions from the NADH produced by glycolysis are donated to another organic molecule. Two of the most common types of fermentation are alcoholic fermentation and lactic acid fermentation. Alcoholic fermentation is common in bacteria and yeast cells. This fermentation leads to the formation of ethanol and CO_2 Eq. (2.2). Once the NADH has been oxidized, glycolysis can continue.

$$\text{Pyruvate} + \text{NADH} + 2\text{H}^+ \quad \rightarrow \quad \text{EtOH} + \text{CO}_2 + \text{NAD}^+ \qquad (2.2)$$

In lactic acid fermentation, pyruvic acid is converted to lactic acid. This reaction is carried out by lactate dehydrogenase, (LDH) Eq. (2.3). The conversion of pyruvate to lactate regenerates NAD^+, which allows glycolysis to continue. Lactic acid is a common by product of fermentation in muscle cells and also in some bacteria.

$$\text{Pyruvate} + \text{NADH} + 2\text{H}^+ \quad \rightarrow \quad \text{Lactate} + \text{CO}_2 + \text{NAD}^+ \qquad (2.3)$$

Note that fermentation does not yield more energy than that already obtained from glycolysis (2 ATPs) but serves to regenerate NAD^+ so glycolysis can continue.

2.1.3 Aerobic respiration

Aerobic respiration takes place in the stages which are summarized in the following (Fig.2.2). In the presence of oxygen, pyruvate which was produced by glycolysis in the cytoplasm will be converted to acetyl Coenzyme A via pyruvate dehydrogenase reaction Eq. (2.4)

$$\text{pyruvate} + \text{NAD}^+ + \text{CoASH} \quad \rightarrow \quad acet\text{-CoA} + \text{NADH} + \text{H}^+ + \text{CO}_2 \quad (2.4)$$

NADH is also produced by this process. Acetyl Coenzyme A then enters into
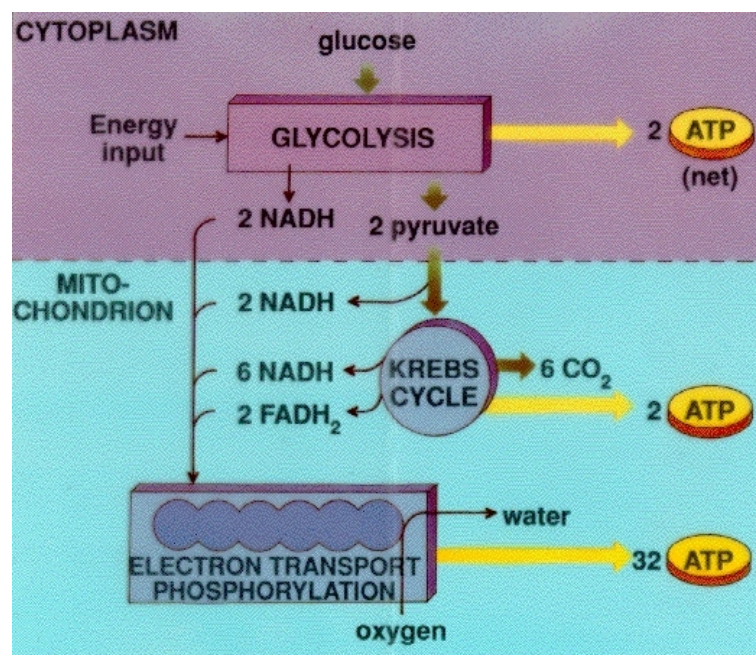
Figure 2.2: Stages in aerobic respiration. Glucose will be converted to pyruvate with the concurrent production of two ATP in glycolysis. From this process, Two molecules of NADH and proton are also produced. Pyruvate will be coverted to acetyl co A before enter into Krebs cycle. This process will produce NADH, proton, $FADH_2$ and ATP. All of NADH and $FADH_2$ are inputs of electron transport chain which use O_2 to produce a large amount of ATP [28].

the Krebs cycle inside the mitochondrial matrix for complete oxidation to CO_2 and H_2O. This process will produce very little energy storing molecules (in the form of guanosine triphosphate (GTP)) directly, but will generate many molecules of reduced coenzymes NAD^+ and FAD as NADH and $FADH_2$. The overall reaction is: Eq. (2.5).

$$\text{Acetyl-Co A} + 3\ NAD^+ + FAD \quad \rightarrow \quad \text{CoASH} + 3\ NADH + FADH_2$$
$$+\ GDP + P_i + 2H_2O \qquad +\ GTP + 2CO_2 + 3H^+ \qquad (2.5)$$
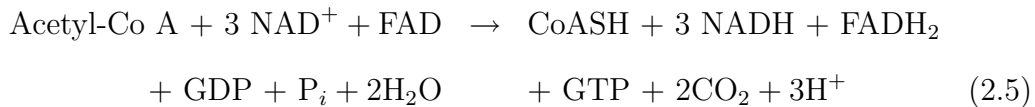
Because glycolysis produces two pyruvate molecules per molecule glucose, each glucose is processed through the Krebs cycle twice. For each molecule of glucose, six NADH, two $FADH_2$, and two ATP are produced. NADH and $FADH_2$ can be used by the electron transport chain to produce further ATP as part of oxidative phosphorylation. This oxidative phosphorylation is the major source of ATP in aerobic organisms. NADH and $FADH_2$ which are produced in glycolysis and Krebs cycle contain a pair of electrons having a high transfer potential. The flow of electrons from NADH or $FADH_2$ to O_2 through protein complexes located in the mitochondrial inner membrane leads to the pumping of protons out of the mitochondrial matrix. Protons enter back into the mitochondrial matrix through channels in ATP synthase enzyme complex. This entry is coupled to ATP synthesis from ADP and phosphate (P_i) as Eq. (2.6)

$$ADP + P_i \quad \rightarrow \quad ATP \qquad (2.6)$$

2.2 Metabolic compartmentation in brain cells

The nervous system consists of two types of cells: the neurons, which are responsible for signal propagation and information processing and glial cells, which exist in between neurons [29]. Based on experimental findings and theoretical considerations it has been suggested that neuronal communication is constrained by the energy supply to the brain [3]. A type of glial cells, with a supporting role
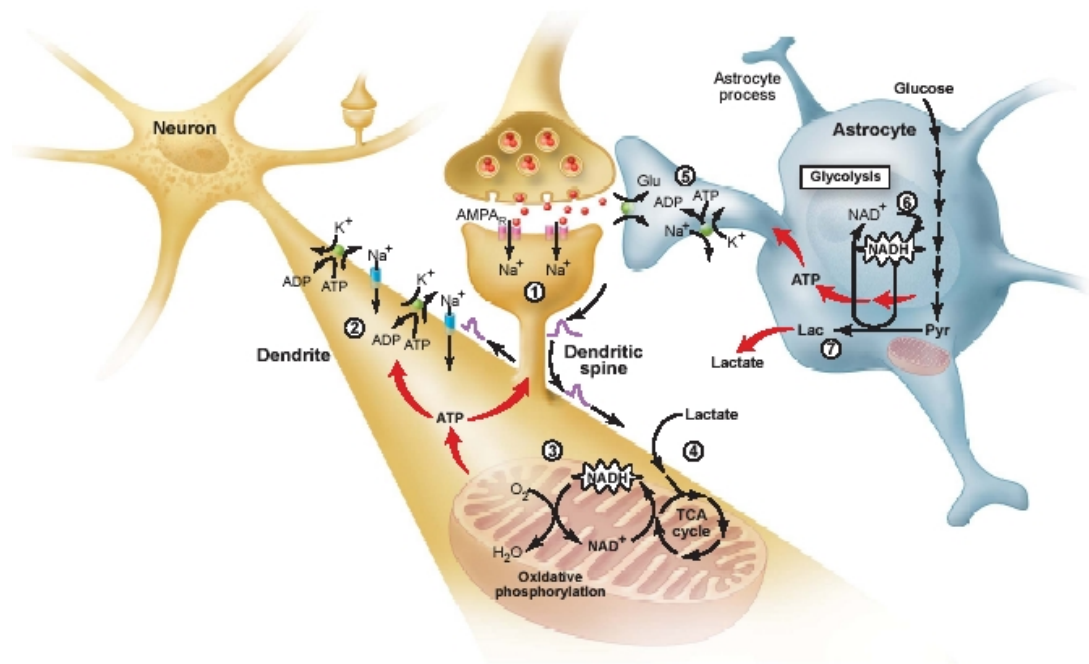
Figure 2.3: Metabolic compartment in brain cells. Separate activation of oxidative phosphorylation (respiration) in neurons (brown) and glycolysis in astrocytes (gray), as revealed by two-photon fluorescence imaging of NADH [22]. (1) Glutamate induces an excitatory postsynaptic potential (EPSP) in the dendritic spine of the neuron. (2) The depolarization propagates from the dendritic spine to the dendrite, where it may cause further opening of voltage-gated sodium channels and activation of the Na^+/K^+ ATPase, leading to an increased demand for energy (ATP). (3) Oxidative phosphorylation is activated. (4) stimulation of the TCA cycle (Krebs cycle) by lactate from the extracellular pool. (5) In parallel glutamate reuptake in astrocytes (gray) activates the glial Na^+/K^+ ATPase. (6) The increased energy demand leads to a strong enhancement of glycolysis in the cytoplasm of astrocytes. (7) The conversion of pyruvate to lactate through the activity of the enzyme lactate dehydrogenase. [24]

for the neurons by holding them together and supplying nutrients to them, are the so-called astrocytes [30, 31]. Neurometabolic coupling describes the interplay between neurons and astrocytes, leading to a directed flow of energy from the astrocytes to the neurons. This concept has been introduced by Pellerin and Magistretti [23, 24]. Figure 2.3 shows metabolic compartmentation between neurons and astrocytes. When the neurons communicate with each other, neurotransmitters, for example glutamate, will be released from one neuron at the presynaptic nerve terminal, then bind to its receptor at the postsynaptic on the next neuron. This process will generate an action potential and the pulse will propagate along

the dendrite (see label 1 in Figure 2.3). The signal may cause further opening of Na^+ channels and activation of Na^+-K^+ ATPase, leading to an increased energy demand (ATP) (see label 2 in Figure 2.3). In parallel but delayed in time, glutamate reuptake in astrocytes activates Na^+-K^+ ATPase (see label 5 in Figure 2.3). This process also needs energy (ATP) leading to a strong enhancement of glycolysis in astrocytes (see label 5 in Figure 2.3). Lactate, a glycolysis product, is released from astrocytes, and then enters neurons (see label 7 in Figure 2.3) as a substrate for the Krebs cycle (see label 4 in Figure 2.3) for compleate oxidation to CO_2 and H_2O (see label 3 in Figure 2.3) to produce a large amount of ATP. This denotes that most of the glycolytic activity occurs in astrocytes, whereas the neurons are more active in respiration. The flow of energy between the two cell types is mediated by lactate. Activation of neurons stimulates glycolysis in the astrocytes with concomitant increased extrusion of lactate.

2.3   Hippocampus

One brain structure known to be involved in the complex processes of forming, sorting, and storing memories is the hippocampus. Moreover, it is responsible for emotion and spatial navigation. The hippocampus is a part of the forebrain, located in the medial temporal lobe (Fig. 2.4). Humans and other mammals have two hippocampi, one in each side of the brain. In rat, where it has been studied most extensively, the hippocampus is shaped something like a banana. In humans, it has a curved and convoluted shape that reminded early anatomists of a seahorse. The name, in fact, derives from the Greek word for seahorse (Greek: hippos = horse, kampos = sea monster).

2.3.1   Metabolism in Hippocampus

In this section, we review former investigations of the metabolism in the hippocampus. The experiments have been performed by observations of NAD(P)H fluorescence from rat hippocampal slices. Thereby, the hippocampus was sepa-
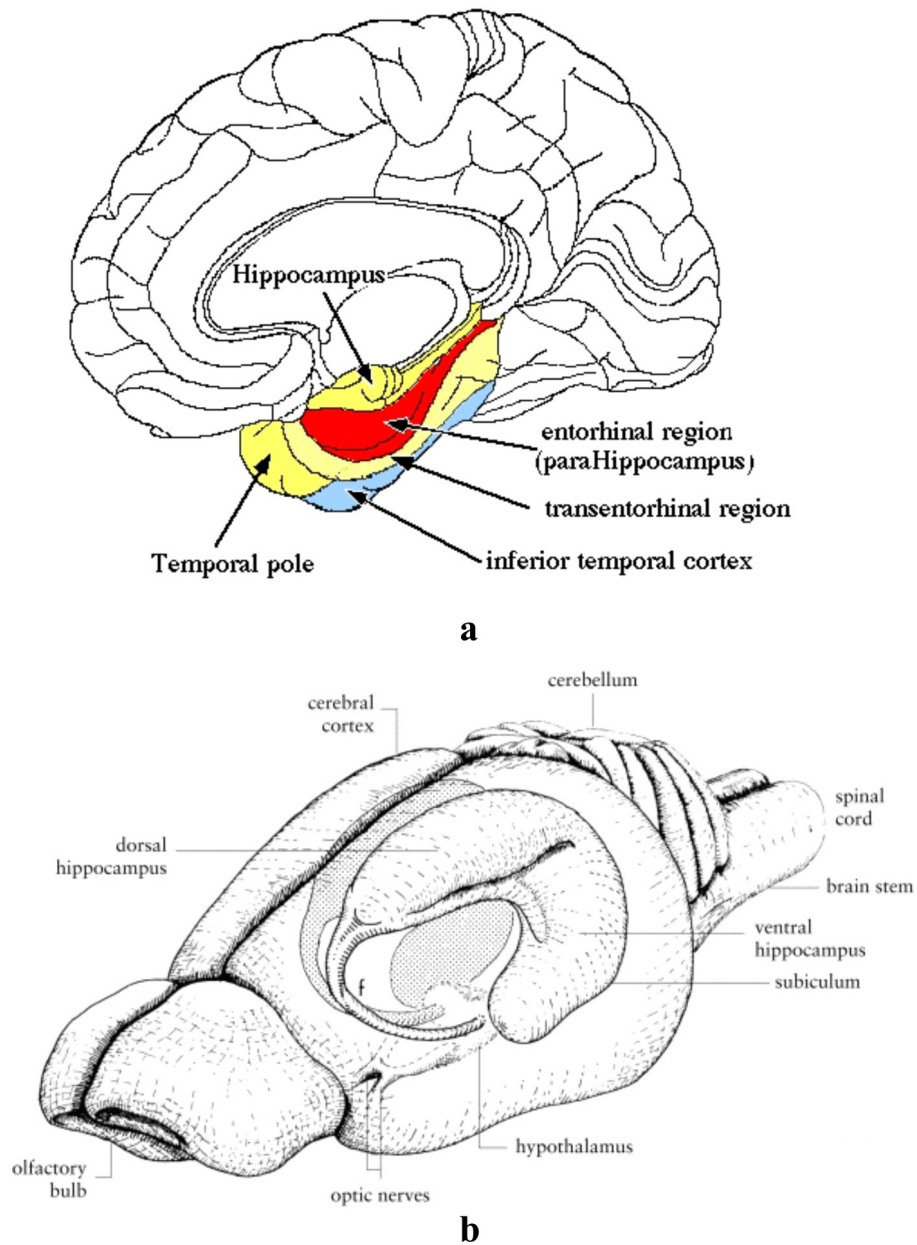
Figure 2.4: Schematic representation of hippocampus of a) human and b) rat brains. Note that the front of the head is on the left side of the picture, the back is on the right side [32, 33].
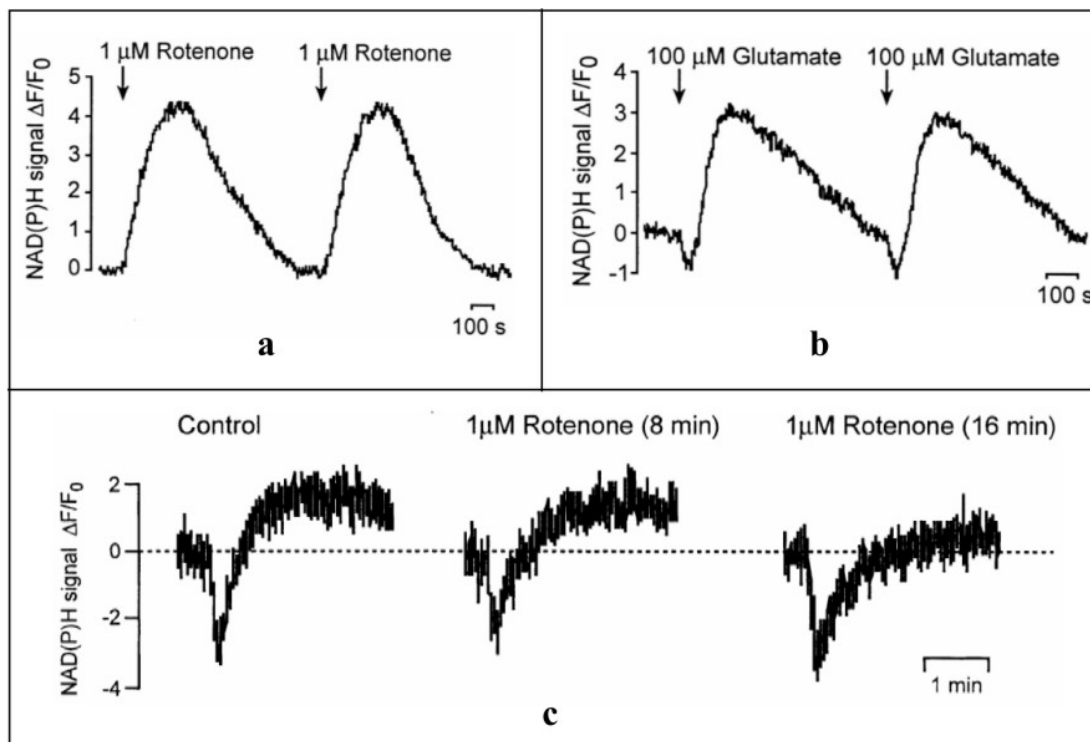
Figure 2.5: Investigations of metabolism in hippocampus by Schuchmann *et al* [20]. a) Application of 1 μM rotenone for 2–3 s resulted in an increased NAD(P)H fluorescence. b) 100 μM glutamate application led to an initial decrease followed by an increase in the fluorescence. c) An electrical stimulation also evoked an initial decrease followed by an increase in the fluorescence (see control). However, the late increase in fluorescence was reduced when the cells were incubated with rotenone for 8 min and nearly blocked after 16 min.

rated from the whole brain and was cut as thin sheets with a thickness, typically, of about 350–400 μm. The slice was placed into a recording chamber perfused with nutrition buffer.

Schuchmann *et al.* [20] showed that an application of rotenone, which is a potent inhibitor of mitochondrial respiratory chain complex I, to rat hippocampal slices led to an accumulation of NAD(P)H thus an increase in its fluorescence (Fig. 2.5 a). They also found a biphasic change of NAD(P)H fluorescence which is induced by glutamate and electrical stimuli. The biphasic response is characterized by an initial transient decrease (dip) followed by an overshoot (Fig. 2.5 b and c). However, in the presence of rotenone electrically evoked long-lasting NAD(P)H signal overshoot decreased progressively within minutes, due to a negative feedback of the accumulated NADH to the NADH-producing citrate cycle (Fig. 2.5 c).
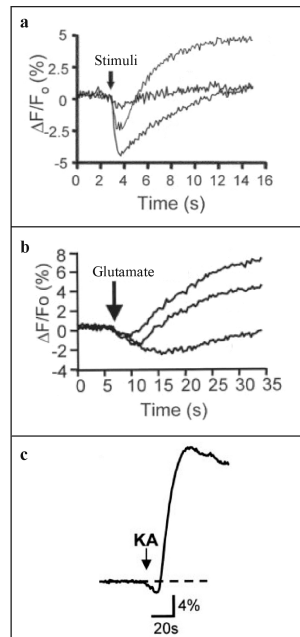
Figure 2.6: Investigations of metabolism in hippocampus by Shuttleworth *et al* [21]. a) A bipolar stimulating electrode was used to deliver a single tetanus (10 pulses, 50 Hz). An electrical stimuli induced NAD(P)H changes from three different locations. b) NAD(P)H responses from three regions evoked by glutamate. c) NAD(P)H fluorescence transients evoked by kainate stimulation.

Shuttleworth *et al.* [21] reported that three types of stimuli (electrical, glutamate, and kainate) produced biphasic (first decrease, then increase) NAD(P)H fluorescence changes as shown in Figure 2.6. These responses were matched by inverted biphasic FAD fluorescence transients proving that the biphasic NADPH responses were not an optical artifact.

Kassischke *et al.* [22] have shown that blocking mitochondrial respiration with cyanide induced an increase in NADH fluorescence and the peak of fluorescence increased with the concentration of cyanide as shown in Figure 2.7 a. However, it saturated at high concentrations. They have also discovered that the biphasic (an initial dip followed by an overshoot) NADH changes which an induced by electrical stimuli are a superposition of two distinct monophasic metabolic responses of neuronal dendrites and astrocytes (Fig. 2.7 b and d). By using glutamate receptor antagonist CNQX (6-cyano-7-nitroquinoxaline-2,3-dione), to block postsynaptic AMPA receptors, the dip of NADH signal induced by electrical stimuli is almost completely eliminated (Fig.2.7 c). Furthermore, the dip and overshoot occurred in
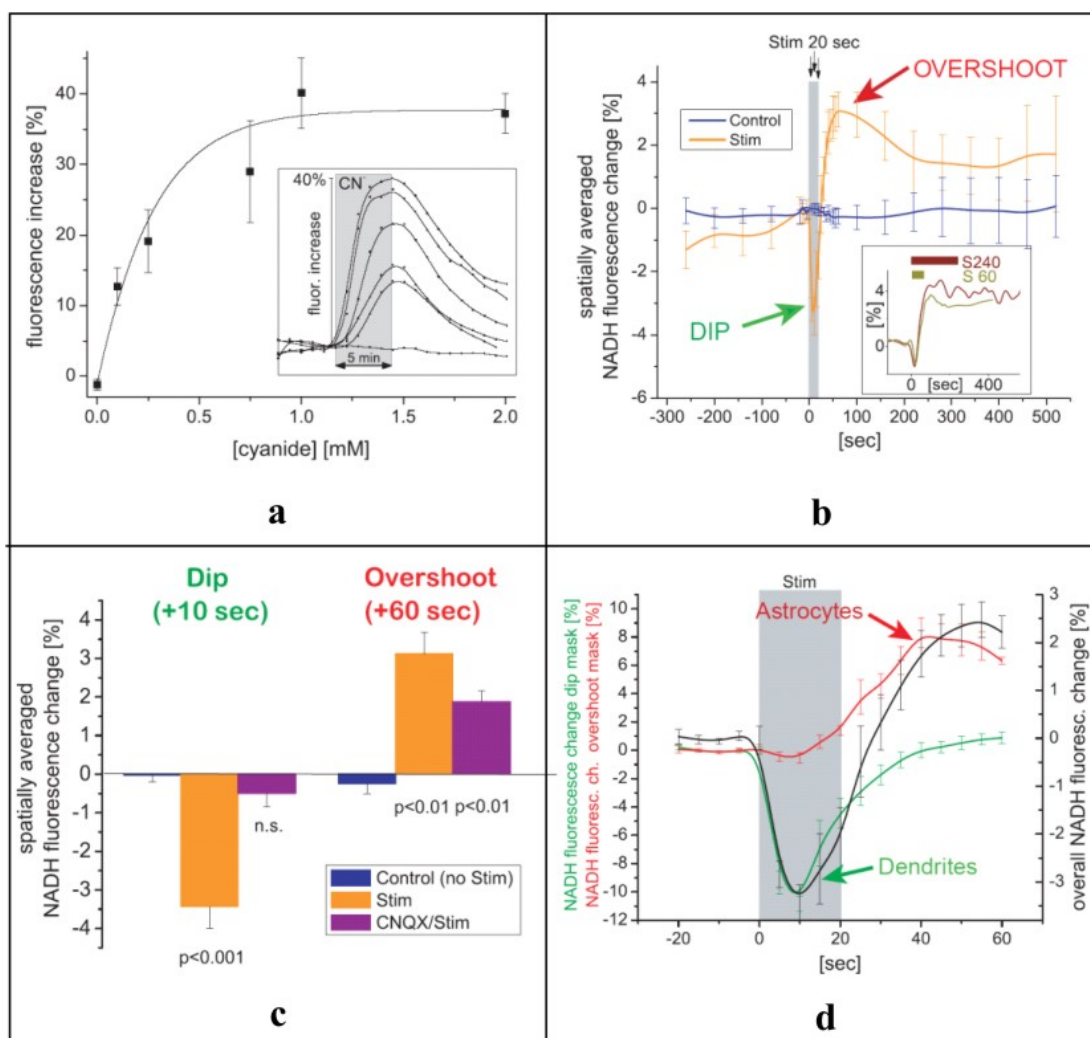
Figure 2.7: Investigations of metabolism in hippocampus by Kasischke *et al* [22]. NAD(P)H fluorescence changes. a) cyanide was applied to slices in concentrations of 0, 0.1, 0.25, 0.75, 1.0 and 2.0 mM. The inset shows the temporal dynamics of NADH fluorescence response under cyanide perfusion for 5 min. b) electrical stimuli induced a biphasic (an initial dip followed by an overshoot) response. The inset shows the response after stimuli were applied for longer times (60 s and 240 s). c) incubation the cells with CNQX, the dip of NADH signal was almost completely eliminated and the overshoot also reduced. d) the biphasic response is the sum of two spatially and temporally distinct monophasic metabolic responses,which indicated early oxidative recovery metabolism in dendrites followed by late activation of glycolysis in astrocytes.
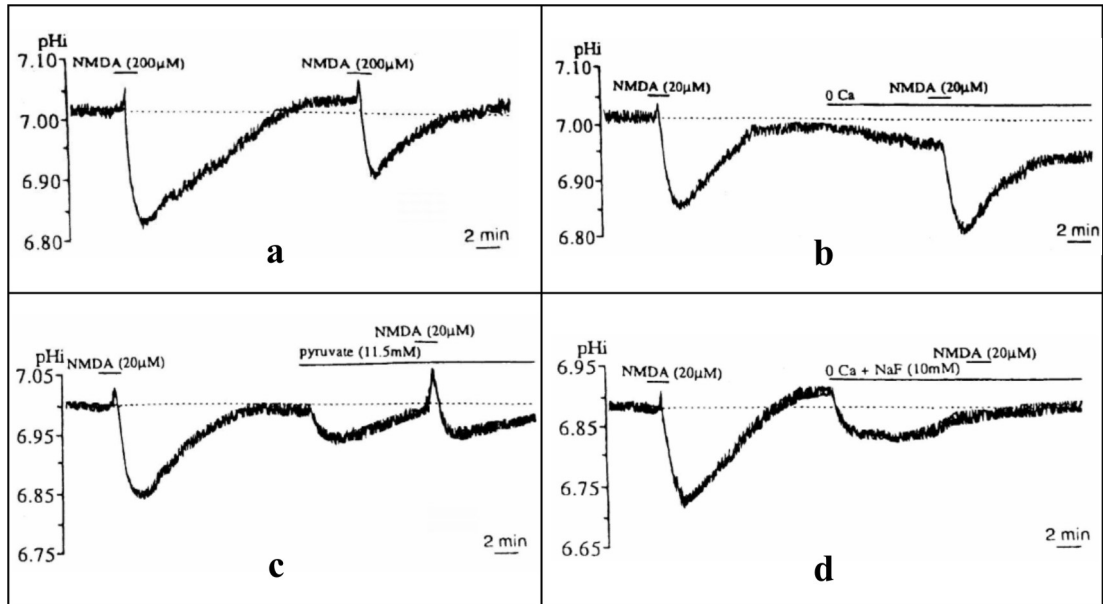
Figure 2.8: Investigations of metabolism in hippocampus by Zhan *et al* [34]. Intracellular pH changes induced by NMDA. a)200 μM NMDA application induced an initial pH_i alkaline shift followed an acid shift. b) in 0 Ca^{2+} medium, an alkaline shift was almost abolished. c) pH_i acid shift decreased when the cells were incubated in the medium with pyruvate instead of glucose. d) pH_i alkaline and acid shifts were eliminated after adding 10 mM fluoride in the medium.

different locations in the fluorescence images. These impies that the responses of the neuronal dendrites represented firstly an increase in oxidative phosphorylation (respiration) in which NADH is consumed, followed by activation of the Krebs cycle to replenish NADH. In contrast, the late overshoot was located in the cytoplasm of the processes of astrocytes. This signal corresponded to a strong activation of glycolysis in which large amount of cytoplasmic NADH are generated before being converted to NAD^+ as lactate is produced.

Zhan *et al.* [34] have found that NMDA induced a biphasic change in intracellular pH (pH_i): an initial alkaline shift followed by a long-lasting acid shift in rat hippocampal slices (Fig. 2.8 a). In the absence of Calcium, NMDA-evoked alkaline shift disappeared completely (Fig. 2.8 b). Replacement of glucose with pyruvate reduced the NMDA-induced pH_i acid shift (Fig. 2.8 c). Fluoride, a glycolytic inhibitor, completely suppressed NMDA-induced pHi acid shift (Fig. 2.8 d). Furthermore, the lactate content of hippocampal slices was markedly increased after the slices were exposed to NMDA. This implies that the initial response is
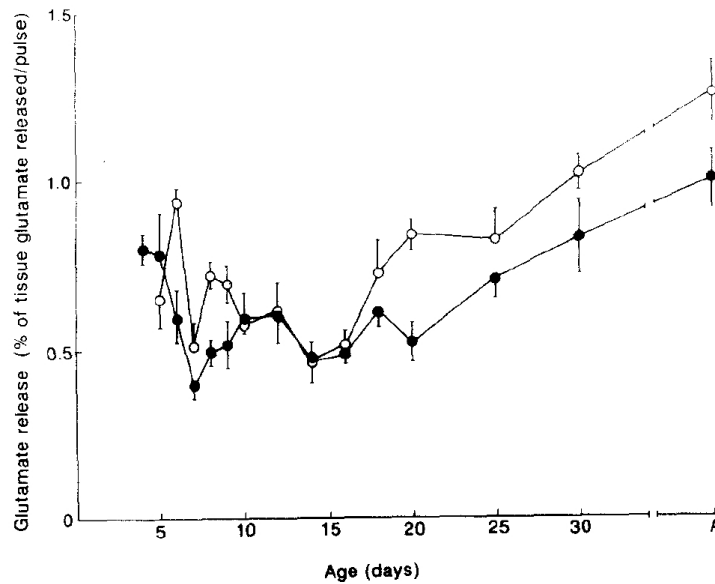
Figure 2.9: Investigations of network development in hippocampus by Collard *et al.* [35]. The release of glutamate from hippocampal (○) and cortical (●) synaptosomes in response to depolarisation with a 30 sec pulse of 20 mM K^+ changed with age. Release is expressed as the percentage of tissue glutamate released per pulse.

associated with a calcium influx and the following acid shift may be caused by an increase in lactate production through the acceleration of glycolysis.

2.3.2   Network development of hippocampus

We now consider experiments on network development in brain, especially the hippocampal part. Collard *et al.* [35] have studied the release of synaptosomal glutamate induced by K^+ depolarization during postnatal development in the rat hippocampus and cortex. In case of the hippocampus, the release increased from day 5 to day 6 and fell to near minimum level at day 7 before rising to a second peak between day 8 and day 9. Then it dropped to a minimum level at day 14 before increasing rapidly to day 20 and then more gradually to adult values (Fig. 2.9). The pattern of change was slightly different in cortical synaptosome (an isolated synapse of a neuron). The sensitivity of glutamate release mechanism to K^+ depolarization varies considerably with postnatal age. These variations may be related to plastic changes which are occurring during this critical period of brain development.

Kudryashov *et al.* [36, 37] have investigated age dependence of population spike (PS) amplitude after electrical stimuli in hippocampal slices from rats with an age from postnatal day 14 to 27. Note that a population spike is a shift in electrical potential as a consequence of the movement of ions involved in the generation and propagation of action potentials. Amplitudes of the first (PS1) and the second (PS2) were measured while paired-pulse stimuli (two electrical pulses given subsequently in a short time) were applied. Both PS1 and PS2 amplitudes increased with the age, except for on day 20 and day 21, they declined as shown in Figure 2.10. For further analysis indicated that the decreases in PS1 and PS2 on day 20 and day 21 were caused by a decrease in the number of connected neurons during synaptic plasticity (the ability of the connection between two neurons to change in strength).
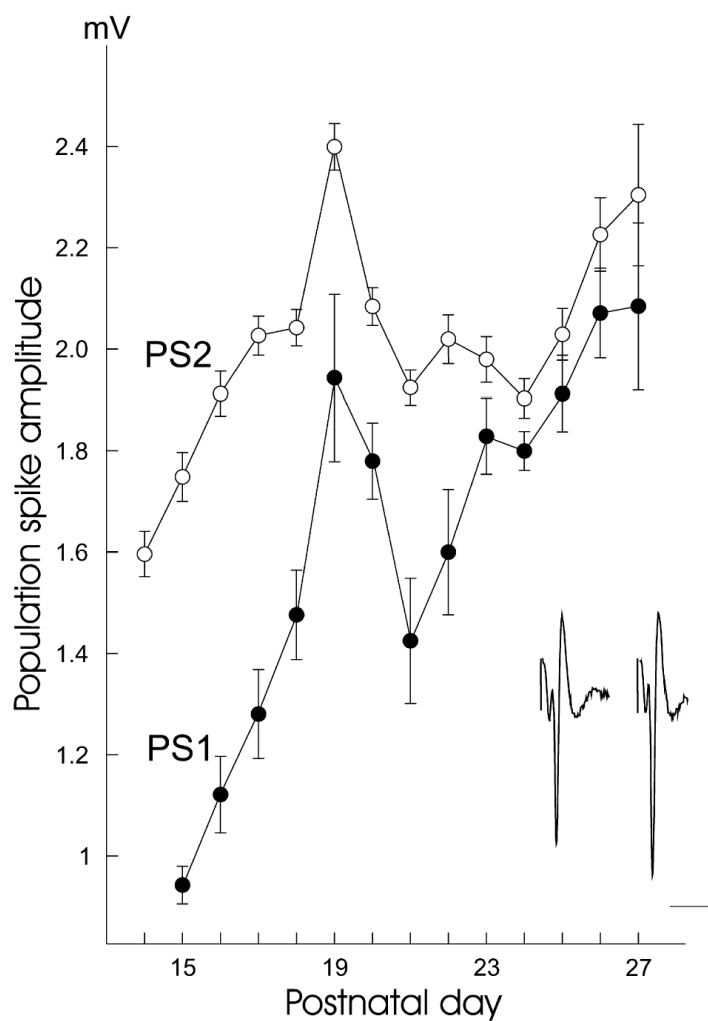
Figure 2.10: Investigations of network development in hippocampus by Kudryashov *et al* [36]. The development of population spike (PS) amplitude evoked by the first and the second stimulus in a paired-pulse paradigm. Note that a population spike is a shift in electrical potential. PS1 and PS2 amplitudes elicited using a 55-ms interpulse interval are plotted against age. The bottom right inset shows examples of population spike with horizontal and vertical scale bars of 4 ms and 1 mV, respectively.

Chapter 3

Spatiotemporal dynamics in excitable media

3.1 Reaction-diffusion mechanism

Unlike passive media in which the wave propagation gradually damps, e.g., sound waves passing through the air, active media exhibit excitation waves which propagate without attenuation of the amplitude. Active media are often described using a system of two-variable differential equations:

$$
\begin{aligned}
\frac{\partial u}{\partial t} &= \frac{f(u,v)}{\epsilon} + D_u \nabla^2 u, \\
\frac{\partial v}{\partial t} &= g(u,v) + D_v \nabla^2 v,
\end{aligned}
\tag{3.1}
$$

where u and v are called "activator" and "inhibitor" variables, respectively. $f(u,v)$ and $g(u,v)$ describe the kinetics of the reaction system. The parameter $\epsilon << 1$ accounts for the markedly different characteristic timescales of the two variables u and v. ∇^2 is the Laplacian operator, D_u and D_v are diffusion coefficients of u and v, respectively.

Active media can be classified as excitable, oscillating, and multi-stable. Figure 3.1 illustrates the local dynamics of the two variables when the reaction terms $f(u,v)$ and $g(u,v)$ are cubic and linear functions, respectively.
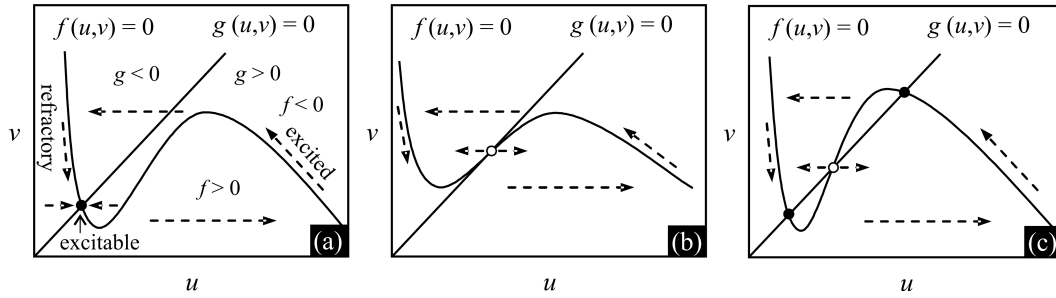
Figure 3.1: Phase diagram of local dynamics in active media. Curves and straight lines represent the u-nullcline ($f(u,v) = 0$) and the v-nullcline ($g(u,v) = 0$), respectively. Arrows indicate the direction of the dynamics. (a) Excitable media have a steady state (filled circle) which is located alone to the unstable manifold. The steady state is stable to any perturbation smaller that a threshold. A sufficiently large perturbation leads to an overshoot of u and the system is in an excited state. Before the system recovers to the excitable state, it stays in a refractory state where the system is unexcitable. (b) For oscillating media, the only one stationary state of the dynamics is unstable (open circle) so, except for this state, u and v always oscillate. (c) For bistable media, there are three fixed states, one unstable in between two others stable. The system switches from one stable state to another when a perturbation is applied.

The fast variable, the activator u, has a u-nullcline ($f(u,v) = 0$, i.e., $du/dt = 0$) consisting of three branches with a maximum and a minimum while the slow inhibitor v has a linear v-nullcline ($g(u,v) = 0$, so $dv/dt = 0$). The intersections between the two nullclines are the stationary solutions (both u and v do remain unchanged). Now we consider the dynamics of the variables in the phase diagram as indicated by the arrows (Fig. 3.1). In the domain under the u-nullcline, $f > 0$ so u always increases. By contrast, when the state of the system is located above the u-nullcline, $f < 0$ and u always decreases. Similarly, in the domain at the right of the v-nullcline, $g > 0$ and v increses but the left of the v-nullcline, $g < 0$ and v decreases. The changes of u and v in different domains specify the trajectory in the system state (u, v) as shown by the arrows.

For excitable media (Fig. 3.1a), the stationary state is stable. It is called *excitable state* since a small perturbation of u from this point would decay, however, a perturbation larger than a theshold results in an overshoot of u and the system is in an *excited state*. This occurs via an autocatalytic process. The system makes a great excursion through the phase space. Before recovering to the excitable state,
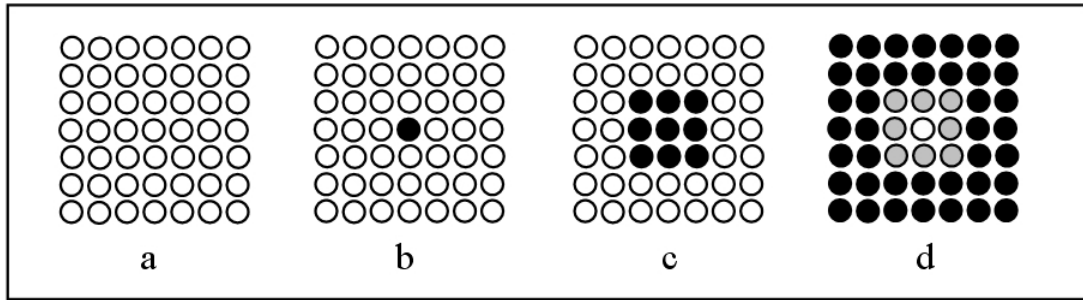
Figure 3.2: Schematic representation of excitation waves. An excitable medium can be represented as a group of elements (circles). a) the whole medium is in the excitable state (open circles). b) A sufficient perturbation at the middle causes the concentration of the activator to rise higher than a threshold so the autocatalytic process begins. Consequently, the activator concentration overshoots and the perturbed point is in the excited state (black circle). c) Due to diffusion, the high concentration of the activator spreads to the neighborhood and triggers the autocatalytic process at those points. This reaction-diffusion coupling leads to a propagation of excitation wave (spreading of the black circles). d) After the wave passes, the elements are in the refactory state (gray circles) and the concentration gradually decays and finally, they returned to the excitable state [15].

the system is in an unexcitable *refractory* state in which no further excitation can occur. In the oscillating case (Fig. 3.1b), an intersection of the nullclines occurs on the middle branch of u-nullcline and the fixed point is unstable. Except for this single point, both u and v oscillate all time. In contrast, there are three fixed states for bistable media (Fig. 3.1c). Again, the stationary point on the middle branch is unstable. The two others are stable. A sufficient perturbation will cause u and v to change and the system switches from one stationary state to the other.

Excitation waves which are propagations of concentration changes result from the coupling of local excitable dynamics (described above) with diffusion. Figure 3.2 shows a schematic representation of a reaction-diffusion wave. In the excitable state, the concentration of the activator is below a threshold value and the system remains homogeneous (open circles in Figure 3.2a). Patterns can arise in this homogeneous medium, when a local perturbation causes the concentration of the activator to rise slightly above the threshold which, in turn, starts the autocatalytic reaction (black circles in Figure 3.2b). The activator at the location with a high concentration, then, diffuses to the neighboring elements and triggers the

autocatalytic reaction of the neighbors (Fig. 3.2c). Hence, the excitation wave (the black circles in the figure) spreads, starting from the perturbed location. The front of the propagation is in the excited state. However, after passage of the wave, the medium is in the refractory state (grey circles in Figure 3.2d) and gradually returns to the excitable state.

3.2   Properties of excitation waves

Excitation waves can be generated at multiple sites within a medium and hence the waves can propagate towards each other. When colliding, excitation waves show mutual annihilation, i.e., interference of waves does not occur. The wave velocity increases with the period – the longer period allows the system to recover and get back closer to the excitable state – yielding a *dispersion relation* [38, 39]:

$$c(T) = c_0 \tanh\left(T/T^*\right), \tag{3.2}$$

where $c(T)$ is the wave velocity at period T while c_0 is the velocity of a single pulse $(T \rightarrow \infty)$ traveling in an absolute by excitable media. T^* is the possible shortest period at which waves can propagate in the excitable media.

Moreover, it is found theoretically [40, 41] and experimentally [42] that the wave velocity $c(\kappa)$ depends on the curvature. An increase of the curvature leads to a decrease of the velocity. This velocity-curvature relationship can be described by the *eikonal equation*:

$$c(\kappa) = c_0 - D_u \kappa, \tag{3.3}$$

where $c(\kappa)$ is the velocity of the curved wave front with a curvature κ while and c_0 is the velocity of a planar wave front. D_u is the diffusion coefficient of the activator u. From this equation a critical radius for propagation of the waves can be obtained. We set $c(\kappa) = 0$ and $\kappa = \frac{1}{R}$ and obtain:

$$R = \frac{D}{c_0} \tag{3.4}$$
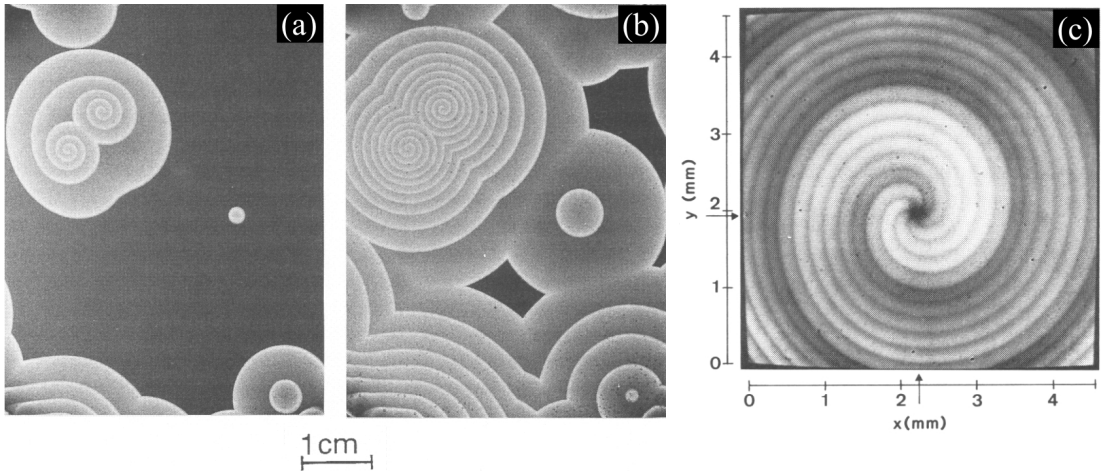
Figure 3.3: Target pattern and spiral waves in a thin layer of the BZ reaction at (a) early and (b) later stages [43]. Top left: a pair of counter-rotating spirals, bottom right: a target pattern. (c) a superposition of six subsequent images of a spiral wave [44]. The spiral core appears as a small circular dark region (at $x = 2.25$ mm, $y = 1.95$ mm) in the image.

This means that there is a critical radius R at and below which an outward propagation of waves can not take place ($c(\kappa) = 0$).

3.3 Circular and spiral waves

Systematic experimental studies of the wave dynamics have been done most often using the Belousov-Zhabotinsky (BZ) reaction [44–49] due to convenience of the experiment including the preparation of the medium and the observation of the waves. Circular waves triggered by a pacemaker (e.g., an impurity such as dust) are often observed in experiments using the BZ reaction. At each pacemaker, the circular waves are produced periodically yielding a target pattern (as at bottom right in Figure 3.3a and b). When a circular wave front is broken, e.g., by pushing an air blast from a pipette to the front, the two open ends of the front. Due to the fact that the velocity of a wave front depends on the local curvature [according to the eikonal relation Eq. (3.3), the open ends of the front, thus, curl in and form a pair of counter-rotating spiral waves (at the top left in Figure 3.3a and b). The position of the spiral tip is corresponds to the point of highest curvature along an isoconcentration line of the spiral wave [50, 51] and the tip rotates around the spiral
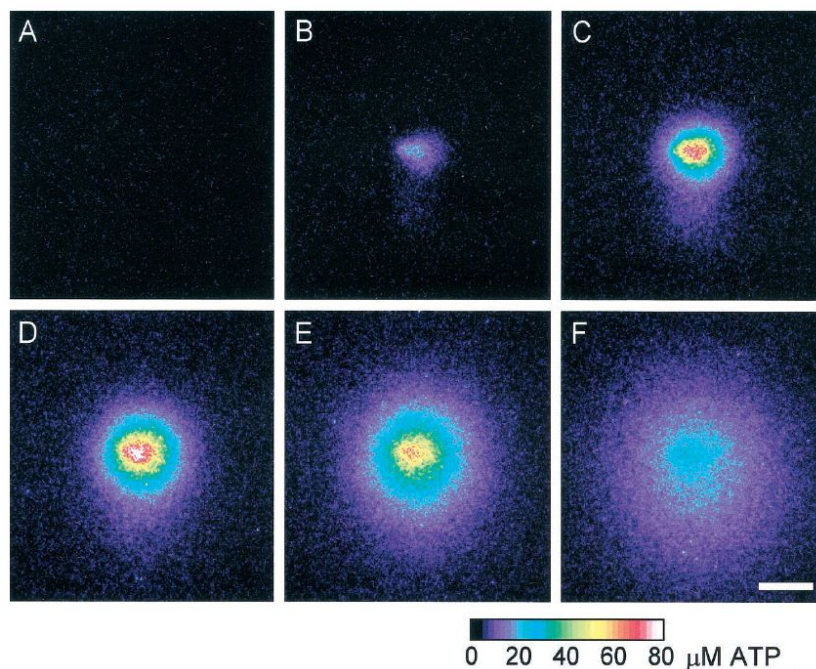
Figure 3.4: Expanding circular ATP wave in rat retina evoked by a mechanical stimulation. ATP concentration is indicated by the pseudocolor scale at the bottom and the scale bar is 100 μm. Elapsed time after the stimulation in A-F: 0, 0.7, 2.0, 4.0, 7.9, and 16.5 s [52].

core which is a small quiescent area appearing as a dark region in a superposition of spiral wave images (Fig. 3.3c). When wave fronts collide with other or reach the walls of the container, they annihilate without interference or reflection.

In biological systems, circular waves have been reported to occur spontaneously in yeast extracts [11]. The circular waves can also be initiated in a controllable fashion using external stimulations [8, 52]. Figure 3.4 presents an example of expanding circular ATP waves in a retinal slice of rat [52] after a mechanical stimulation. Spiral waves are known as extremely robust spatiotemporal patterns. They have been observed in different biological excitable media as shown in Figure 3.5(a)–(e): (a) *Xenopus laevis* oocytes, (b) the cell aggregation of the slime mould *Dictyostelium discoideum*, (c) chicken retina, (d) yeast extract, (e) hippocampal slice cultures, and (f) cardiac tissue.
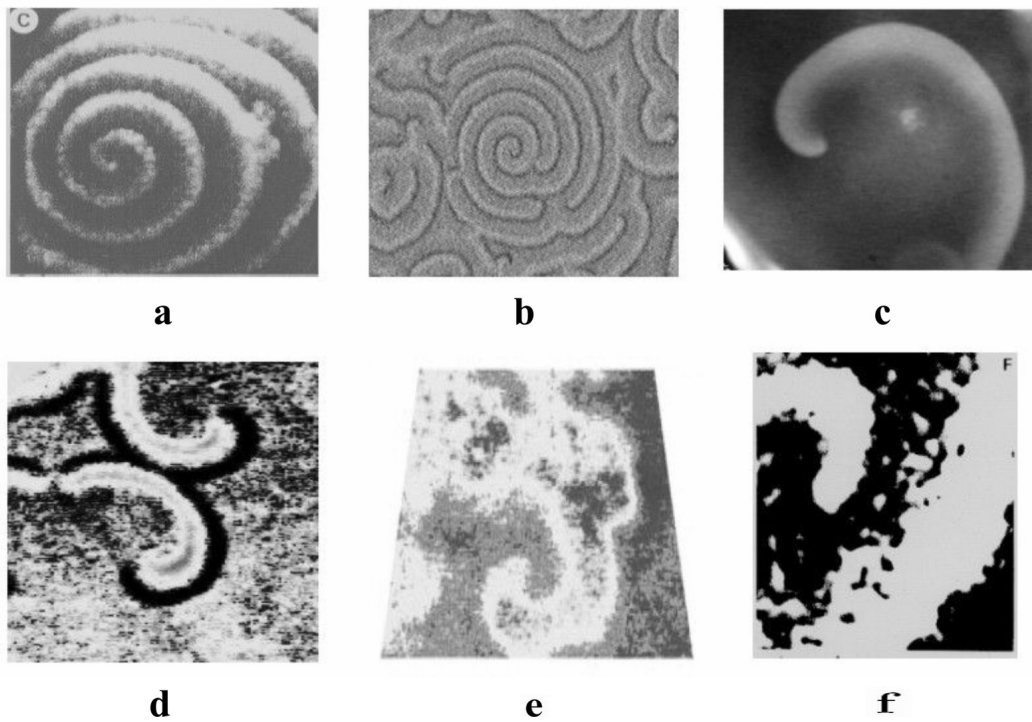
Figure 3.5: Rotating spiral waves in various biological excitable media: (a) Ca^{2+} waves in *Xenopus laevis* oocyte [6], (b) aggreation patterns of the slime mould *Dictyostelium discoideum* [53], (c) spreading depression waves on chicken retina [54], (d) spiral waves propagating during glycolysis in yeast extract [55], (e) intercellular Ca^{2+} waves in hippocampal slice cultures [5], (f) Electrical waves in the ventricle of the heart during ventricle tachycardia [56].
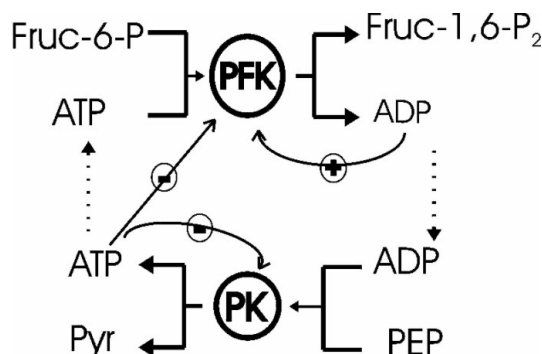
Figure 3.6: Reaction catalyzed by the enzyme PFK. The figure illustrates the allosteric regulation of PFK by positive and negative effectors.

3.4   Glycolytic oscillations and waves

In the this section, excitation patterns concerning glycolysis process are reviewed in detail since we investigated this process in hippocampal cell cultures.

In glycolysis, the enzyme phosphofructokinase (PFK), which is an allosteric enzyme, catalyzes the autocatalytic process in glycolysis (Fig. 2.1). For an autocatalytic process, at least, one of the products also acts as an activator of the reaction. The activity of the enzyme can be affected by its effectors. In the case of PFK, adenosine diphosphate (ADP) and adenosine mophosphate (AMP) act as the positive effectors and adenosine triphosphate (ATP) is the negative effector, as shown in Figure 3.6 [57]. There is a coulping between the first phase (C6-carbons) and the second phase (C3-carbons) of glycolysis via ATP consuming (hexokinase, phosphofruc-tokinase) and ATP producing enzymes (phosphoglyc-ertkinase, pyruvatkinase). Moreover, the glycolytic flux is directly coupled to an oxidation/reduction cycle of NADH. Allosteric regulation and the cooperativity of the PFK are the kinetic bases that drive the system into the oscillatory state [58]. Glycolytic oscillations have been observed in many types of cells and cell extracts, e.g., in yeast cells and yeast extract [59–62], smooth muscle cell extract [63], skeletal muscle cell extract [64], heart cells [65], tumor cells [66], and pancreatic β-cells [67, 68].

The autocatalytic process of PFK coupling with the diffusion of ADP can lead to spatio-temporal waves of NADH and proton. A model which takes into account
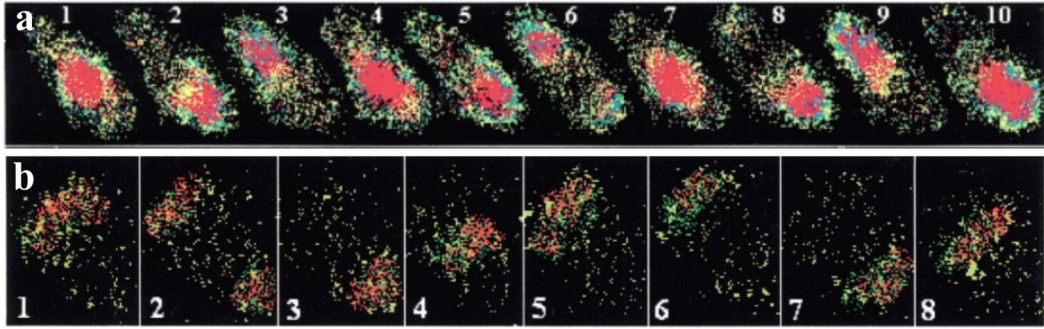
Figure 3.7: NAD(P)H and proton waves in a neutrophil cell. Images were collected for 10 ms at a 90 ms intervals. a) time sequence of NAD(P)H autofluorsecence. b) a time sequence of eight images of a SNARF-1-labeled cell (pH indicator). Cell is elliptical from top left to bottom right [10].

this view was proposed by Goldbeter [58]. The Goldbeter model considers the PFK reaction and its regulation via the product ADP as the key step of oscillatory glycolysis. Mair and Müller [9] have demonstrated that traveling NADH and proton concentration waves in yeast extract exhibited properties of reaction-diffusion patterns, i.e., mutual annihilations and formation of spiral waves. NADH waves traveled at 5 μm/s and the front width was about 0.7 mm which agree well with the Goldbeter model [58]. In addition, controlled initiations of NADH waves with a strong activator of PFK confirmed the theoretical assumption about the important impact of PFK enzyme for wave generation.

Petty et al. [10] have demonstrated sustained traveling waves of NAD(P)H and proton in living cells as shown in Figure 3.7. They have measured the spontaneous formation of these waves in polarized neutophils. The wave velocity amounted to about 5 μm/s which is in good agreement with the results from yeast extract, whereas the wave width was about 3-4 μm, i.e., about 100 times smaller. Yeast extract does not contain organelles. Therefore, the different shape of the waves maybe a consequence of metabolic interactions between the glycolytic pathway and morphological substructures. The wave movement in neutrophils is unidirectional and always along the elongated cell axis, hence coinciding with the direction of cell motility.

Chapter 4

Fluorescence spectroscopy

Fluorescence spectroscopy is one of the most widely used spectroscopic techniques in the fields of biochemistry and molecular biophysics today, due to its extremely high sensitivity and selectivity.

4.1 Basic fluorescence theory

Fluorescence is a luminescence, in which the molecular absorption of a photon triggers the emission of another photon with a longer wavelength. Processes which occur between the absorption and emission of light are usually illustrated by a Jablonski diagram as shown in Figure 4.1.

A molecule has absorbed energy in the form of electromagnetic radiation. If the photon emission (shown in as a short wavelength, that is downward pointing, "long" green line in the diagram) occurs between states of the same spin state (e.g. $S_1 \rightarrow S_0$) this is termed fluorescence. If the spin state of the initial and final energy levels are different (e.g. $T_1 \rightarrow S_0$), the emission (loss of energy) is called phosphorescence. In the diagram this is depicted by a longer wavelength (lower energy) and therefore shorter length red line. Since fluorescence is statistically much more likely than phosphorescence, the lifetimes of fluorescent states are very short (1 x 10^{-5} to 10^{-8} seconds) and phosphorescence somewhat longer (1 x 10^{-4} seconds to minutes or even hours; think about glow-in-the-dark flying disks).

Three nonradiative deactivation processes are also significant here: internal
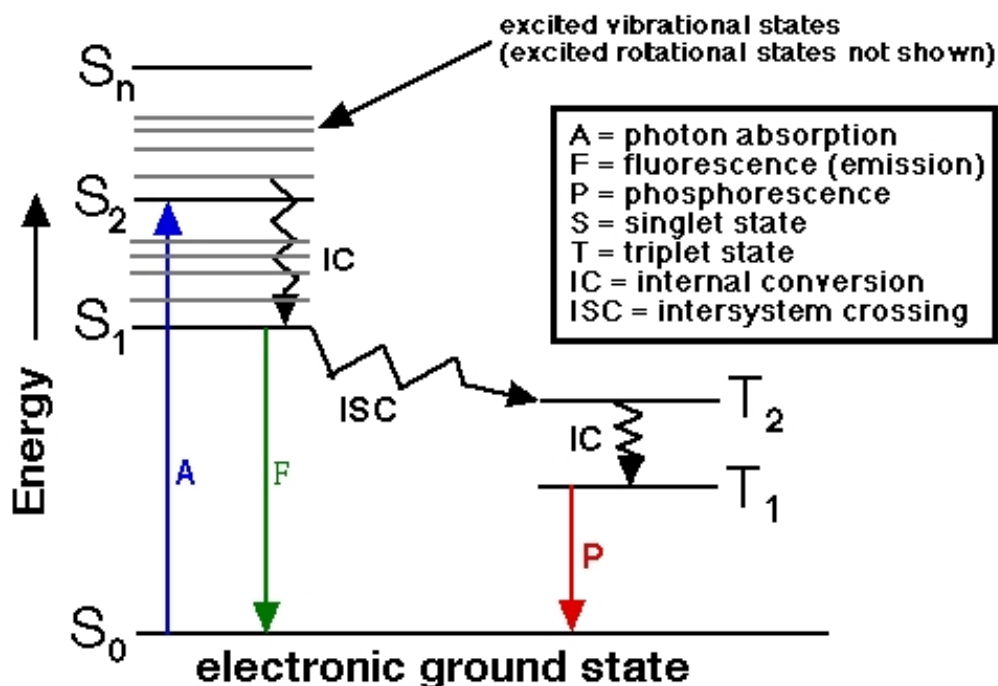
Figure 4.1: Jablonski diagram [69]. For the explanation see text.

conversion (IC), intersystem crossing (ISC) and vibrational relaxation. Examples of the first two can be seen in the diagram. Internal conversion is the radiationless transition between energy states of the same spin state (in contrast to fluorescence-that is a radiative process). Intersystem crossing is a radiationless transition between different spin states. Vibrational relaxation, the most common of the three, occurs very quickly for most molecules ($<1 \times 10^{-12}$ seconds) and is enhanced by physical contact of an excited molecule with other particles with which energy, in the form of vibrations and rotations, can be transferred through collisions. This means that most excited state molecules never emit any energy because in liquid samples the solvent or, in gas phase samples, other gas phase molecules that are present "steal" the energy before other deactivation processes can occur.

4.2 NAD(P)H fluorescence

Nicotinamide adenine dinucleotide (NADH) is the predominant component of tissue autofluorescence under UV excitation, but after donation of electrons to the
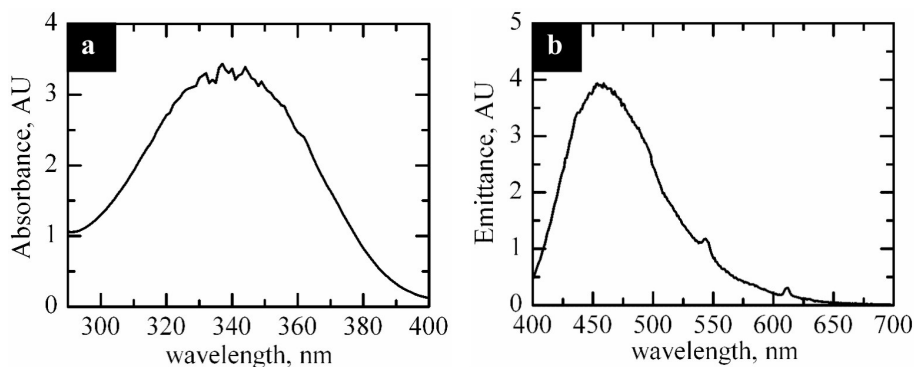
Figure 4.2: Absorption and emission spectra of 1 mM NADH.

electron transport chain, the oxidized molecule (NAD^+) is non-fluorescent. The NADH is excited at wavelength about 340-360 nm and its fluorescence is at about 460 nm. Figure 4.2 shows absorption and emission spectra of NADH.

4.3   pH indicators

Seminaphthorhodafluor (SNARF) acetoxymethyl (AM) ester is one of fluorescence indicators which enable researchers to determine intracellular pH in the physiological range. The acetoxymethyl (AM) ester derivatives of fluorescent indicators make up one of the most useful groups of compounds for the study of living cells. Modification of carboxylic acids with AM ester groups results in an uncharged molecule that can permeate cell membranes. When added to cells, SNARF-AM crosses cell membranes and once inside the cell, the acetoxymethyl groups are removed by cellular esterases. Removal of the acetoxymethyl esters regenerates SNARF indicator whose fluorescence can be excited by visible light.

Carboxy SNARF-1

The carboxy SNARF-1 dye, which is easily loaded into cells in the form of its cell-permeant AM ester acetate, has a pK_a of about 7.5 at room temperature and 7.3–7.4 at 37°C. Thus, carboxy SNARF-1 is useful for measuring pH changes between pH 7 and 8. The emission spectrum of carboxy SNARF-1 undergoes a pH-dependent wavelength shift, thus allowing the ratio of the fluorescence intensities
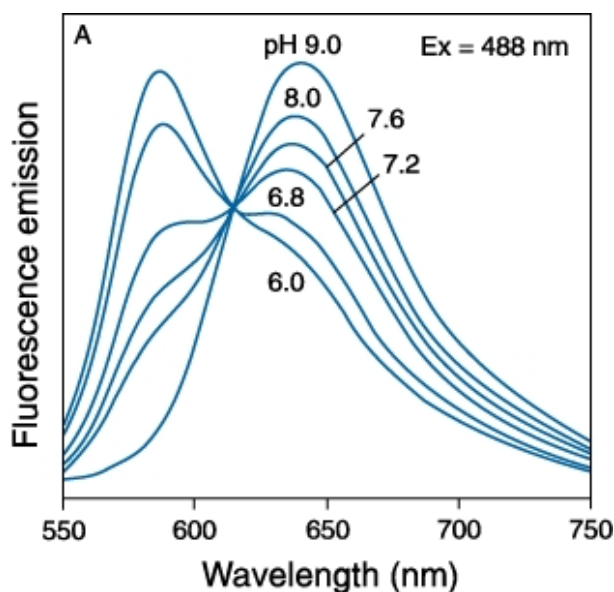
Figure 4.3: The fluorescence emission spectra of carboxy SNARF-1 [70].

from the dye at two emission wavelengths to be used for more accurate determinations of pH. Carboxy SNARF-1 is typically used by exciting the dye at one wavelength between 488 nm and 530 nm while monitoring the fluorescence emission at two wavelengths typically about 580 nm and 640 nm. Carboxy SNARF-1 is particularly well suited for instrumentation with a visible-light fixed-wavelength excitation source, including confocal laser scanning microscopes. In this study, SNARF-1 was used for 488 nm excitation. Figure (4.3) shows the fluorescence when SNARF-1 is excited with 488 nm laser for different pH values. For example, when pH increases from 6 to 9, the fluorescence at a wavelengths less than 600 nm decreases but the fluorescence with a wavelength larger than 630 nm increases. This allows ratioing of the fluorescence in order to avoid artifacts. To detect the change of fluorescence in two different ranges of the wavelengths, two optical band pass filters 535-590 nm and 633-719 nm, respectively are used.

SNARF-5F carboxylic acid

Although the carboxy SNARF-1 indicator possesses excellent spectral properties, SNARF-5F carboxylic acid is suited better for our measurements using fluorescence microscope together with an image intensified CCD-camera. Since the SNARF-5F has one emission when it is excited with light of 543 nm wavelength as shown in
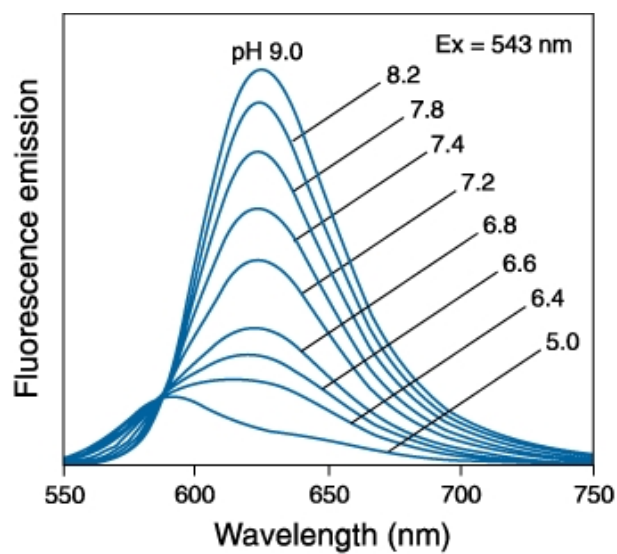
Figure 4.4: Fluorescence emission spectra of SNARF-5F 5-(and 6-) carboxylic acid as a function of pH [70].

Figure 4.4. The graph shows that when the fluorescence emission increases, the pH also increases. The SNARF-5F carboxylic acid has a pK_a of about 7.2 and this indicator has the best spectral properties for estimating cytosolic pH.

Chapter 5

Material and Methods

In this chapter, we present the methods to investigate the energy metabolism in hippocampal cell cultures using fluorescence observation. We describe the preparation of cell cultures, the chemical stimuli, the fluorescence imaging, and data analysis. At the beginning of this study, a confocal laser scanning microscope which gives high contrast images was used. Due to the low speed of image acquisition of the confocal microscope, most of the experiments were performed using a wide-field microscope with an image intensified camera instead. Both of the microscopes are briefly described.

5.1 Primary Cell cultures and nutrition buffer

Primary cultures of hippocampal cells of newborn rats (white Wistar) were prepared by Uta Kreher, Institute of Biology, Faculty of Natural Sciences, Otto-von-Guericke Universität Magdeburg., as described in Braun et al. [71]. These cultures are composed of neurons and glia cells with nearly the same fractions (50%:50%).

The cells were placed on a polylysine coated cover glass (12 mm diameter) and cultured during the first day in culture medium (M1) containing: 90% DMEM (Sigma), 0.45% glucose (Sigma), 40 mM $NaHCO_3$ (Sigma), 10% fetal bovine serum (Biochrom), 20 g/ml gentamicin (Invitrogen) and 1 mM glutamax (Invitrogen). For the subsequent days of cultivation the medium (M1) was replaced by another culture medium (M2) consisting of: 98% Neurobasal, 2% B27, 10 g/ml gentamicin,

and 1 mM glutamax (all from Invitrogen). The pH of the media was 7.35. The medium (M2) was renewed every 4 days. The cells were cultured in a tempered incubator at 37 °C under constant aeration with 95% O_2 and 5% CO_2.

We measured the response of the energy metabolism to external perturbations at different days of cultivation (3-22 days *in vitro*). At the day of the experiment, the cells were taken from the incubator and first placed into conditioning medium (CM) for 5 minutes of the following composition: 129 mM NaCl (Roth), 4 mM KCl (J.T.Baker), 1 mM $CaCl_2$ (Merck), 1M glycine (Merck), 10 mM HEPES (Serva), 4.2 mM D-Glucose (Sigma), pH 7.35. Osmolarity was adjusted to 315 mOsm with Sucrose (Roth). Thereafter, the cells were transferred into recording medium (RM) which had the same composition as CM except that glycine was replaced by 0.5 mM MgCl (Merck).

5.2   Local chemical stimulations

Locally chemical stimulations were performed using a nano-injector, as described in the next section.

To evoke energy metabolism, N-Methyl-DL-aspartic acid, NMD(L)A (Sigma) or KCN (Merck) was applied to the cell cultures. NMD(L)A and KCN were dissolved in distilled water and were prepared freshly for each set of the preparation of cell cultures, i.e., the solutions were used within one month after the preparation.

Activation of neuronal activity by NMDA

The response of the energy metabolism to chemical stimulation of neuronal activity was measured at different days of cultivation (3-22 days *in vitro*). Neuronal activation was achieved by applying NMD(L)A (Sigma), using a nano injector (Nanoject from H. Saur, Germany). The diameter of the tip was about 5-7 μm and was placed close to the cells for which fluorescence measurements were taken. In some experiments, 50 μM of the NMDA receptor antagonist D(-)-2-amino-5-phosphonopentanoic acid (D-AP5, Calbiochem) or 2 mM KCN (Merck) were added to the recording medium.
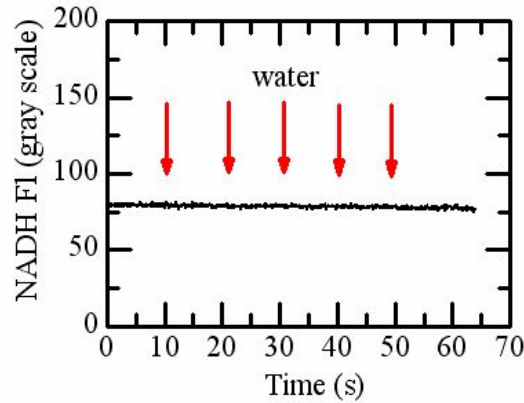
Figure 5.1: Controlling experiment with distilled water. A local of 60 nl of distilled water was added to the cell cultures.

Blockade of respiration by KCN

In order to distinguish between aerobic and anaerobic energy metabolisms, i.e., between glycolysis and mitochrondrial respiration, KCN has been applied to the cells. When testing the effect of KCN directly on the energy metabolism, 60 nl of a 0.5 M solution was injected locally into the cell culture which was incubated with 300 μl of recording medium. The final average concentration of KCN is 0.1 mM. This corresponds to a 5000 times dilution. In the experiment using bath application, this concentration (0.1 mM) is considered low in which cyanide still affects the cells [22]. For some experiments on the activation of neuronal activity by NMDA , 2 mM KCN was added to the recording medium as mentioned above before the cell cultures were placed in this buffer.

As controlled experiments, we have tested for artifacts in our experiments. The artifacts may come from, for example, mechanical perturbations which are possibly from the nano-injector. In the controlled experiments, we applied distilled water to the cells and the results (Fig. 5.1) showed that there was no response of the cells due to the injections of water using the nano-injector. This indicated that there were no (known) artifacts in our experiments.
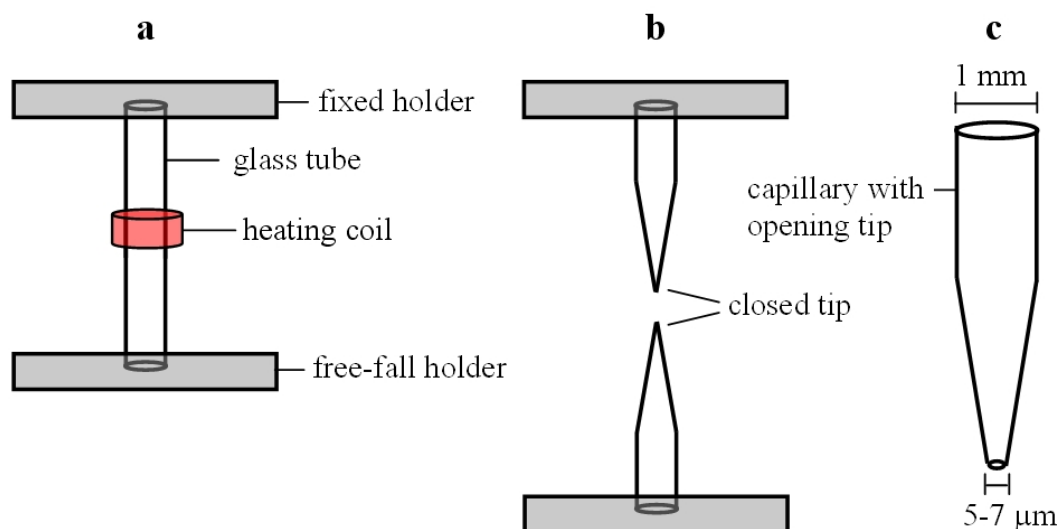
Figure 5.2: Preparation of capillary for locally chemical stimulations. a) A glass tube (diameter = 1 mm) is attached to holders and set vertically. The upper holder is fixed while the lower holder is free-fall movable. A heating coil (length = 1 cm) causes a portion at the middle of the tube to melt. b) Due to the weight of the tube and the lower holder, the melting part is lengthened until the tube splits into two parts whose smaller ends are closed. c) Each of the closed ends is carefully broken under a microscope and the capillary has a small open end with a diameter of $\sim$ 5–7 μm.

5.3   Nano-injector

The local chemical stimulations were realized by using a nano-injector (Nanoject from H. Saur, Germany). It is composed of three components: a gun, a glass capillary, and an electronic control unit. The glass capillary with a small tip of 5-7 μm in diameter was made from a glass tube.

We prepared the glass capillary as described in Figure 5.2. The glass tube (diameter = 1 mm, H. Saur, Germany) was hold vertically and a small patch on the tube was melted by a heating coil (Fig. 5.2a). Due to the weight of the lower part, the heated part was lengthened and its diameter became smaller until the tube separated into two parts (Fig. 5.2b). With this way, we got straight glass tubes of a varing diameter. In fact, one end of each tube was closed (diameter = 0 μm). Then, we broke the closed end in a controllable way under a microscope (Fig. 5.2c). The tube was attached to the stage of the microscope. By carefully adjusting the stage via a knob, the closed end collided with an obstacle fixed next
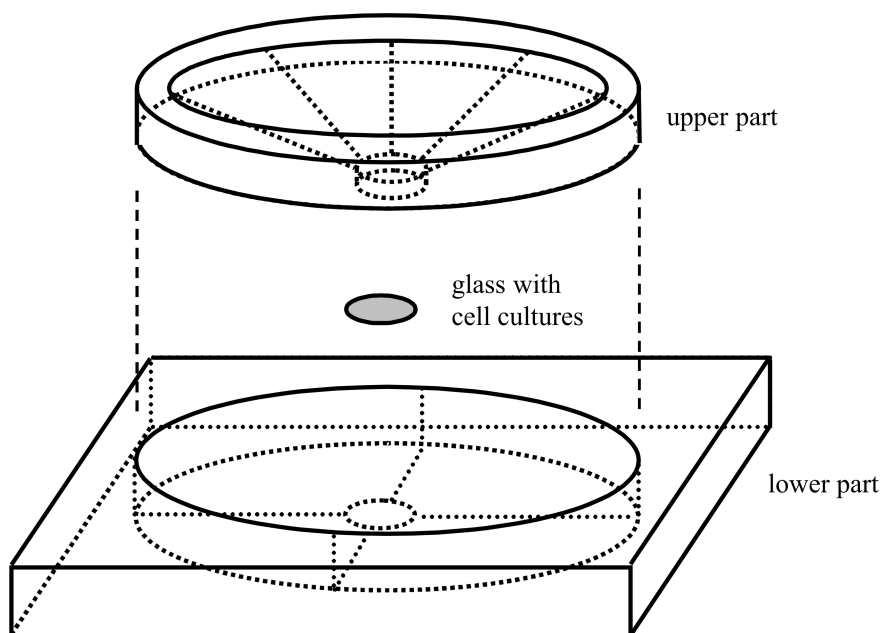
Figure 5.3: Reaction chamber. The reaction chamber is composed of two parts – upper and lower parts. A glass with cell cultures (10 mm diameter) was sandwiched between both parts. The 8 mm diameter hole in the center of the chamber allows the objective lens of the microscope to approach the glass. The upper part was manufactured as a cone shape (height = 10 mm, diameter = 100 and 8 mm at top and bottom, respectively) for convenience in a chemical stimulation using a nano injector. The dimensions of the lower part are 120×120 mm^2 fitting with the stage of the fluorescence microscope.

to the stage causing the end to break and open.

Filling and ejection of the solution was controlled by an electronic controller equipped with the injector. This allowed application of a precise volume of the solution. The ejected volume is as small as 4.6 nl. For each experiments, the injector was fixed next to the observation setup. The tip of the capillary was immersed into the buffer and was placed near one edge of the field of observation.

5.4 Reaction chamber

To investigate the response of the cell cultures to a local chemical stimulation, we designed a reaction chamber for this specific purpose. Figure 5.3 shows a sketch of this reaction chamber which is composed of two main compartments, i.e., upper and lower parts. Both parts were made from stainless steel. During the experiments, a

circular glass with cell cultures (diameter = 10 mm) was placed between the two parts. The hole (diameter = 8 mm) in the lower part allowed the objective of the microscope to reach the bottom of the culture glass for fluorescence imaging while the cone-shaped cut in the upper part gives a convenient way for the tip of the nano injector to approach the cells. A thin rubber ring was also set between the upper part and the glass for sealing.

5.5 Fluorescence imaging

In this section, we explain the fluorescence image acquisition using a wide-field microscope which we mainly used in this study. At the end of the section, the principle of confocal microscopy is mentioned as well, since we used a confocal microscope for our experiments at the beginning. Confocal microscopy offers several advantages over conventional wide-field optical microscopy, including the ability to control depth of field, elimination or reduction of background information away from the focal plane (that leads to image degradation), and the capability to collect serial optical sections from thick specimens. However, the scanning speed of the confocal microscope LSM 510, Zeiss which we used is quite low. It takes 5 frames per second for a 512×512 pixel image. We have expected to observe intracellular glycolytic wave phenomena, i.e. propagations of NAD(P)H and intracellular protons changes which maybe too fast to be detected with this low temporal resolution. Therefore, the results described in sections 6.2 and 6.3 were obtained using the inverted fluorescence microscope (Axiovert 200, Zeiss) equipped with an image intensified CCD-camera (Proxitronic) which takes the images with a rate of 12.5 frames per second.

Figure 5.4 shows a schematic presentation of the experimental setup using a wide-field microscope. The reaction chamber containing cell cultures was transfered to the stage of an inverted fluorescence microscope (Axiovert 200 Zeiss) equipped with a 40x 1.3 NA oil-immersion Plan-NEOFLUAR objective lens (Zeiss).

The cellular NAD(P)H fluorescence was excited with a mercury lamp (HBO 103 W), through 365/12 nm band pass filters (Zeiss). The fluorescence at 460
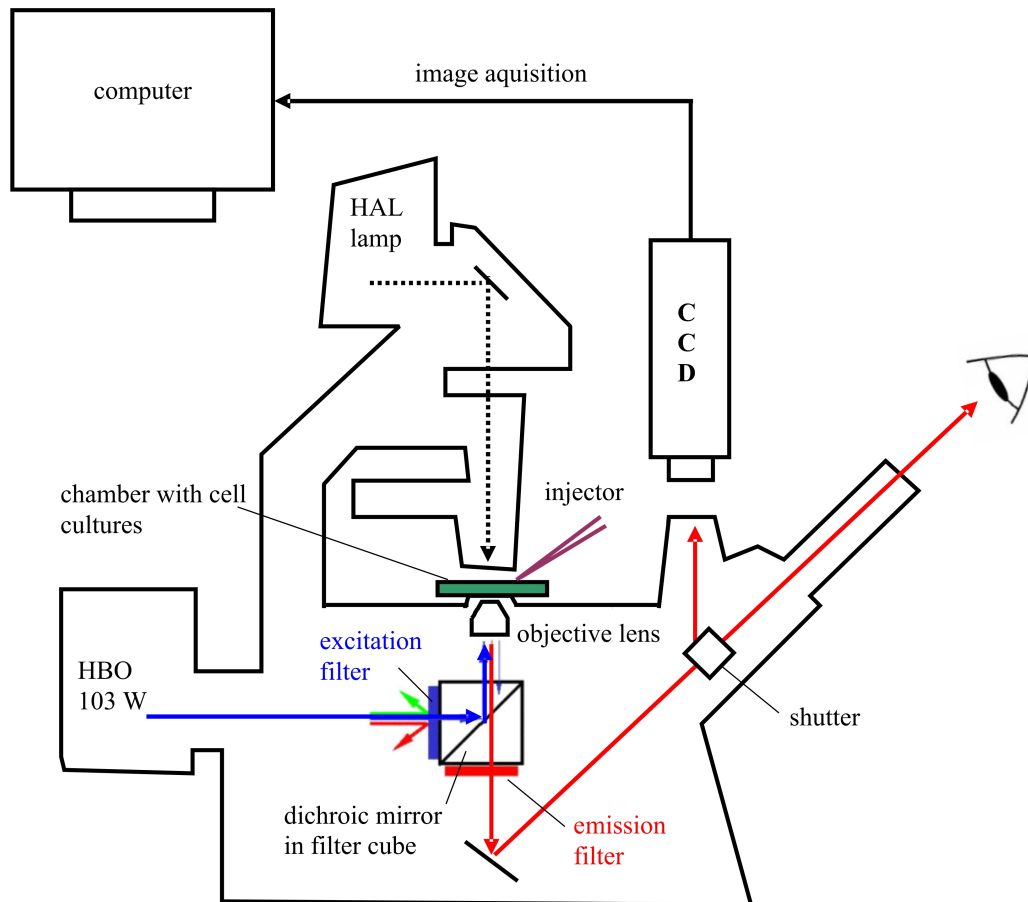
Figure 5.4: Setup for fluorescence image observation. The chamber with cell cultures was placed on the stage of an inverted fluorescence microscope (Axiovert 200 Zeiss). To illuminate the spacimen, light from a mercury lamp (HBO 103 W) was filtered by a band pass filter (excitation filter, 365/12 nm for NAD(P)H and 546/12 nm for protons) before it is reflected at a dichroic mirror in a filter cube to the cell cultures. The emission fluorescence from the cell cultures has a wavelength longer than the excitation light so it can pass the dichroic mirror. To acquire specific fluorescence, the fluorescence was filtered by a banpass filter (emission filter, 397 nm for NAD(P)H and 590 nm for proton) before it was recorded via an image intensified CCD-camera. To observe the transmission image, the cell cultures were illuminated from a halogen lamp at the top, whose light is transmitted through the cells towards the camera.

nm was recorded through a 397 nm long pass filter (Zeiss). Fluorescence images
with an area of $350 \times 400 \ \mu m^2$ were recorded via an image intensified CCD-camera
(Proxitronic) with a rate of 12.5 frames per second. Transmission images were also
taken at the beginning of the experiments in order to locate the cells.

Proton concentration was measured by monitoring the fluorescence of the pH
indicator SNARF-5 (Molecular Probes). This indicator was loaded as the AM ester
derivative of the dye into the cells by incubation for 1 hour, at room temperature.
Excitation light from the mercury lamp was first passed through a neutral density
filter to reduce light intensity and thus photo bleaching then through 546/12 nm
band-pass filters (Zeiss). The emitted fluorescence at 630 nm was detected through
a 590 nm long pass filter (Zeiss).

The fluorescence images from the camera were transferred to a personal com-
puter via a monochrome PCI frame grabber (DT3162, Data Translation) and were
stored as 8-bit grayscale images in TIFF format for further analysis which is de-
scribed in the next section. The acquisition software was written in the graphic
language LabView (written by C. Luengviriya).

At the beginning of the study, experiments were done by using a conforcal mi-
croscope (LSM 510, Zeiss) with Ar/ML 458/477/488/514 laser source. This laser
source provided excitation with four different wavelengths of 457, 477, 488 and 514
nm so that we can perform fluorescence imaging only for pH, not for NAD(P)H.
Note that the excitation of NAD(P)H is about 340-360 nm, as mentioned earlier in
section 4.2. Because protons are non-autofluorescence, we used the dye SNARF-1
AM (Molecular probe) as pH indicator. We excited the dye by using the 488 nm
laser and it emitted visible light with two ranges of wavelengths, as shown in Figure
4.3, section 4.3. To detect the change of fluorescence in these two ranges of wave-
lengths, two optical band pass filters of 535–590 nm and 633–719 nm respectively
were used.

Figure 5.5 presents the light paths in confocal microscopy. In a confocal imaging
system, there are lenses inside the microscope, that focus light from the focal point
of one lens to another point as represented by the solid line. The dashed line
represents light from another point in the sample which is not at the focal point
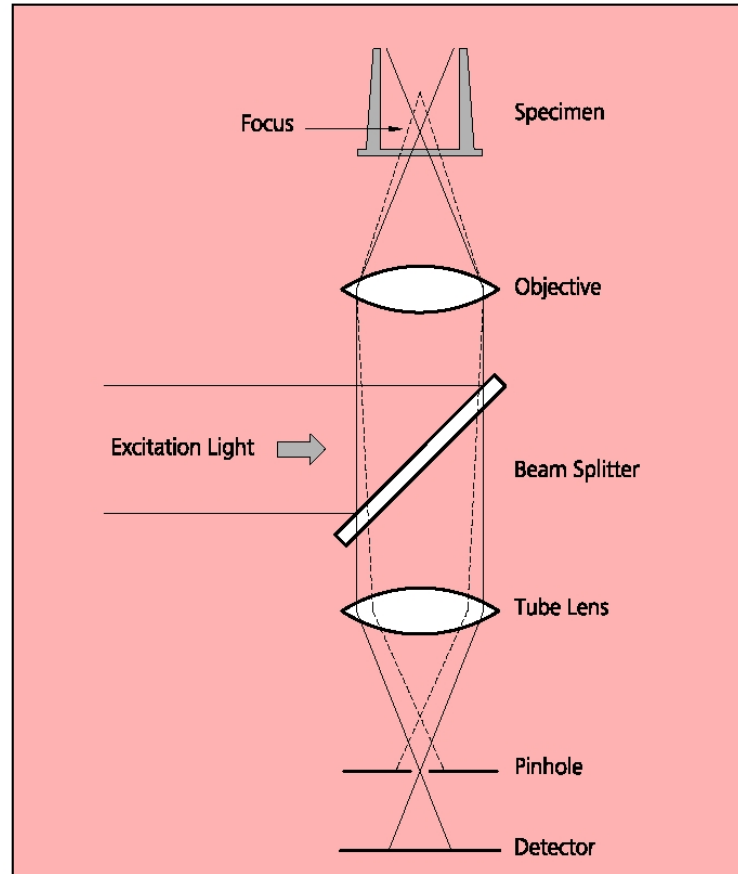
Figure 5.5: Principle of confocal imaging. The light reflected, or the fluorescence light produced, at the focus of the high-NA objective is projected onto a variable pinhole diaphragm by the same objective and a tube lens. The focus inside the specimen and the pinhole are situated at optically conjugate points (confocal imaging). The decisive advantage of this arrangement is the fact that essentially no other light than that coming from the object plane of interest can pass the narrow pinhole and be registered by a detector. Unwanted light coming from other specimen areas is focused outside the pinhole, which allows only a small fraction of it to pass. The smaller the pinhole, the less stray light or fluorescence from out-of-focus areas will get on the detector. The image point thus generated is largely free from blur caused by unwanted light [72].

of the lens but it gets imaged by the lenses of the microscope. There is a screen with a pinhole in front of the detector. Only the focused light can pass through the pinhole and reach the detector. The light from out of focus gets blocked by the pinhole. Because the focal point of the objective lens of the microscope forms an image where the pinhole is, these two points are known as "conjugate points" (or alternatively, the sample plane and the pinhole/screen are conjugate planes). The pinhole is **con**jugate to the **focal** point of the lens, thus it is a **confocal** pinhole.

5.6   Data evaluation

5.6.1   Temporal dynamics of fluorescence

Temporal dynamics of NAD(P)H fluorescence from each individual cell has been investigated by gray level analysis. For this, the fluorescence images were overlaid with the transmission-light image using GIMP program (GNU Image Manipulation Program), which enables the freehand selection of several cells within one image for gray level analysis as shown in Figure 5.6a and b. This allowed us to localize all cells within the observation area and to attribute the fluorescence changes to the identified cells as shown in Figure 5.6c. The gray levels of each cell, exhibiting fluorescence, were averaged and taken as fluorescence intensity (F). This fluorescence value was normalized and then plotted as a function of time, i.e. each image of the image sequence was analyzed in the same way. The normalized intensity of NAD(P)H fluorescence was defined as $F' = (F - F_0)/F_0$, where F_0 is the fluorescence intensity before stimulation of the cells. The response of the cells to the chemical application was quantified by the overshoot amplitude of NAD(P)H or proton fluorescence as shown in Figure 5.6c.

5.6.2   Contrast enhancement

To improve the contrast of the images, the program contrast_overall.pro was applied to the recorded images. First, we defined the recored images during a single experiment as a set of data G. Then the program searched for the minimum (G_{min})
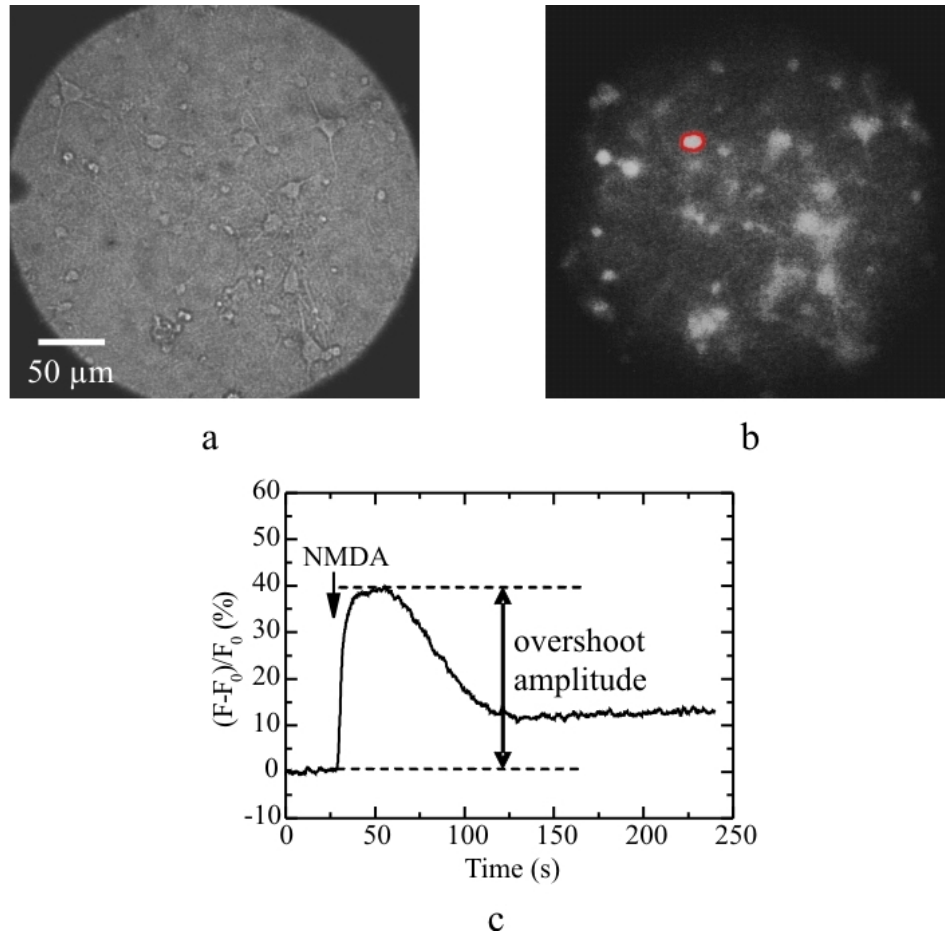
Figure 5.6: Evaluation of temporal dynamics of fluorescence. The cell cultures can be identified in a) the transmission image easier than in b) the fluorescence image of the same observed area. With in GIMP program, the transmission image is overlaid on the fluorescence image and the envelope of the cells is drawn by a freehand function, e.g., the red loop. c) The normalized average fluorescence intensity over time of the marked cell in b). The overshoot amplitude is measured from the initial value to the maximum of the curve.

$$g_n \qquad\qquad g_{n-1} \qquad\qquad \Delta g$$
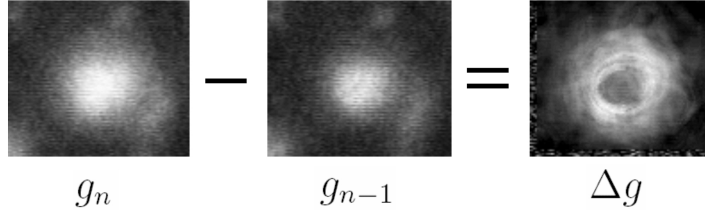
Figure 5.7: Difference of fluorescence images. Travelling waves can be visualized on the different image Δg which is calculated from two subsequent image g_n and g_{n-1} using Eq. (5.2).

and maximum (G_{max}) of the data set G. Finally, each pixel of data set $G(i, j)$ was rescaled to $g(i, j)$ by using Eq. (5.1)

$$g(i,j) \;\; = \;\; 255 \; \frac{G(i,j) - G_{min}}{G_{max} - G_{min}} \tag{5.1}$$

This way the contrast of images is enhanced with the same scaling factor ($(G_{max} - G_{min})^{-1}$), thus, the temporal relation of the image brightness is conserved.

5.6.3   Difference images

The difference (Δg) of two subsequent contrast-enhanced images (e.g., g_n and g_{n-1}) was determined to present travelling waves as shown in Figure 5.7 . The difference Δg was calcualted for each pixel (i, j) using Eq. (5.2).

$$
\begin{aligned}
\Delta g(i,j) \;\; &= \;\; g_n(i,j) - g_{n-1}(i,j) \quad for \quad \Delta g(i,j) > 0 \\
&= \;\; 0 \qquad\qquad\qquad\qquad\;\; for \quad \Delta g(i,j) \le 0.
\end{aligned}
\tag{5.2}
$$

Equation (5.2) implies that only the pixels where the gray level increases are visible on the difference image Δg, while those whose gray level remains or decreases are suppressed (i.e., the gray level is set to zero). Note that before the difference (Δg) was calculated, a median filter with a window width of 9 pixels was applied to the contrast-enhanced images (g_n and g_{n-1}) to reduce noise. The program for this purpose is diff_delay_subvolume_showplus.pro.
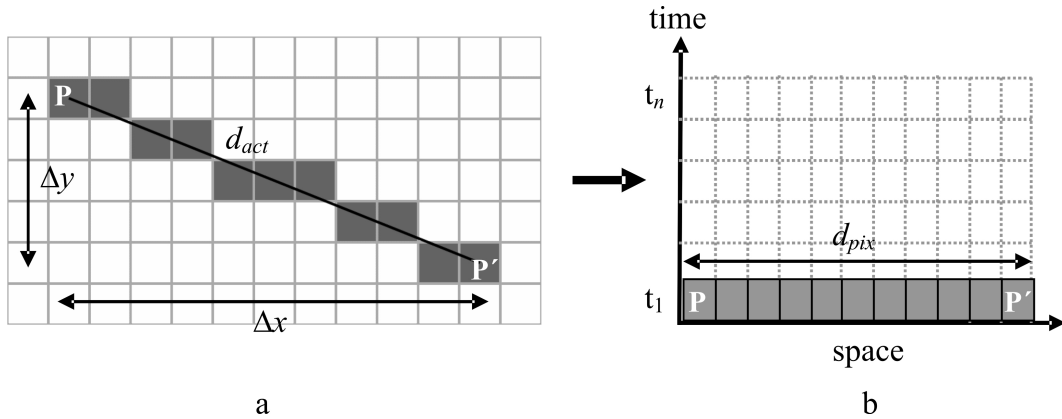
Figure 5.8: Construction of a time-space plot. (a) A set of pixels (in gray) in an fluorescence image is selected by using the Bresenham's line algorithm to present an approximation of a straight line connecting two points P and P′. The actual distance d_{act} between P and P′ can be calculated as $d_{act} = \sqrt{\Delta x^2 + \Delta y^2}$). (b) The selected pixels formed a horizontal line of pixels (from P to P′) and are placed in the time-space plot at time t_1. The same pixels in a series of n-subsequent images recording at time t_1 to t_n are stacked in the vertical direction to complete the time-space plot. Due to the fact that the number of pixels d_{pix} connecting the two points P and P′, in most cases, is higher than the actual distance d_{act}, the horizontal width (d_{pix}) of the time-space plot must be rescaled to the actual distance d_{act} before the plot are utilized for calculating a wave velocity.

5.6.4 Time space plot

The velocity of travelling waves for a certain distance and direction in the recorded images can be estimated using a method of time-space plots. Figure 5.8 shows a construction of such a time-space plot. A straight line (PP′ in Figure 5.8a) was selected parallel to the propagation of the wave (i.e., PP′ was approximately perpendicular to the wave front). Since the images are a set of discrete pixels, the selected line PP′ contains of pixels which, in most cases, are not lying on a straight line, e.g., as shown in Figure 5.8a. In fact, the Bresenham′s line algorithm [73] is used to select the group of pixels (gray pixels) to form an approximation of a straight line connecting the two points P and P′. To construct a time-space plot, the line of selected pixels (gray pixels in Figure 5.8a) is placed along the horizontal direction (i.e., the space axis), at t_1 in Figure 5.8b. The same lines of pixels from subsequent images are stacked in the vertical direction (i.e., the time axis) as $t_2 \ldots t_n$. Since a wave front is a bright front in a dark background, the time

space plot shows an inclined bright line of the propagating front and the velocity of the wave, v, can be calculated as the reciprocal of the slope of the line ($v = 1/\text{slope}$).

We now consider the actual distance d_{act} between P and P′ ($d_{act} = \sqrt{\Delta x^2 + \Delta y^2}$) and the number of pixels (d_{pix}) connecting the two points. If the selected pixels which form the line PP′ lie exactly on a straight line (i.e., PP′ is a vertical line, a horizontal line, or a line with an angle 45° to the horizon), then $d_{pix} = d_{act}$, otherwise $d_{pix} > d_{act}$. In most cases where $d_{pix} > d_{act}$, the width along the horizontal axis (width $= d_{pix}$) of the time-space plot must be rescale to the actual distance d_{act} of PP′ before the velocity of the wave can be calculated correctly.

5.7   Statistics

The results are presented as mean values $\pm$ S.E.M. (standard error of measurement). The significance of differences in the overshoot amplitude of the normalized fluorescence F' at different ages of the cultures was tested using one-way ANOVA (Analysis of variance) with Tukey post-hoc test. The calculations have been done using the commercial software Origin (OriginLab). $P<0.05$ is considered as being statistically significant different. The P-value is the probability of obtaining a result at least as extreme as the one that was actually observed, given that the null hypothesis is true.

One-way ANOVA is a statisical method for testing whether the mean of two or more groups of measured data are equal. Assume that we have k groups of measurements and y_{ij} is the measured value of the ith observation ($i = 1,\ 2,\ 3,\ \ldots\ n_j$) in the jth measurement ($j = 1,\ 2,\ 3,\ \ldots\ k$). The *null hypothesis* states that the means of the different measurements are the same ($\mu_1 = \mu_2 = \ldots = \mu_k$). When the measured data obey the null hypothesis, the statistic F_{cal}:

$$F_{cal} \;=\; \frac{MSTM}{MSE} \tag{5.3}$$

, where

$$MSTM = \frac{\sum\limits_{j=1}^{k} n_j \left(\bar{y}_j - \bar{y}\right)^2}{k-1}, \tag{5.4}$$

$$MSE = \frac{\sum\limits_{j=1}^{k} \sum\limits_{i=1}^{n} {}_j \left(y_{ij} - \bar{y}_j\right)^2}{n-k}, \tag{5.5}$$

will follow an F-distribution. Note that $MSTM$ is the mean squares for treatments and MSE is the mean squares for error, which are derived from the variation "between" the groups and the variation "within" the groups, respectively.

Given a certain significance level α, if the statistic F_{cal} exceeds the critical value $F(k-1, n-k, \alpha)$, which is the tabular value of the F-distribution with $k-1$ and $n-k$ degrees of freedom at level α, or equivalently, the followed P-value, $P[F_{cal} \geq F(k-1, n-k, \alpha)]$, less than the significance level, the null hypothesis should be rejected, i.e., at least the mean of one group differs from the others.

A major limitation of the result from a one-way ANOVA is that it only indicates whether the means are significantly different to each other, however, it does not show how the means differ. To clarify this, we use the Tukey post-hoc procedure which will compare all possible pair of means. For example, given a set of 3 means, the Tukey procedure will compare μ_1 vs. μ_2, μ_1 vs. μ_3, and μ_2 vs. μ_3.

Chapter 6

Results and Discussion

6.1 Preliminary results and remarks

In this section, we want to emphasize that the cell cultures are very sensitive to the transportation. For earlier experiments, the incubator and the experimental setup were in different campuses (the University Campus and the Medical School Campus). Even though we have transferred the cells carefully (which took about 15-20 min by car) using an insulator box, the transportation still disturbed the cells. Most of the cells did not respond to any stimulation.

To minimize the influence of the transportation on the cells, we then performed experiments in the Institute of Biology, Medical School Campus, where the cell cultures were incubated. Thereby, we could carefully transfer the cells from the incubator to the observation setup in a short time. Since a confocal microscope (LSM 510, Zeiss) with Ar/ML 458/477/488/514 laser source was available in the Institute of Biology, we utilized it for observing changes of pH in the cell cultures. As mentioned in section 5.5, we could not detect the fluorescence of NAD(P)H by using this confocal microscope due to the limitation of the laser source.

Figure 6.1 shows an example of the preliminary results. In these experiments, we loaded the dye SNARF-1 to the rat hippocampal cell cultures and stimulated the cell cultures by an application of KCN (0.2 μl of 0.5 M KCN, using an automatic pipet). A laser (488 nm in wavelength) illuminated the sample and the SNARF-1
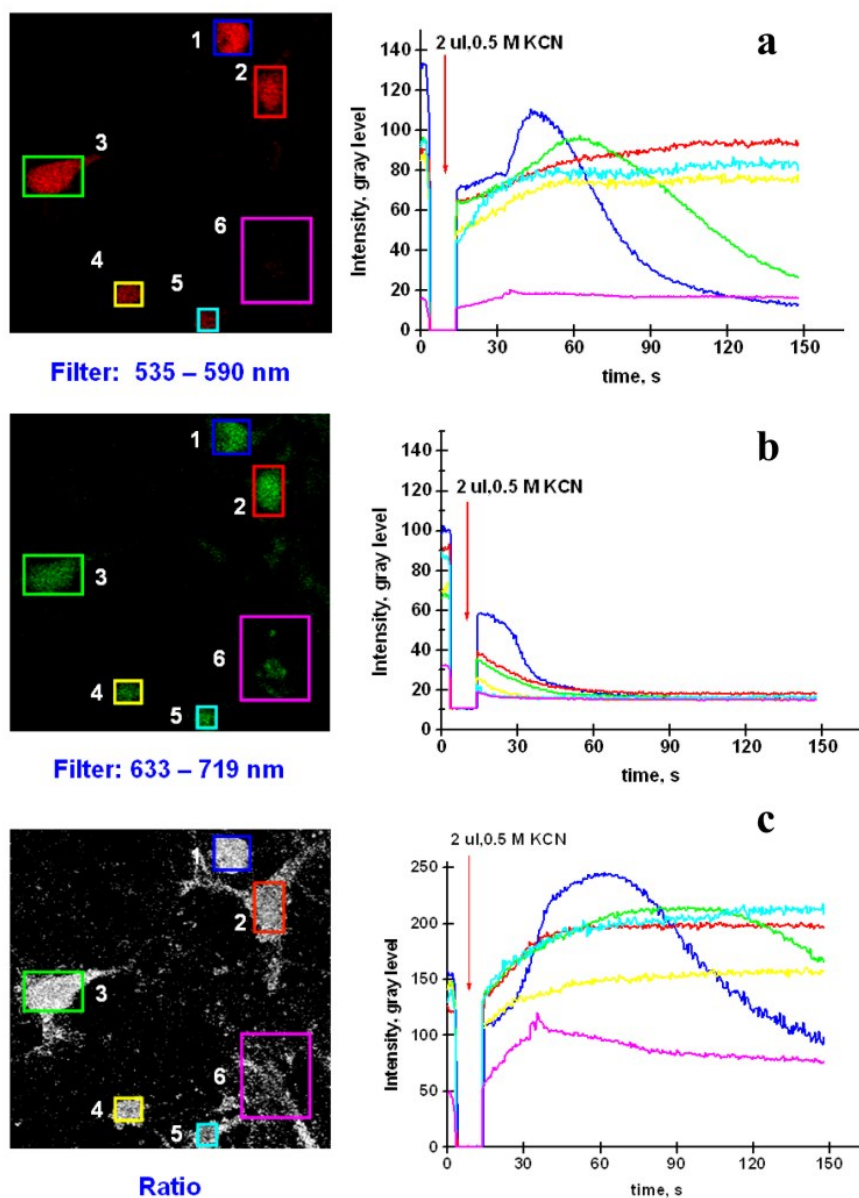
Figure 6.1: Primary results of cell response to KCN. SNARF-1 fluorescence images, which corresponds to the pH value in the cells, were recorded using a confocal microscope with two output channels. After a stimulation by KCN, a) the average fluorescence from channel1 (optical filter = 535–590 nm) increased, b) while that from channel2 (optical filter = 633–719 nm) decreased. c) The ratio of the fluorescence from both channels also increased. The results indicated an accumulation of protons in the cells due to the KCN blockage of mitrocondrial function. The cells and their corresponding plots of intensity are marked with the same color.

fluorescence (with two ranges of wavelengths) was observed at two output channels of the microscope. Figure 6.1a, b show the average fluorescence intensity of the cells from channel1 (optical filter = 535–590 nm) and channel2 (optical filter = 633–719 nm) while Figure 6.1c presents the ratio of fluorescence intensity from channel1 ($Fl1$) to channel2 ($Fl2$). The ratio was calculated as $R = (Fl1+1)/(Fl2+1)+128$. Note that $Fl1$, $Fl2$, and R have a value in the range of 0–255 (8-bit grayscale images). After the application of KCN, the fluorescence intensity from channel1 as well as the ratio R increased while, in contrast, the fluorescence from channel2 decreased. Not that we closed the shutter of the laser beam at 5–15 s to apply KCN using an automatic pipet so that the fluorescence during this interval dropped to zero.

The results in Figure 6.1 can be explained as the following. The KCN blockage of mitrocondrial respiration resulted in an accumulation of both NAD(P)H and protons which were produced by glycolysis (see Eq. (2.1). The accumulation caused an increase in the concentration of protons, i.e., pH decreased. As shown in Figure 6.2, when the pH decreased, the fluorescence intensity with a wavelength less than 630 nm (measured in channel1) raised. On the other hand, the fluorescence intensity with a wavelength higher than 630 nm (measured in channel2) decayed.

A change of SNARF-1 concentration is one possible artifact which may cause the fluorescence from channel1 and channel2 to change while the value of pH still remains constant. We concluded that the change of fluorescence in these experiments due to the effect of KCN and not due to artifacts by two reasons. First, the fluorescence intensity from channel1 and channel2 changed in opposite direction. Second, the ratio of the fluorescence intensity in Figure 6.1c increased. In case that SNARF-1 concentration changes with time while pH is constant, the fluorescence intensity from channel1 and channel2 would change in the same manner because the curves in Figure 6.2 may be shifted up or down with the same function. Further more, the ratio would remain unchanged during the shift of the curves. Therefore, the results indicated the response of the cell cultures to the stimulation of KCN.

The preliminary results convinced us to continue the investigation in the same direction. Accordingly, the fluorescence changes reflect intracellular changes of the
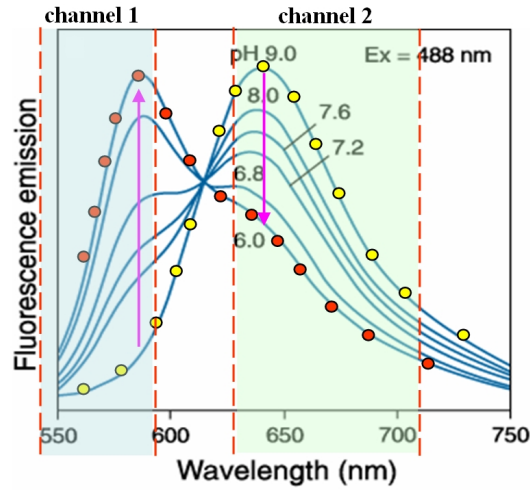
Figure 6.2: Schematic description of SNARF-1 Fluorescence changes in two ranges of wavelengths. In the experiments using a confocal laser scanning microscope with two output channels: channel1 and channel2, the fluorescence intensity from both channels changed in opposite directions. A KCN stimulation caused an increase in the concentration of proton, i.e., pH diminished, and, consequently, the fluorescence intensity for wavelengths < 630 nm (Channel1) increased while that for wavelength > 630 nm (Channel2) decreased.

proton concentration. The results show the temporal dynamics of the intracelluar pH changes. Since the spatiotemporal intracellular patterns have been found to be fast dynamics [10], we decided to use an experimental setup with higher temporal resolution by compared to the confocal laser scanning microscope. For the succeeding experiments, we have improved the speed of fluorescence imaging by using a wide field microscope together with an intensified CCD camera instead of the confocal microscope. We utilized a mercury lamp (HBO 103 W) as the light source. This allowed us to study both protons and NAD(P)H because the spectrum of the mercury lamp covers also the near UV–range, which is required for excitation of NAD(P)H. The chemical stimulations were done closer to the cells (i.e., locally) by using a nano-injector because we wanted to observe the immediate response of the cells to the stimulation. This requires a fast injection of the chemical with concomitant recording of the cellular response. Both is possible when using an injector instead of a pipet.
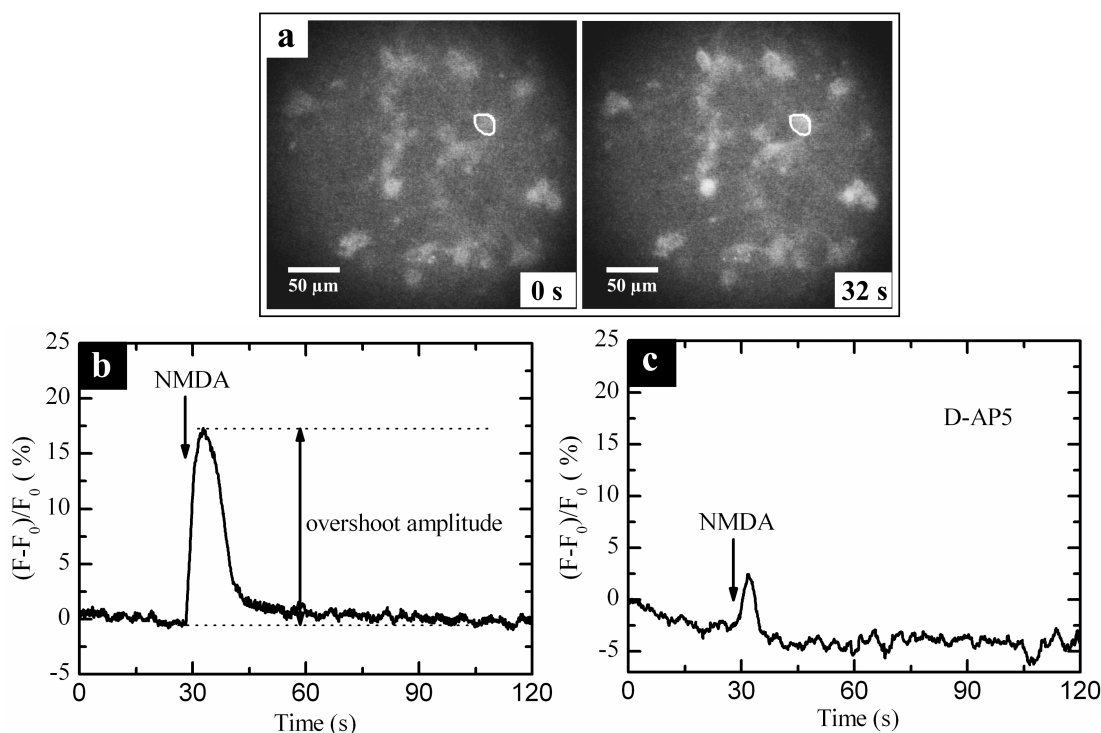
Figure 6.3: NMDA induced increase of cellular NAD(P)H fluorescence. a) Fluorescence image of the cell culture at 19 day *in vitro*. The cell analyzed for temporal fluorescence changes is marked. The images shown were taken before (0s) and after (32s) NMDA injection. b) Temporal changes of the normalized NAD(P)H fluorescence after NMDA injection (60 nl of 25 mM NMDA). The instant of NMDA injection is indicated by a single headed arrow. The overshoot amplitude used for all further analyses is shown. c) Same as b) but in the presence of 50 μM D-AP5.

6.2 NAD(P)H imaging

6.2.1 NMDA-induced activation of the energy metabolism

We have studied the energy metabolism of rat hippocampal cell cultures during neuronal network formation. As a measure of the energy metabolism we recorded the fluorescence of NAD(P)H, which is a common indicator of glycolytic and mitochondrial activity [25–27]. The fluorescence image of the cell cultures illustrates that the NAD(P)H fluorescence is located within the cells and that its intensity varies from cell to cell as shown in Figure 6.3a. Figure 6.3b shows that an activation of neuronal activity by the application of NMDA induces a transient increase in NAD(P)H fluorescence intensity which lasts for about 15 s. This response of the cells to NMDA can be strongly reduced by the NMDA receptor antagonist D-AP5,
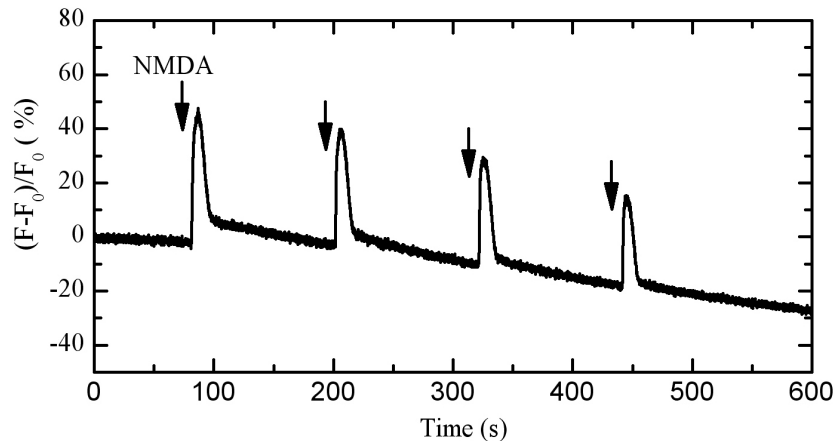
Figure 6.4: Multiple NMDA stimulations. NMDA (50 mM) injection, marked by arrows, have been done every 2 min for 4 times. The fluorescence overshot in every perturbations, however their amplitude decreased with the number of applications.

as shown in Figure 6.3c. The transient nature of this effect is probably due to diffusion of NMDA out of the area of observation. The loss of stimulation leads to a reoxidation of NAD(P)H via the basic turnover of the energy metabolism. Experiments with multiple stimulations support this view. The repeated injection of NMDA evokes every time a transient increase in NAD(P)H-fluorescence (Fig. 6.4). The fact that the magnitude of this fluorescence change decrease with every further injection can be explained by the gradual increase of NMDA with preceding injection. Control experiments demonstrate that the NMDA induced signals are not artificial (Fig. 5.1) .

6.2.2 Optimization of NMDA stimulation

To determine the appropriate volume and concentration of NMDA required to evoke a single stimulation, we first varied the injected volume of a 50 mM NMDA solution from 9 to 74 nl as shown in Figure 6.5a, the overshoot amplitude of NAD(P)H fluorescence intensity and the percentage of responding cells increased with the injected volume of NMDA. Saturation occurs at about 40 nl 50 mM NMDA. For all further experiments, we have chosen 60 nl 50 mM NMDA as an optimal volume for a single pulse.

Next we varied the concentration of NMDA from 12.5 mM to 50 mM and found
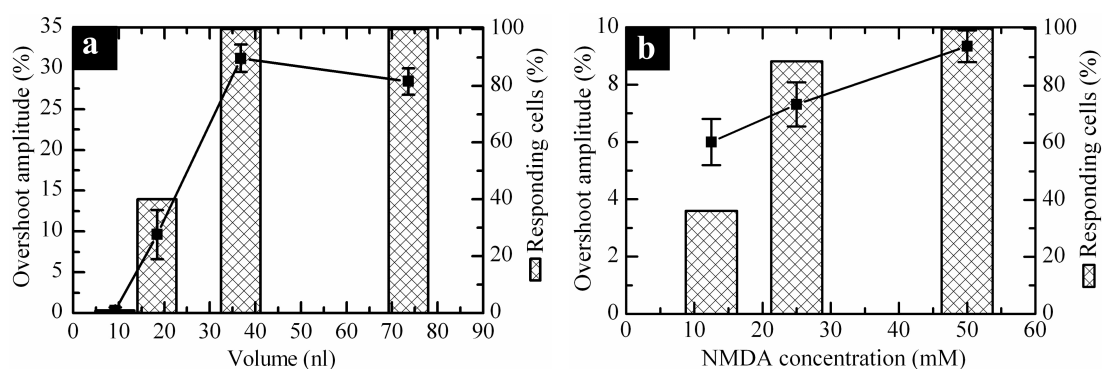
Figure 6.5: Optimization of the conditions for NMDA injection. a) Effect of volume of NMDA solution: Dependence of the overshoot amplitude of NAD(P)H fluorescence (line) and the number of responding cells (columns) on the volume of injected NMDA solution. The concentration in the capillary was kept constant to 50 mM. The age of the cells was 7 days *in vitro*. The bars represent the mean $\pm$ S.E.M of 8-20 cells. The differences in the overshot amplitude between 9nl and 18 nl as well as 18 nl and 36 nl were significant ($P < 0.005$) b) Effect of the concentration of NMDA solution: Dependence of the overshoot amplitude of NAD(P)H fluorescence (line) and the number of responding cells (column) at varying NMDA concentrations. The injected volume was set to 60 nl. The age of the cells was 7 days *in vitro*. The differences in the overshot amplitude between 12.5 mM and 25 mM was not significant ($P > 0.3$), whereas ist was significant between 25 mM and 50 mM ($P < 0.04$).
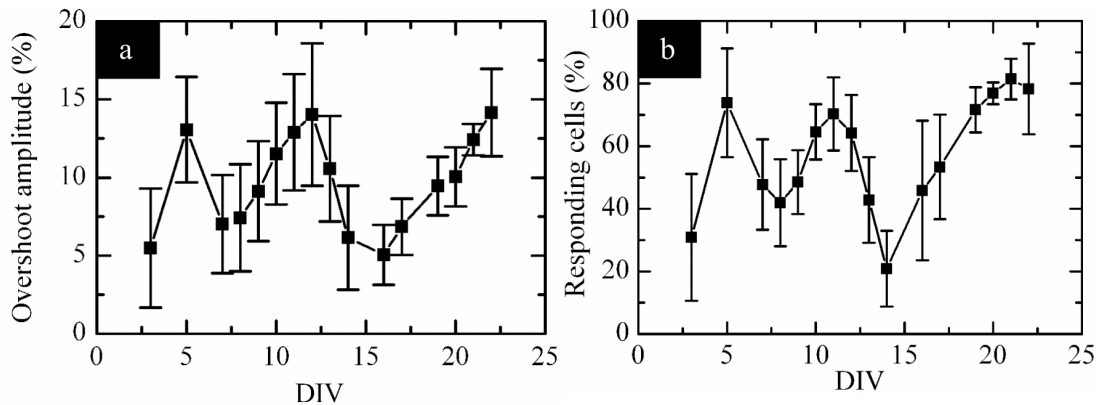
Figure 6.6: Metabolic activation changes with the age of the cell cultures. Cell cultures were taken at different days *in vitro* (DIV) and analyzed for NMDA-evoked stimulation of NAD(P)H-fluorescence as shown in Figure 6.3b. a) Change in the overshoot amplitude as a function of age (DIV). b) Percentage of cells responding to NMDA-stimulation plotted against time of growth. Error bars represent the mean $\pm$ S.E.M of 5 measurements.

a dose-dependent increase of the percentage of responding cells which reached a saturation level at around 25 mM NMDA. To minimize toxic effects of NMDA a concentration of 25 mM NMDA was chosen for all further experiments. Note that the injected NMDA is diluted 5,000 times by injecting 60 nl NMDA solution into 300 μl recording buffer, i.e., the final averaged concentration for a single pulse is 5 μM. After having optimized the conditions for stimulation of the energy metabolism by NMDA-injection, we started to investigate the relation between neuronal activity and energy metabolism during growth of the cell cultures.

6.2.3 Developmental changes in NMDA-induced NAD(P)H responses

The overshoot amplitude changed with the age of the cells as shown in Figure 6.6a. Within 5-22 days *in vitro* (DIV) the overshoot amplitude changed in a biphasic manner with two minima at 7 DIV($7 \pm 3\%$) and 16 ($5 \pm 2\%$) DIV. The occurrence of these minima is statistically significant. All P-values are below 0.0001 when comparing the overshot amplitudes of the minima (7 DIV and 16 DIV) with those of the maxima (5 DIV, 12 DIV and 22 DIV). The growth dependent response of the energy metabolism could be reproduced several times, however with slight

temporal shifts of the minima, depending on the cultures used for the experiments. For the data presented in Figure 6.6, these shifts have been corrected by adjusting the first minimum to the same time instant for all measurements (5 DIV) in order to compare the different data sets. The percentage of responding cells was $74\pm17\%$ at 5 DIV and 77% at 22 DIV, which shows only a slight increase of the number of responsive cells over this culturing period (Fig. 6.6b). At 8 DIV and 14 DIV only $42\pm14\%$ and $21\pm12\%$ of the cells were NMDA responsive (Fig. 6.6). Unlike to the overshot amplitude, the first minimum for responsive cells is not significant ($P > 0.1$) but only the second minimum shows significant differences with respect to the maxima at 11 DIV and 21 DIV ($P < 0.03$).

6.2.4   Testing for metabolic performance

The measured age dependent changes in the cellular energy metabolism evoked by NMDA stimulation can be interpreted by different mechanisms: a) they might either reflect developmental changes such as the increase in the complexity of synaptic wiring, changes in the expression of NMDA receptors or other receptor types, etc. or b) the energy metabolism itself undergoes developmental changes during neuronal network formation. Therefore the metabolic performance of the cells was tested by applying KCN to the cells. KCN induces a block of mitochondrial respiration with concomitant accumulation of NAD(P)H [22]. We expect that there is a direct relation between the energy flow, i.e., glucose oxidation, and mitochodrial respiration. Thus the increase in NAD(P)H after the cyanide block can be taken as an indicator of the extent of this energy flow. Similar to NMDA stimulation, NAD(P)H fluorescence intensity increased immediately after cyanide application as shown in Figure 6.7b. However, in contrast to NMDA stimulation, KCN evoked responses in 100% of the cells in all experiments and at all developmental stages (see Figure 6.7a). Moreover, the temporal dynamics of the NAD(P)H-response was different. Whereas the velocity of the increase in fluorescence intensity was similar (0.079 s^{-1} vs 0.054 s^{-1} for KCN and NMDA, respectively), the decrease in fluorescence intensity was one order of magnitude lower for KCN (0.0034 s^{-1} vs
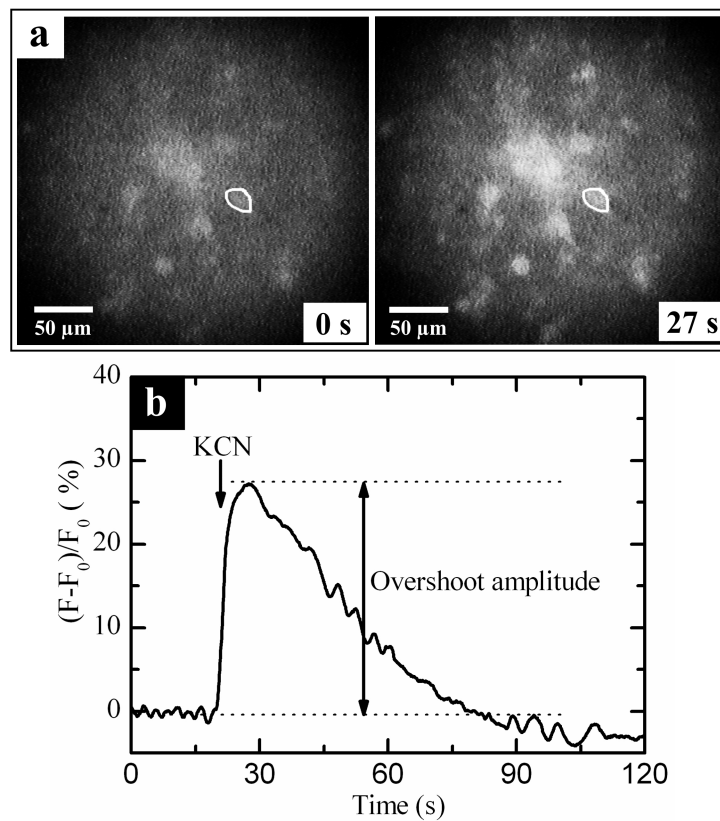
Figure 6.7: Effect of KCN on cellular NAD(P)H fluorescence. The experiments were performed as described in Figure 6.5 except that 60 nl 0.5 M KCN was applied (final concentration is 0.1 mM). The age of the cells was 10 DIV. The fluorescence images of the cells before (0 s) and after (27 s) KCN injection is shown in a, whereas the intensity changes for a single cell, marked in a, is shown in b.
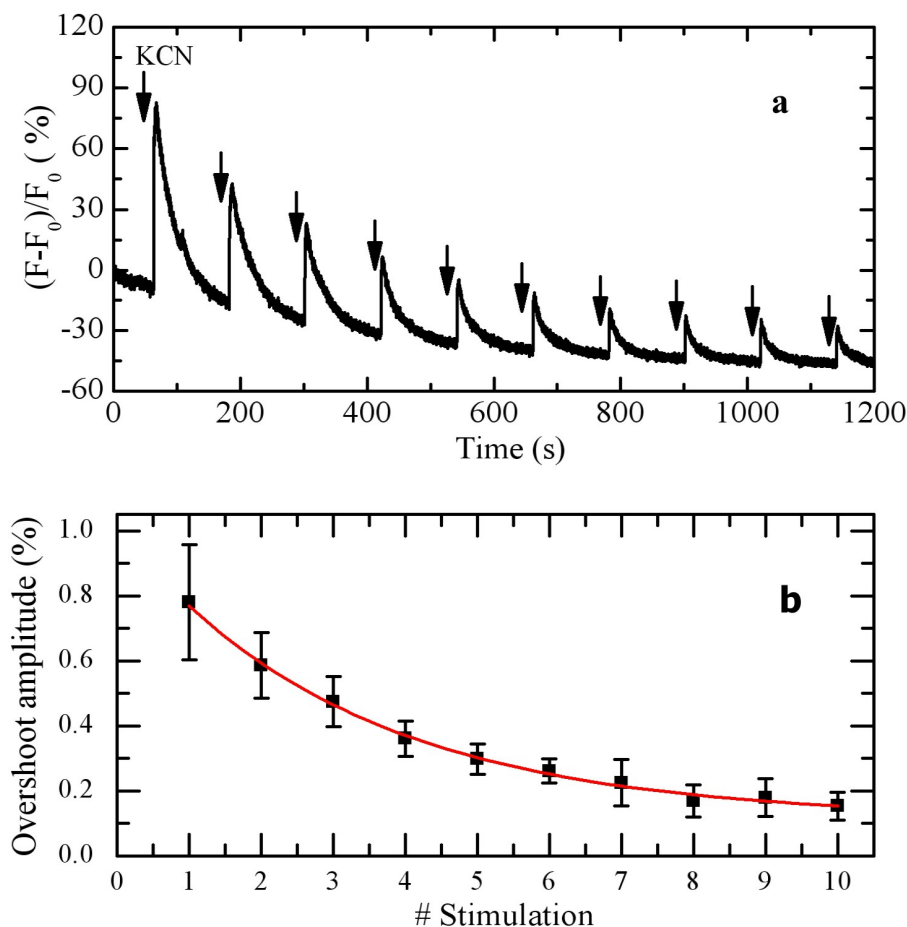
Figure 6.8: Multiple KCN stimulations. KCN (70 nl 0.5 M) injection, marked by arrows, have been done every 2 min for 10 times. a) normalized NAD(P)H fluorescence and b) the overshoot amplitude of the fluorescence.

0.023 s^{-1} for KCN and NMDA, respectively).

We have also investigated the effect of multiple KCN stimulations. In this experiment, KCN applications have been done every 2 min for 10 times. The fluorescence intensity overshot in every perturbation as shown in Figure6.8 a. However, the overshoot amplitude of fluorescence (A) decreased as an exponential function of the perturbation number (x): A = 0.89 exp(-x/3.19)+ 0.11 (Fig. 6.8 b).

The effect of KCN showed developmental changes (Fig. 6.9). An increase in the overshoot amplitude was observed between 5 DIV to 7 DIV ($19 \pm 0.8\%$ to $24\pm0.9\%$ $P < 0.001$) followed by a plateau between 7 DIV and 15 DIV (($25\pm1.2\%$) all P-values larger than 0.05). Between 16 and 25 DIV there is a steep decrease in amplitude down to 10% ($P < 0.0001$ for DIV 15-18; $P > 0.9$ for DIV 18-22, and
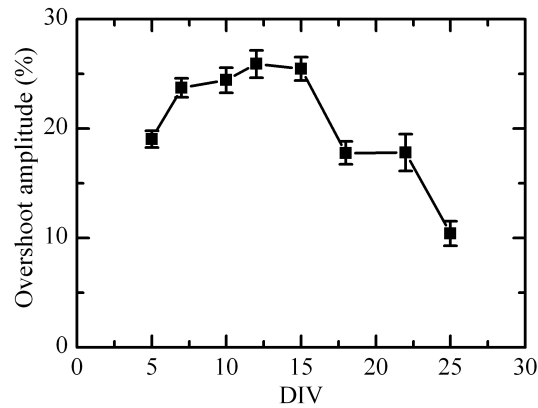
Figure 6.9: Dependence of the KCN effect on age of the cells. The experiments were performed as shown in Figure 6.7. The overshoot amplitude is plotted as a function of the age of the cells. The percentage of responding cells in every experiment was 100%. Error bars represent the mean $\pm$ S.E.M of 24 to 50 cells.

$P < 0.004$ for DIV 22-25).

6.2.5 NMDA-evoked NAD(P)H responses during respiratory block

The change in NAD(P)H-fluorescence intensity is taken as an indicator of the energy metabolism. However, it is not possible to distinguish between the glycolytic or/ and mitochondrial contribution to this change. In order to get an estimation about this, the contribution the mitochondrial respiration was blocked by addition of 2 mM KCN to the recording medium (cf [22]), and the cells were incubated for 4 minutes in this solution. Subsequent injection of 60nl of 25 mM NMDA to the cells still did evoke an increase in the cellular NAD(P)H-fluorescence, indictating that the NMDA-effect is mainly due to stimulation of glycolysis. Similar to the results shown in Figure 6.6, this stimulation also induced developmental changes in the presence of KCN. The NMDA-evoked overshoot amplitude in cells with blocked respiration and in cells without KCN addition during the first 3 weeks *in vitro* is shown in Figure 6.10. First, in both cases we find two minima, where the differences between the minima and maxima are significant for both curves ($P < 0.01$). The first minimum is located at 7 DIV (18 ± 1.1) for the respiratory cells and at 9 DIV (16 ± 0.8) for the glycolytic cells. The second minimum is centered at 16 DIV for
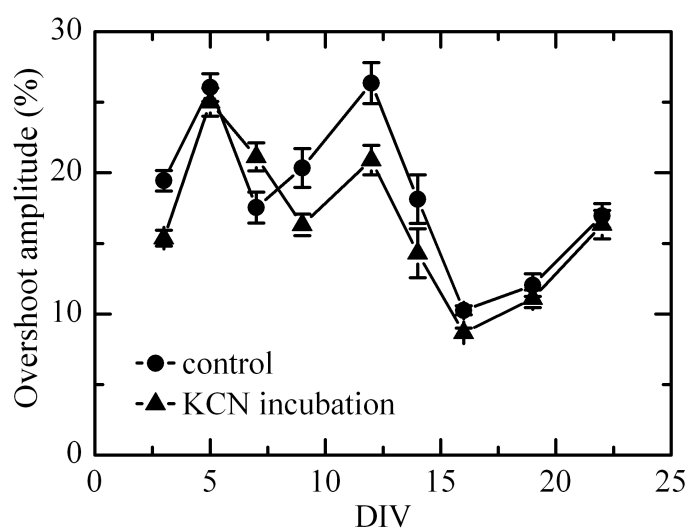
Figure 6.10: Effect of NMDA on the energy metabolism of aerobic and anaerobic cell cultures. The experiments were performed as following. First, the cells were incubated in recording medium and 60 nl 25 mM of NMDA was injected while the NAD(P)H fluorescence was measured (circles). Subsequently, the recording medium was carefully removed and replaced by recording medium including 2 mM KCN. The same cells were then incubated for 4 min with KCN before another NMDA injection (60 nl 25 mM) was done (triangles). The results show the normalized NMDA evoked overshoot amplitude, as defined in Figure 6.3 . Error bars represent the mean $\pm$ S.E.M of 23 to 76 cells.

both cell types (9 ± 0.3). Second, the differences between these two curves from DIVs 6 to 16 are small but significant ($P < 0.02$) except for DIV 14 ($P > 0.1$). At all other DIVs the differences between the curves of the control and KCN inhibited cells are not significant ($P > 0.1$).

6.2.6 Discussion

NMDA-evoked stimulation of cellular NAD(P)H-fluorescence

The presented results demonstrate that hippocampal cell cultures from newborn rats respond to a local NMDA stimulus with an increased activity of the energy metabolism, as measured from changes of the cellular NAD(P)H fluorescence. During the first three weeks *in vitro*, the magnitude of this response depends on the age of the culture and follows a biphasic shape with two minima at DIV 7 and DIV 16. This behavior is only slightly affected by the blockade of mitochondrial respiration by KCN. On the other hand, a blockade of the NMDA-receptor by the NMDA-antagonist AP-5 leads to a nearly complete inhibition of the response, demonstrating its specificity.

The NAD(P)H fluorescence in brain slices from adult rats in response to electrical stimulation and/or receptor activation has been studied previously [21, 74, 75]. In these studies biphasic responses, consisting of an initial dip component (decrease of fluorescence intensity) and a subsequent overshoot component, of the fluorescence signal have been found.

We found a different behavior when using cell cultures from the hippocampus of newborn rats instead of brain slices from adult rats, we observed only a transient increase in NAD(P)H fluorescence with no indication of a two-phase response, i.e., we observed only the overshoot component. These discrepancies might be due to the different developmental status of the tissue preparation. Compared to adult brain slices the cells in our dissociated primary cultures from newborn rats are still immature (even at 22 DIV) and the development of neuronal network connectivity, including the expression of glutamatergic receptors, is continuing during the cultivation period (A.K. Braun, personal communication). Moreover, acute brain

slices from adult rats most likely display a tighter coupling between neuronal and glial cells than present in our dissociated cultures from neonatal rats. On the other hand, the two-phase behavior is not seen in all hippocampal subregions, since it has been shown that some hippocampal regions only display the initial dip component [21].

Developmental changes of the energy metabolism

NMDA-evoked stimulation of the energy metabolism at different growth times, starting from 3 DIV to 22 DIV, underlies strong developmental changes, and both, changes in the overshoot amplitude as well as in the percentage of responding cells followed similar developmental profiles. From 3 DIV to 5 DIV the overshoot amplitude increased to values from $5 \pm 4\%$ to $13 \pm 3\%$. It remained nearly at this level ($14 \pm 5\%$ at 12 DIV and 22 DIV). This developmental course showed two minima: one at 7 DIV ($7 \pm 3\%$ overshoot amplitude) and the second at 16 DIV ($5 \pm 2\%$ overshoot amplitude).The biphasic profile of overshoot amplitudes may indicate a "silencing" of metabolic activation during specific developmental time windows during which neuronal and synaptic reorganization takes place. Such time windows have also been detected for other neuronal parameters during hippocampal development. For instance, Kudryashov et al. [36, 37] showed that population spike amplitude increased until postnatal day 19, thereafter decreased to a minimum at postnatal day 21- 24 until it increased again to adult levels. A study by Collard et al. [35], measuring glutamate release after K^+-depolarization in hippocampal synaptosomes, observed a dampened K^+-evoked glutamate response at postnatal day 7 and between postnatal day 14 and 16, after which the glutamate response increased again to adult levels. A recent study by Gruss et al [76] found that emotional reinforcement of late-long term potential (LTP) was specifically prevented in adolescent rats, which had been exposed to maternal separation stress at postnatal day 9, but not at other time points.

Kudryashov et al. and Collard et al. argue that these minima in either population spike amplitude or glutamate release result from maturation processes of the early postnatal brain. It is unlikely that the developmental changes observed in

our cultures are due to LTP induced changes of network connectivity. Therefore, we tested whether the observed developmental patterns evolve solely from changes of the energy metabolism, i. e., whether they are independent of activation by NMDA. Indeed, the energy flow, as estimated by cyanide induced accumulation of NAD(P)H, exhibits developmental changes. However, this change follows a bell-shaped curve during the first three postnatal weeks and is thus different from the biphasic patterns obtained by NMDA application. Hence, the growth dependent changes of the energy metabolism alone may participate but cannot be the exclusive reason for occurrence of the biphasic behavior, as it is observed for the NMDA triggered NAD(P)H-fluorescence change. From this we may conclude that activation of the NMDA-receptor, either in neurons, or glia cells or in both, is required to produce the observed biphasic patterns in the energy metabolism. Moreover, the similarity of the developmental patterns of the activity of neurons [35–37] and the NMDA-evoked metabolic responses in our cultures indicate that both phenomena might reflect reorganization of neurons and their synaptic circuits. Accordingly, the decrease of neuronal connections at 7 DIV and 16 DIV may account for the decrease in NMDA-induced NADPH-response due to dampened neurometabolic coupling between neurons and glia cells and thereby reduced metabolic response towards NMDA.

NMDA-receptor activation in the presence of KCN

We have taken NAD(P)H as an indicator of the energy metabolism, but this does not allow a distinction between aerobic, i. e., mitochondrial, and anaerobic, i. e. glycolytic, energy production. In general, NAD(P)H is thought to originate mainly from the mitochondrial energy metabolism, but Yamane et al [77] have shown that also the anaerobic, i.e., glycolytic, energy metabolism is important for maintenance of neuronal functions. Kasischke et al [22] also reported NAD(P)H-fluorescence changes as a result of glycolytic activity, however, mainly for glia cells and not for neurons. Kahlert and Reiser [78] found that glycolytic and to a lesser extent also mitochondrial ATP is required for loading of intracellular Ca^{2+} stores of hippocampal astrocytes.

In order to narrow the possible source of the NAD(P)H signals in our cell cultures we applied NMDA to cells whose respiration had been blocked by KCN. Under this condition, there is only a slight reduction of the NMDA-evoked overshoot amplitude. Moreover, the biphasic pattern with the two minima around DIV 7 and DIV 16 can also be observed. Since addition of cyanide completely blocks energy production by mitochondria, the observed changes in the NAD(P)H signals result mainly from glycolysis. This is in agreement with an earlier study from Zhan et al.[34]. They found an NMDA-induced intracellular acidification in hippocampal slices. They attributed this NMDA-induced acid shift to glycolysis because the the shift was reduced in the presence of the glycolytic inhibitor fluoride or when glucose was substituted by pyruvate. Further support for this view comes from the results from Shuttleworth et al. [21]. In agreement with the hypothesis of neurometabolic coupling [23, 24] Shuttleworth et al. found that the activity of the plasma membrane ATPase significantly contributes to stimulus evoked NAD(P)H signals in brain slices. From their results they conclude further, that mitochondrial functions are not required for the NAD(P)H transients. This is in agreement with our findings, since NMDA can evoke the NAD(P)H transient also in cyanide inhibited cell cultures.

Another interesting conclusion can be drawn, when comparing the developmental changes of the NMDA-evoked overshoot amplitude with those of the KCN-evoked overshoot amplitude. While the NMDA-evoked overshoot amplitude starts to increase during the third week *in vitro*, the KCN-evoked overshoot amplitude shows the opposite behavior, it declines to minimal values. If we take the KCN-evoked signal as an indicator for the mitochondrial activity, these data indicate that the glycolytic energy production increases during the development of neuronal networks with respect to the mitochondrial one.

Taken together, our results demonstrate that the energy metabolism of hippocampal cell cultures undergoes strong changes during the development of neuronal networks, fostering the idea of energy supported network formation. The observed changes seem to originate mainly from the glycolytic pathway, although additional alterations of other pathways, affecting the efficiency of the neurometabolic
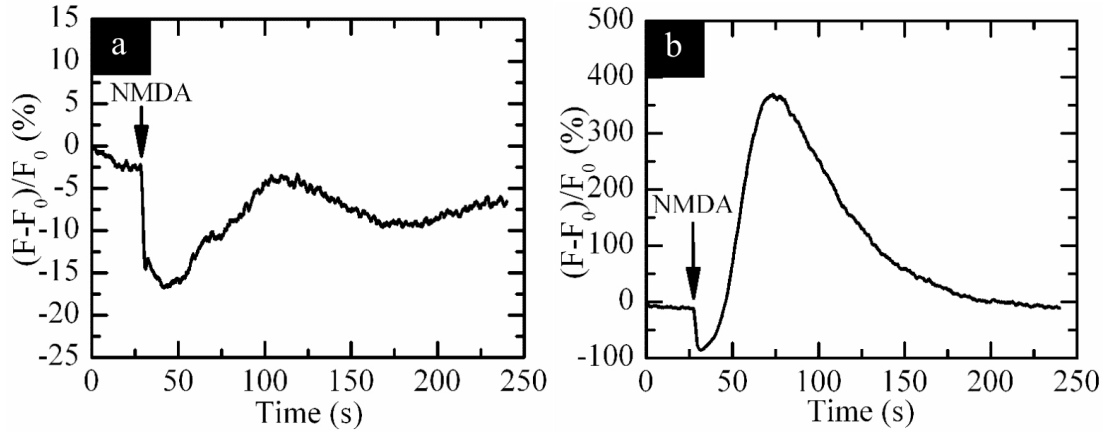
Figure 6.11: Two kinds of temporal dynamics of pH_i in hippocampal cell cultures after NMDA stimulation. Note that the injected NMDA is diluted 5,000 times by injecting 60 nl 25 mM NMDA solution into 300 μl recording buffer, i.e., the final averaged concentration for a single pulse is 5 μM. a) An acidification: the fluorescence decreased and then slowly increased to the initial value. This behaviore occurred in the cells grown no longer than 14 DIV. b) A biphasic change: in the cells grown form 14 DIV to 22 DIV, the fluorescence dip slightly and subsequently overshot with substantially higher amplitude. The graphs show normalized fluorescence of SNARF-5F which is a pH indicator.

coupling, can not be excluded.

6.3 Intracellular pH imaging

6.3.1 NMDA-induced temporal intracellular pH dynamics

We utilized intracellular pH (pH_i) imaging to study the energy metabolism of rat hippocampal cell cultures during neuronal network formation. We have studied the temporal pH_i dynamics in cell cultures between 3 to 22 days *in vitro* (DIV). A chemical stimulation of neuronal activity by NMDA application induced two kinds of temporal dynamics of pH_i , i.e., an intracellular acidification and a biphasic change, as shown in Figure 6.11). For the intracellular acidification (Fig. 6.11a), the fluorescence intensity of SNARF-5F decreases to a minimum (20-60 %) before it returns to the initial value. The biphasic change (Fig. 6.11b) is characterized as an initial transient acid shift (40-100 %) followed by a long lasting alkaline shift (400-1400 %). These temporal dynamics of pH_i depend on the age of the cells. For
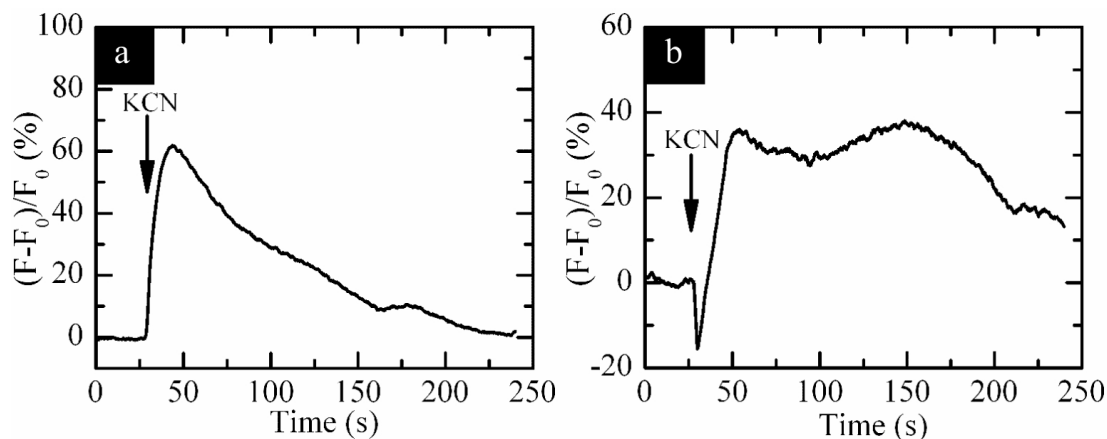
Figure 6.12: Temporal dynamics of intracellular pH in hippocampal cell cultures after 60 nl 0.5 M KCN application (final concentration is 0.1 mM). The graphs show normalized fluorescence of SNARF-5F which is a pH indicator. Two different dynamics are shown: a) Fluorescence overshot and subsequent decrease. b) the fluorescence dip slightly and subsequently overshot with a higher amplitude.

3-14 DIV, most of the observed cells (80-100 %) showed an acidification while the rest (up to 20%) showed the biphasic change. After 14 DIV, we observed only the biphasic pattern in all of the cells.

6.3.2 Temporal dynamics of intracellular pH evoked by KCN

After an application of KCN, we observed two different kinds of temporal dynamics of pH_i, i.e., an alkalization in which the fluorescense overshot (60-700%) and subsequently decay to the initial value (Fig. 6.12a) and a biphasic change (Fig. 6.12b) with a tiny dip (20-100%) followed by a high overshoot (40-1300%). Also in this case, the temporal dynamics of pH_i depend on the age of the cells. During the first three weeks *in vitro* (3-22 DIV), most of observed cells (60-100 %) showed the biphasic change while the rest (up to 40%) showed the alkalinization except at 14 DIV where all cells (100%) showed the alkaline shift. In control experiments we checked that the response of the cells to KCN addition is no artifact. When the cells were pre-incubated for 4 min with 2 mM KCN, the response of the cells to NMDA application was the same as in the absence of KCN, demonstrating that the cells were not poisoned during these 4 min.
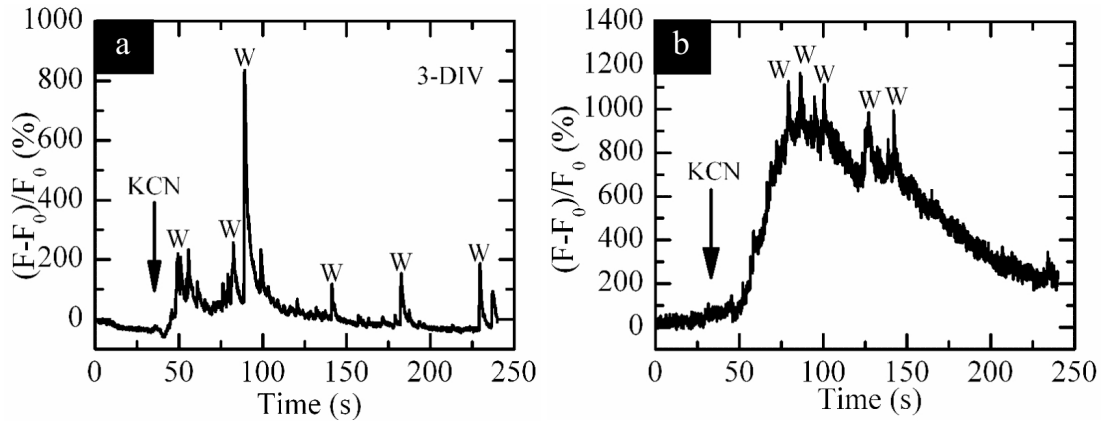
Figure 6.13: Repetitive pH_i spiking in a single cell. A local injection of 60 nl 0.5 M KCN (final concentration is 0.1 mM) evoked both a change in the fluorescence of background intensity of the cells (the low frequency component) and a pH_i spiking. Each spike corresponds to the generation of wave, indicated by w. a)The fluorescence changes after KCN application in the cells at 3 DIV. b) The fluorescence changes after KCN application in the cells at 19 DIV.

6.3.3 Spatiotemporal dynamics of intracellular pH evoked by KCN

Intracellular pH waves

At 3 DIV and after 14 DIV a pH_i-spiking activity was superimposed on the biphasic response (Fig. 6.13). It was during this pH_i-spiking that traveling waves occurred. The traveling pH_i waves appeared as small dots and then propagated to the neighboring regions. Figure 6.14 shows a circular pH wave. The wave emerged at the middle of the cell and spread outwardly (the top row in Figure 6.14), however, only for a restricted spatial length corresponding to the size of one cell (50 μm). We estimated the wave velocity along a linear path (e.g., the segment PP' in Figure 6.14) using a time-space plot method as shown in Figure 6.15. The results show that the velocity of pH waves in individual cells is in the range of 60-110 μm/s.

The pH waves were observed to occur repeatedly as shown in Figure 6.13 (labelled as w). Both curves of the fluorescence intensity of a single cell in Figure 6.13a and 6.13b can be decomposed into two parts - background and wave components. At early stages of growth (3 DIV, Figure6.13a) the background intensity of the cell
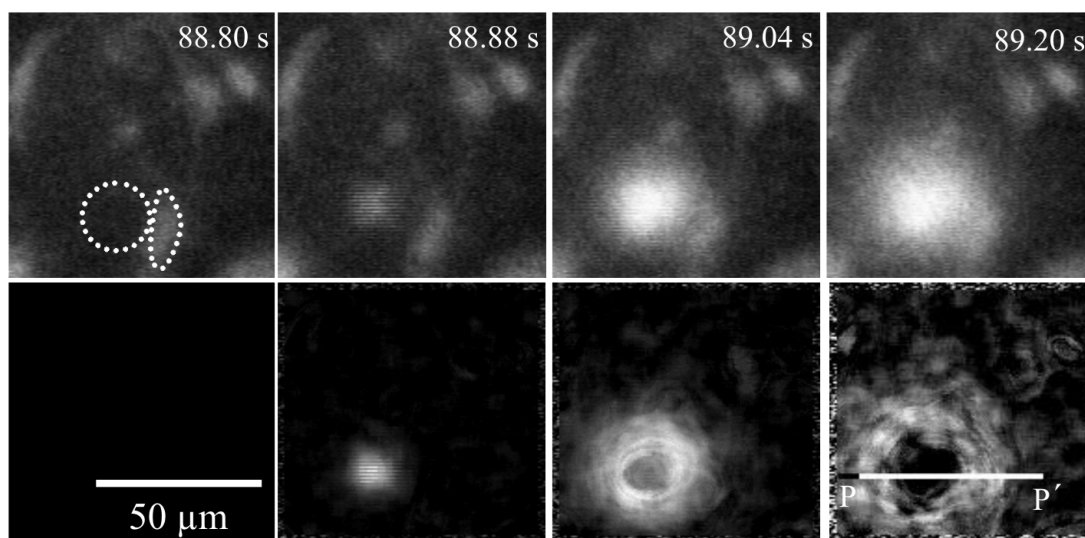
Figure 6.14: Propagating circular pH wave in a single cell. For comparison, the shape of two cells is marked by dotted loops. Top row: Fluorescence images after an application of KCN (60 nl/0.5 M, final concentration is 0.1 mM) show an expanding circular wave. Bottom row: To illustrate the propagating front, difference images were calculated as difference [image$_n$-image$_{(n-1)}$] of the adjacent images in top row. The pixels along a straight line PP$'$ were used to construct a time-space plot as shown in Figure 6.15. The age of the cells was 3 DIV.
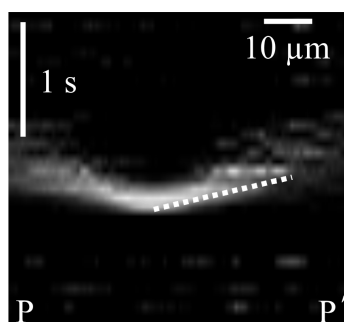
Figure 6.15: Determination of wave velocity using a time-space plot method. The pixels along the path PP$'$ in Figure 6.14, bottom row, were stacked from the bottom to the top with respect to time. The reciprocal of the slope of a linear regression (the dashed line) corresponds to the wave velocity. It is 109 μm/s.
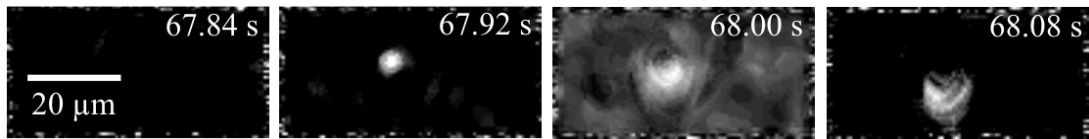
Figure 6.16: Traveling crescent-shaped wave in a single cell. Difference images were calculated to show the propagating front. The calculated velocity is 60 μm/s. The age of the cells was 5 DIV.

nearly doubled after KCN addition, whereas at later stages of growth (19 DIV, Figure 6.13b), it increased about 10 times.

A crescent-shaped wave also occurred, when the wave did not start at the middle of the cell but emerged near one edge of it (Fig.6.16). In this case the wave propagates only in one direction and is annihilated at the opposite cell pole.

Network oscillations

The pH$_i$ waves did propagate only through a single cell and could not cross the cell membrane (cf.Figure 6.14). However, it is likely that the waves induced a communication between the cells because we always observed spatiotemporal oscillations of cell clusters, provided that intracellular waves had been generated. An exampale is given in Figure 6.17. The cells in the dashed boxes (labeled 1-4) repeatedly exhibited circular waves. This occurred randomly with small time delays, thus giving rise to spatiotemporal oscillations. Figure 6.18 shows the fluorescence intensity changes of the cells labelled 1-4 in Figure 6.17. After an application of KCN, the fluorescence intensity slightly dropped (20-40%) before it overshot with a larger magnitude (50-200%). Subsequently, the fluorescence in the four cells oscillated in a complicated manner, i.e., with varied amplitudes and frequencies. The peaks with the same label (1-7) seem to appear in the graphs at nearly the same time with only small time delays of 0.08-4.52 s. However, there was no ordered time delay between the cells, i.e., it did not result from wave propagation.

Initial fluorescence

Interestingly, the occurrence of the intracellular pH waves as well as the network oscillations were related to the initial fluorescence intensity of the cells. They occurred mainly in those cells whose initial fluorescence intensity was low (e.g., the cells in the dashed boxes labelled 1-4 in Figure 6.17). The cells with high
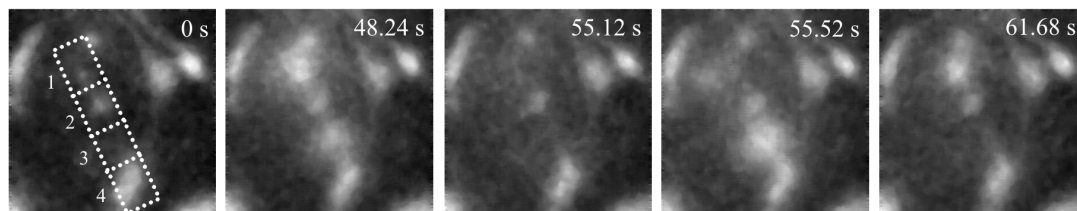
Figure 6.17: Network oscillations. Time sequence showing intracellular pH waves within each cell in the dashed boxes (labeled 1-4) exhibited waves repeatedly.
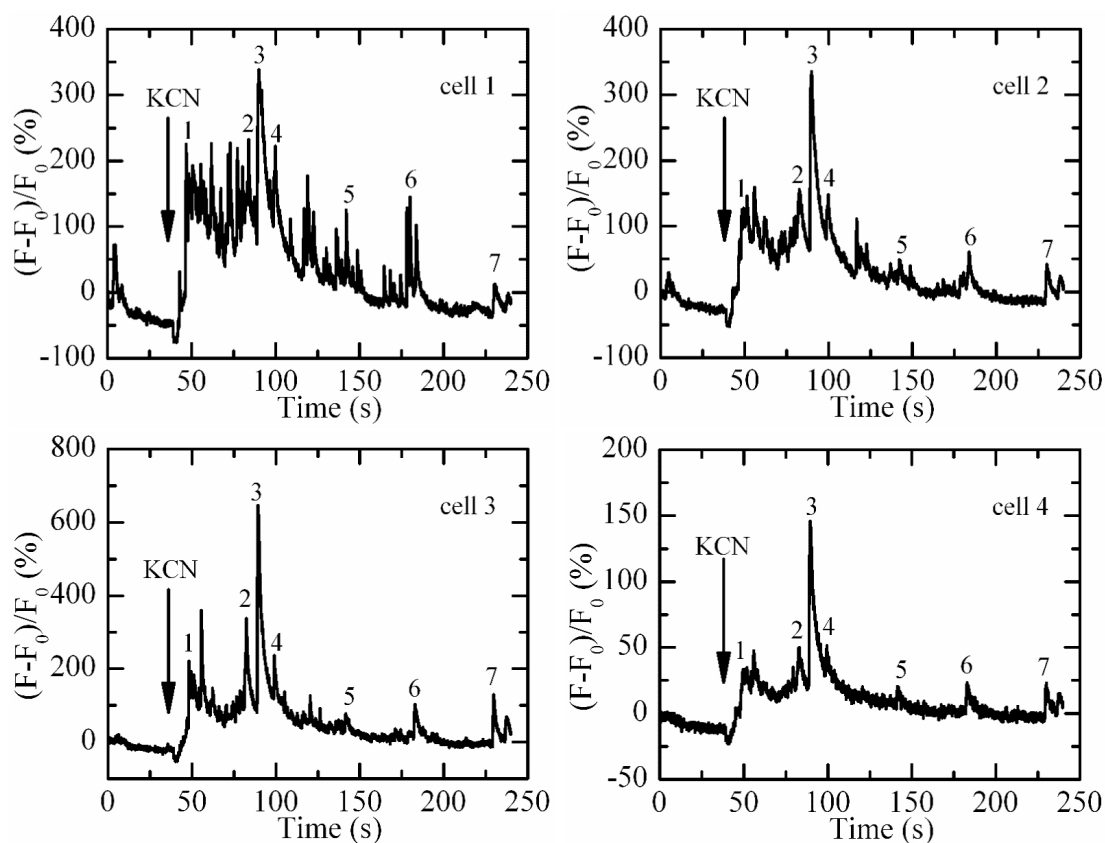
Figure 6.18: Average fluorescence intensity of cell 1-4. Fluorescence changes measured over image areas indicated by boxes in Figure 6.17 before and after local injection of 60 nl 0.5 M KCN (final concentration is 0.1 mM).
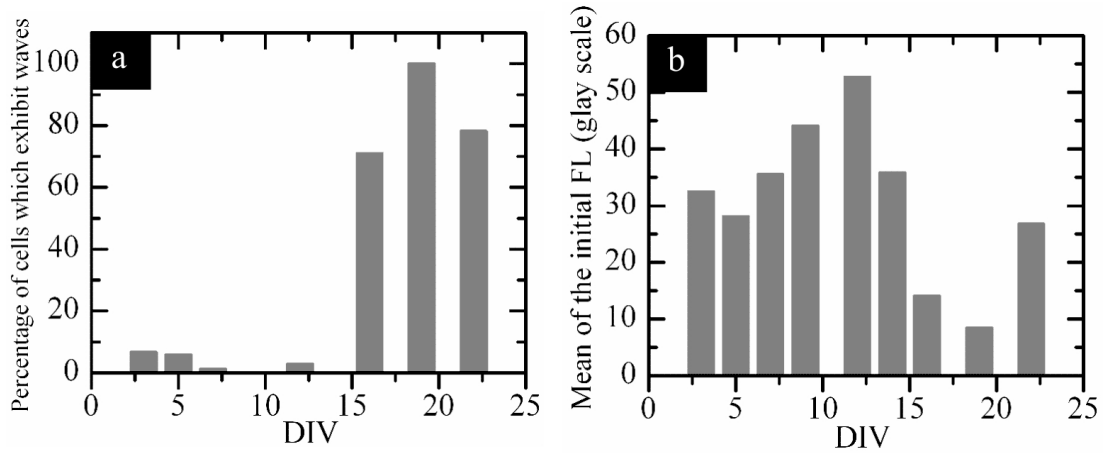
Figure 6.19: Relation of the initial fluorescence and the pH_i dynamics. a) Percentage of cells which exhibit waves after KCN application plotted against time of growth. b) Mean of the initial fluorescence before any application plotted against time of growth.

initial fluorescence exhibited only the two kinds of temporal dynamics as shown in Figure 6.12.

The pH_i waves were mainly observed after 14 DIV, as shown in Figure 6.19a. In order to plot the relation between cells of low and high initial fluorescence, we calculated the mean of the initial fluorescence for all cells (Fig. 6.19b). This plot yields nearly a complementary image of Figure 6.19a, confirming the generation of waves and network oscillations in cells with low initial fluorescence.

6.3.4 Discussion

NMDA-evoked stimulation of temporal pH_i dynamics

We found that NMDA induced two kinds of changes in pH_i in hippocampal cell cultures from newborn rats which did depend on the age of the cell cultures. During the first two weeks *in vitro*, NMDA stimulated mainly an intracellular acidification while after 14 DIV we observed only a pH_i biphasic change characterized by a transient acidification followed by a longer lasting alkalinization.

Earlier studies have shown that the pH_i acid shift is related to glycolysis. Zhan et al. [34, 79] have found a biphasic change in pH_i: an initial transient alkaline shift followed by a long-lasting acid shift evoked by NMDA in rat hippocampal

slices. The acid shift was suppressed when glucose was substituted by pyruvate, i.e., when there was no substrate for glycolysis. Moreover, inhibition of glycolysis by fluoride also suppressed the acid shift. For another brain tissue, Brune et al. [80] have demonstrated that glutamate, aspartate and kainate induce an intracellular acidification in cultured rat cerebellar astrocytes. They elucidated that kainate-induced acidification is partly due to a concomitant intracellular Ca^{2+} rise, while the glutamate/aspartate-induced acidification is mainly due to the activation of the glutamate uptake system. This glutamate reuptake into astrocyte activates the glial Na^+-K^+ ATPase resulting in activation of glycolysis [24, 27]. Therefore, we interpret the NMDA-induced intracellular acidification found in our experiments as an increased activity of glycolysis.

It has been found that neuronal activity leads to an intracellular alkalinization. An increase in pH_i of glial cells was demonstrated to be induced by electrical stimulation [81] as well as extracellular K^+ induced depolarization [82]. This alkalinization occurred due to the activation of Na^+-HCO_3^- cotransport [82–84]. Hence, the alkalinization may be taken as an indicator for increased neuronal activity, either evoked by NMDA or K^+-addition.

KCN-evoked stimulation of temporal pH_i dynamics

Similar to NMDA stimulation, KCN application induced also different changes in pH_i that were age-dependent. A biphasic response (first acid shift, then alkalinization) was observed during the whole observation period (3-22 DIV). Starting from 14 DIV there was an additional spiking activity, superimposed on the alkaline phase. This spiking activity was only observed after KCN addition, i.e., after block of mitochondrial respiration. We therefore assume that this spiking activity is coupled to glycolysis. The fact, that the alkaline spikes are preceded by a short lasting acid shift supports this view. Obviously, an inceased glycolytic activity, represented by the acid shift, triggers the spikes. It is interesting to note that the biphasic response in pH_i to either KCN or NMDA addition is nearly identical. The only difference lies in the pH_i-spiking activity and generation of waves mainly after 14 DIV, when KCN is used. This indicates that the biphasic response is evoked by

increased neuronal activity, either via NMDA or via potassium induced depolarization of the cell membranes, whereas the spiking activity and the wave generation is due to block of mitochondria via cyanide. The blockage of mitochondrial activity obviously introduces some instability in the energy metabolism of the cells, leading to nonlinear dynamics in pH_i.

KCN-evoked pH_i waves and network oscillations

During the first two weeks of cultivation, KCN addition evoked only temporal changes in pH_i. However, after 14 DIV, there were additional spatio-temporal patterns. We observed propagating pH_i waves in hippocampal cultured cells stimulated by KCN. The waves mostly emerged at the middle of the cells and then expanded as a circular front. At some instances, the waves in a cluster of cells started nearly at the same time thus forming network oscillations.

Extracellular waves of concentration changes have been demonstrated earlier in the nervous system. Innocenti et al. [52] have shown that glutamate, which was released from stimulated cultured rat cortical astrocytes during Ca^{2+} signaling, propagated in the form of a circular wave. Newman [8] has found that ATP was released as a circular wave after a local mechanical stimulation in retinal astrocytes. In a numerical study of astrocytic networks, circular waves of ATP and Ca^{2+} with finite range of propagation are generated due to IP_3-dependent ATP release [85].

The pH_i waves, as reported in this work, differ from the previously reported ones. First, the propagating species are protons, whereas most of the other wave phenomena have been described for calcium ions in other brain tissues. Second, most of these waves propagate as intercellular waves, originating from intracellular calcium elevations, whereas the proton waves do not cross the cell membrane. The wave velocity of the proton waves (60-110 μm/s) is somewhat lager than that reported for calcium waves in other brain tissue (6-30 μm/s). Proton waves have been already reported to occur in neutrophil cells or in yeast extract as the result of oscillatory glycolysis [9, 10]. Since the pH_i-waves in the hippocampal cell cultures occurred only when mitochondrial respiration was blocked, we may suggest that these waves appearred as the result of altered glycolytic activity. In this case,

the propagation occurs solely in the cytoplasm whereas calcium waves require additional intracellular calcium stores. However, the particular mechanisms for pH_i-wave propagation remain to be elucidated.

The pH_i-wave traveled only on small spatial scales. In contrast, network oscillations of pH_i occurred over the whole cell cultures. These oscillations did not appear homogeneously, but occurred as spatial fluctuations with random distribution and varying frequency. They occurred only after 14 DIV, i.e., when the synaptic connections are established, giving raise to a functional neuronal network. Similar network oscillations in hippocampal slices with different frequencies have been reported for calcium [86].

In addition to the age-dependent change of pH_i, the initial pH_i, i.e., before addition of KCN or NMDA, showed variations within one cell culture. Generally, there were cells with either low or high initial pH_i. Similar results have been reported for neurons from immature or mature hippocampal neurons. Bevensee et al. [87] found that on average the pH_i of mature neurons are more alkaline. Intracellular variability of initial fluorescence in brain cells is not restricted to pH_i. Kasischke et al. used different initial NAD(P)H fluorescence in rat hippocampal slice preparations to distinguish between neurons and astrocytes. In our cell cultures, the number of cells with low initial pH_i markedly increased when the culture was older than 14 days. Since this is also the time point when waves and network oscillations appeared, we conclude that there is a correlation between the initial pH_i and generation of spatiotemporal pH_i -patterns.

The results of this work demonstrate that spatiotemporal pattern formation of certain time windows during the formation of neuronal networks. We may take this behavior as an indication that the waves play an important role at specific stages of neuronal network formation. The fact that these patterns are only visible when mitochondrial respiration is blocked by cyanide does not exclude that these patterns occur in vivo. The background fluorescence from mitochondrial NAD(P)H metabolism may be too high and thus mask the proton waves in the absence of cyanide. However, whether additional proton transport activities also affect the fluorescence signal has to be clarified in future work.

Chapter 7

Conclusion and outlook

Energy metabolism is important for every life. Experimental findings supported the concept of metabolic compartmentation in brains: most of glycolysis occurs in glia cells and provides lactate as a substrate for mitrocondrial respiration which mainly takes place in the neurons. Due to the limited resource of energy, brains optimize their neuronal network connections during early postnatal state in order to increase the efficiency of communication in the network. Hippocampus is a part of the brain which plays a major role in short term memory and spatial navigation and it is often used for study of brain energy metabolism.

Since both NAD(P)H and proton are also generated during glycolysis and subsequently consumed by mitrocondrial respiration, experiments on metabolism have been performed by fluorescence imaging of NAD(P)H and pH-sensitive dyes for proton measurement. Spatiotemporal patterns known as spiral and circular waves have been found in many kinds of biological excitable media. Investigations of glycolysis have revealed traveling NAD(P)H and proton waves in both cell extracts and living cells.

In the present thesis, we have reported a study of the energy metabolism during neuronal network formation (i.e., the first three weeks *in vitro*) in rat hippocampal cell cultures containing both intracellular neurons and glia cells. We utilized fluorescence imaging to detect changes of NAD(P)H and proton concentrations. To observe the immediate response of the cells, chemical stimulations (with the

neurotransmitter NMDA or the inhibitor of mitrocondrial respiration KCN) have been applied locally, i.e., close to the cells, using a nano-injector during the imaging process.

In the part of NAD(P)H imaging, NMDA induced a transient overshoot of NAD(P)H fluorescence. During the first 3 weeks *in vitro*, changes of NMDA-evoked NAD(P)H signaling progressed as a biphasic pattern (the response was minimal at day 7 and 16) that reproduced earlier findings of other groups about developmental changes of population spike amplitudes or glutamate release in young rats. KCN evoked a transient increase in NAD(P)H fluorescence. In contrast to the case of NMDA, the NAD(P)H response to KCN increased with the age of the first two weeks and decayed at the higher age, without a biphasic pattern. In the presence of KCN, the progressive change of NMDA-evoked NAD(P)H fluorescence still exhibited a biphasic pattern which implied that the NMDA-evoked response of the energy metabolism was mainly due to an increase in the glycolytic activity.

In the part of intracellular pH (pH_i) imaging, NMDA induced two kinds of temporal dynamics of pH_i, i.e., an intracellular acidification or a biphasic (first acid, then alkaline) change. We interpret the NMDA-induced intracellular acidification as an increased activity of glycolysis. Blocking mitochondrial respiration by cyanide induced temporal dynamics of pH_i as well as propagating waves or network oscillations. During the whole observation period (3-22 DIV), most of observed cells showed the biphasic responses (first acid shift, then alkalinization) while some cells exhibited alkalinization only. Interestingly, traveling waves or network oscillations, which mainly occurred after 14 DIV, superimposed the biphasic changes. We observed two forms of propagating wave fronts. A circular wave emerged at the middle of the cell while a crescentic wave started near one edge of the cell.

We have presented an investigation of the energy metabolism in hippocampal cell cultures using chemical applications. Future research can be performed by means of electrical stimuli. For hippocampal slices, it has been found earlier that the electrical stimuli evoked different changes of NADH fluorescence depending on the observed location on the slices and it was suggested that neurons and glia cells

provided different responses to the electrical stimuli. Unlike the slices where the two kinds of cells possibly overlay each other, neurons and glia cells in cell cultures can be easier distinguished from each other. For example, it is possible to generate cell cultures of only neurons or glia cells. Therefore, the electrical evoked response from different cells are possibly clearer identified in the case of cell cultures.

Appendix A

IDL program

The programs for calculating an average intensity, image enhancement and different images are presented below. These programs were written by Ulrich Storb and Chaiya Luengviriya from Biophysics Group, Otto-von-Guericke University of Magdeburg, in IDL (Interactive Data Language).

A.1 Average intensity

pro intensity_multisub_freeshape, colorimg=colorimg, grayimg=grayimg, labeledimg=labeledimg,

listimg=listimg, intensityfile=intensityfile

if not keyword_set(colorimg) then begin

Filename = DIALOG_PICKFILE(TITLE = 'Select the image with color AOIs', FILTER =

'*.bmp', PATH = '.')

endif else begin

filename = colorimg

endelse

print,Filename

pfad = drivename(Filename(0))+dirname(Filename(0))

print,'Image folder is ',pfad

old_dir = ''

CD,pfad,CURRENT=old_dir

dimension = QUERY_bmp (Filename, Info)

```
dimension_x = Info.DIMENSIONS(0)

dimension_y = Info.DIMENSIONS(1)

print, dimension_x,dimension_y

image = READ_bmp(Filename)

SET_PLOT, 'WIN'

WINDOW, 0, XSIZE = dimension_x , YSIZE = dimension_y , TITLE = 'original image'

WSET, 0

TV, image,TRUE = 1

imageAOIs = bytarr(dimension_x,dimension_y)

for x = 0, dimension_x -1 do begin

for y = 0, dimension_y -1 do begin

if NOT( (image(0,x,y) eq image(1,x,y)) and (image(0,x,y) eq image(2,x,y)) ) then begin

imageAOIs(x,y) = 1

endif

endfor

endfor

group = group_label_long(image=imageAOIs,xsize=dimension_x,ysize=dimension_y,grayvalue=1)

nrofgroup = MAX(group)

countmember = intarr(nrofgroup+1)

edgeAOIs = intarr(nrofgroup+1)

pos_number = intarr(nrofgroup+1)

AOIs = where(group eq 1,count)

countmember[1] = count

edgeAOIs[0] = 0

edgeAOIs[1] = countmember[1]

for i = 2, nrofgroup do begin

AOI = where(group eq i,count)

countmember[i] = count

AOIs = [AOIs, AOI]

edgeAOIs[i] = edgeAOIs[i-1] + countmember[i]

endfor
```

```
if not keyword_set(grayimg) then begin

Filename = DIALOG_PICKFILE(TITLE = 'Select an gray-scale image to assign label the AOI',

FILTER = '*.tif', PATH = '.')

endif else begin

filename = grayimg

endelse

image2 = read_tiff(filename)

envelopAOIs = envelop(image= imageAOIs,xsize=dimension_x,ysize=dimension_y)

enveloppoints = where(envelopAOIs eq 1)

imageAOIs(enveloppoints) = 1

envelopAOIs = envelop(image= imageAOIs,xsize=dimension_x,ysize=dimension_y)

enveloppoints2 = where(envelopAOIs eq 1)

enveloppoints = [enveloppoints,enveloppoints2]

image2_color = bytarr(3,dimension_x,dimension_y)

image2_color0 = image2

image2_color0(enveloppoints) = 255

image2_color(0,*,*) = image2_color0

image2_color1 = image2

image2_color1(enveloppoints) = 0

image2_color(1,*,*) = image2_color1

image2_color2 = image2

image2_color2(enveloppoints) = 0

image2_color(2,*,*) = image2_color2

SET_PLOT, 'WIN'

WINDOW, 1, XSIZE = dimension_x , YSIZE = dimension_y , TITLE = 'AOIs with label'

WSET, 1

TV, image2_color,true=1

Rotateimage2_color = bytarr(3,dimension_x,dimension_y)

Rotateimage2_color(0,*,*) = ROTATE(REFORM(image2_color(0,*,*)), 7)

Rotateimage2_color(1,*,*) = ROTATE(REFORM(image2_color(1,*,*)), 7)

Rotateimage2_color(2,*,*) = ROTATE(REFORM(image2_color(2,*,*)), 7)
```

```
WINDOW, 3, XSIZE = dimension_x , YSIZE = dimension_y , TITLE = 'AOIs with label(flip)'

WSET, 3

TV, Rotateimage2_color ,true=1

for i = 1, nrofgroup do begin

pos_number = AOIs[(countmember(i))/2 + edgeAOIs[i-1]]

pos_x = pos_number mod dimension_x

pos_y = fix(pos_number/dimension_x)


WSET, 1

XYOUTS, pos_x, pos_y, STRCOMPRESS(i, /REMOVE_ALL), /DEVICE

pos_y = dimension_y - pos_y

WSET, 3

XYOUTS, pos_x, pos_y, STRCOMPRESS(i, /REMOVE_ALL), /DEVICE

endfor

if not keyword_set(labeledimg) then begin

file = DIALOG_PICKFILE(TITLE = 'Select a name to save the image with the AOI label',

FILTER = '*.bmp', PATH = '.')

endif else begin

file = labeledimg

endelse

WSET, 1

WRITE_BMP, file + '.bmp', TVRD(true=1),/RGB

WSET, 3

WRITE_BMP, file + '_flip.bmp', TVRD(true=1),/RGB

SET_PLOT, 'WIN'

WINDOW, 2, XSIZE = dimension_x , YSIZE = dimension_y , TITLE = 'AOIs without label'

WSET, 2

TV, image2_color,true=1

WRITE_BMP, file + '_nolabel.bmp', image2_color,/RGB

if not keyword_set(listimg) then begin

file = DIALOG_PICKFILE(/READ,FILTER='*.txt',PATH='.', $
```

TITLE='Select list file of movies to load')

endif else begin

file = listimg

endelse

IF (file(0) EQ '') THEN RETURN

pfad = drivename(file(0))+dirname(file(0))

print,'Image folder is ',pfad

old_dir = ''

CD,pfad,CURRENT=old_dir

if not keyword_set(intensityfile) then begin

int_file = DIALOG_PICKFILE(TITLE ='Save average intersity to')

endif else begin

int_file = intensityfile

endelse

OPENR,unit,file(0),/GET_LUN

scenes = read_all_lines(unit)

CLOSE,unit

FREE_LUN,unit

nroflines = size(scenes)

nroflines = nroflines(1)

OPENW, Unit, int_File, /GET_LUN

intensity = fltarr(nrofgroup)

FOR i=0, nroflines-1 DO BEGIN

print,i

inputfile = pfad + scenes[i]

image = READ_TIFF(inputfile)

FOR j = 0, nrofgroup-1 DO BEGIN

pict = image(AOIs(edgeAOIs[j]:edgeAOIs[j+1]-1))

intensity[j] = MEAN(pict)

ENDFOR

format2 = '(I6,' + string(nrofgroup) + 'F10.2)'

PRINTF, Unit,format=format2, i,intensity

ENDFOR

CLOSE, Unit

FREE_LUN, Unit

normalize, infile = int_file, nroflines = nroflines, nrofgroup = nrofgroup

PRINT,'done'

end

A.2 Contrast enhancement

pro contrastimgs_overall,individual=individual

file = DIALOG_PICKFILE(/READ,FILTER='*.txt',PATH='.', $

TITLE='Select list file of movies to load')

IF (file(0) EQ '') THEN RETURN

pfad = drivename(file(0))+dirname(file(0))

print,'Image folder is ',pfad

old_dir = ''

CD,pfad,CURRENT=old_dir

OPENR,unit,file(0),/GET_LUN

scenes = read_all_lines(unit)

CLOSE,unit

FREE_LUN,unit

nroflines = size(scenes)

nroflines = nroflines(1)

IF not KEYWORD_SET(outdir) THEN BEGIN

outdir = DIALOG_PICKFILE(/READ,FILTER='*.*',PATH='.',TITLE='Select a folder to save

result images')

outdir = drivename(outdir) + dirname(outdir)

IF (outdir EQ '') THEN RETURN

print,'destination folder of is ', outdir

ENDIF

```
ok = QUERY_TIFF (pfad + scenes[0], Info)

xsize = info.dimensions(0)

ysize = info.dimensions(1)

outfile_bytscl = outdir + 'bytscl'

if keyword_set(individual) then begin

for j = 0 , nroflines -1 do begin

print,j

image = read_tiff(pfad + scenes[j])

img = bytscl(image)

write_tiff, outfile_bytscl + scenes(j), img ,compression=1

endfor

endif else begin

minarr = bytarr(nroflines)

maxarr = bytarr(nroflines)

for i = 0 , nroflines -1 do begin

print,i

image = read_tiff(pfad + scenes[i])

minarr[i] = min(image,max=maxi)

maxarr[i] = maxi

endfor

minminall = min(minarr,max=maxminall)

minmaxall = min(maxarr,max=maxmaxall)

countpopmin = intarr(256)

countpopmax = intarr(256)

for i = minminall, maxminall do begin

search = where(minarr eq i,count)

countpopmin[i] = count

endfor

for i = minmaxall, maxmaxall do begin

search = where(maxarr eq i,count)

countpopmax[i] = count
```

```
endfor

window,0 ,title= 'graph of minima and amount of images'

wset,0

plot,countpopmin

window,1 ,title= 'graph of maxima and amount of images'

wset,1

plot,countpopmax

print,' '

text = 'overall mininum and maximum : ' + string(minminall,format='(I3.3)')+ ', '

+ string(maxmaxall,format='(I3.3)') +', take them? If not, insert them in the command line'

ok = dialog_message(/question, text)

minall = minminall

maxall = maxmaxall

if ok eq 'No' then begin

print,'Please insert the minimum.'

read,minall

print,'Please insert the maximum.'

read,maxall

endif

for i = 0 , nroflines -1 do begin

print,i

image = read_tiff(pfad + scenes[i])

img = bytscl(image, min=minall, max=maxall)

write_tiff, outfile_bytscl + scenes(i), img ,compression=1

endfor

endelse

print,'done'

end
```

A.3   Difference of images

```
Pro diff_delay_subvolume_showplus, skip = skip,$

delay = delay,$

CIRCULAR = circular,$

z0 = z0,$

zn = zn,$

slicewise = slicewise,$

whitefront = whitefront, $

shift_min = shift_min, $

shift_max = shift_max,$

median_width=median_width,$

theshold_plus=theshold_plus,$

collective_width=collective_width

if keyword_set(collective_width) then begin

n=collective_width

kernal = MAKE_ARRAY([n,n],/float, VALUE=1.0)

endif

file = DIALOG_PICKFILE(/READ,FILTER='*.txt',PATH='.', $

TITLE='Select list file of movies to load')

IF ( file(0) EQ '' ) THEN RETURN

pfad = drivename(file(0))+dirname(file(0))

print,'Image folder is ',pfad

old_dir = ''

CD,pfad,CURRENT=old_dir

OPENR,unit,file(0),/GET_LUN

scenes = read_all_lines(unit)

CLOSE,unit

FREE_LUN,unit

nroflines = size(scenes)

nroflines = nroflines(1)
```

```
outdir = DIALOG_PICKFILE(/READ,FILTER='*.*',PATH='.',TITLE='Select Folder to save
result-movie ')

IF ( outdir EQ '' ) THEN RETURN

print,'destination folder is ',drivename(outdir) + dirname(outdir)

image = pfad+scenes(0)

print,image

ok = QUERY_TIFF(image,Info)

xsize = Info.DIMENSIONS(0)

ysize = Info.DIMENSIONS(1)

IF (KEYWORD_SET(circular)) THEN BEGIN

diam = MIN([xsize,ysize])

abschneiden = FLTARR(xsize,ysize)

FOR ii = 0,xsize-1 DO BEGIN

FOR jj = 0,ysize-1 DO BEGIN

abschneiden(ii,jj) = (ii-xsize/2)*(ii-xsize/2)+(jj-ysize/2)*(jj-ysize/2)

ENDFOR

ENDFOR

aussenindex = WHERE(abschneiden GE (diam/2-circular) *(diam/2-circular))

innenindex = WHERE(abschneiden LT (diam/2-circular) *(diam/2-circular))

no_of_valid_points = SIZE(innenindex)

ENDIF

IF NOT(KEYWORD_SET(skip)) THEN skip = 0

IF NOT(KEYWORD_SET(delay)) THEN delay = 1

IF NOT(KEYWORD_SET(z0)) THEN z0 = 0

IF NOT(KEYWORD_SET(zn)) THEN zn = info.NUM_IMAGES - 1

mi = fltarr(zn - z0 + 1)

ma = fltarr(zn - z0 + 1)

films1 = FLTARR(xsize,ysize)

films2 = FLTARR(xsize,ysize)

diff = FLTARR(xsize,ysize,info.NUM_IMAGES)

j = delay
```

```
While (j LT nroflines) DO BEGIN

print, 'diff of image: ',scenes(j),' and' ,scenes(j - delay)

inputfile1 = pfad+scenes(j)

inputfile2 = pfad+scenes(j - delay)

outfile = drivename(outdir) + dirname(outdir)+'diff'+ STRTRIM(delay,2) + scenes(j)

FOR i = z0,zn DO BEGIN

films1 = FLOAT(READ_TIFF(inputfile1,IMAGE_INDEX=i))

films2 = FLOAT(READ_TIFF(inputfile2,IMAGE_INDEX=i))

if keyword_set(median_width) then begin

films1 = median(films1,median_width)

films2 = median(films2,median_width)

endif

diff(*,*,i) = films1 - films2

slice = diff(*,*,i)

if keyword_set(theshold_plus) then begin

slice(where(slice lt theshold_plus)) = 0

endif

if keyword_set(collective_width) then begin

slice_conv = convol(slice,kernal)/(n)

slice(where(slice_conv lt theshold_plus)) = 0

endif

If (keyword_set(circular)) Then begin

valid_points = slice(innenindex)

endif else begin

valid_points = slice

endelse

mi[i-z0] = MIN(valid_points)

ma[i-z0] = MAX(valid_points)

ENDFOR

mi_whole = MIN(mi)

ma_whole = MAX(ma)
```

```
print, mi_whole,ma_whole

IF (KEYWORD_SET(shift_min)) THEN mi_whole = shift_min

IF (KEYWORD_SET(shift_max)) THEN ma_whole = shift_max

FOR k= z0,zn DO BEGIN

slice = diff(*,*,k)

IF ( keyword_set(slicewise)) THEN BEGIN

slice = BYTSCL(slice, MIN=mi(k - z0), MAX=ma(k-z0))

endif else begin

slice = BYTSCL(slice, MIN=mi_whole, MAX=ma_whole)

endelse

IF ( keyword_set(whitefront)) THEN BEGIN

slice = 255 - slice

ENDIF

IF ( k eq z0 ) THEN BEGIN

WRITE_TIFF,outfile, slice,COMPRESSION=1

ENDIF ELSE BEGIN

WRITE_TIFF,outfile, slice,/APPEND,COMPRESSION=1

ENDELSE

ENDFOR

j = j + 1 + skip

ENDWHILE

print,'done'

END
```

References

[1] A.I. Zotin. *Thermodynamic Bases of Biological Processes*. Walter de Gruyter, Berlin, 1997.

[2] M.A. Hofman. Energy metabolism, brain size and longevity in mammals. *Q Rev Biol.*, 58(4):495–512, 1983.

[3] S.B. Laughlin and T.J. Sejnowski. Communication in neuronal networks. *Science*, 301:1870–1874, 2003.

[4] W. Singer. Development and plasticity of cortical processing architectures. *Science*, 270(5237):758–764, 1995.

[5] M. E. Harris-White, S. A. Zanotti, S. A. Frautschy, and A. C. Charles. Spiral intercellular calcium waves in hippocampal slice cultures. *The Journal of Neurophysiology*, 79:1045–1052, 1998.

[6] J. Lechleiter, S. Girard, E. Peralta, and D. Clapham. Spiral calcium wave propagation and annihilation in *xenopus laevis* oocytes. *Science*, 252:123–126, 1991.

[7] K.J. Tomchik and P.N. Devreotes. Adenosine 3v,5v-monophosphate waves in *dictyostelium discoideum*: a demonstration by isotope dilutionfluorography. *Science*, 212:443–446, 1981.

[8] E.A. Newman. Propagation of intercellular calcium waves in retinal astrocytes and Müller cells, the journal of neuroscience. *The Journal of Neuroscience*, 21:2215–2223, 2001.

[9] T. Mair and S.C. Müller. Travelling NADH and proton waves during oscillatory glycolysis in vitro. *J. Biol. Chem*, 271:627–630, 1996.

[10] H.R. Petty, R.G. Worth, and A.L. Kindzelskii. Imaging sustained dissipative patterns in the metabolism of individual living cells. *Phys. Rev. Lett*, 84:2754–2757, 2000.

[11] E. Dulos J. Boissonade P.D. Kepper S.C. Muller S. Bagyan, T. Mair. Glycolytic oscillations and waves in an open spatial reactor: impact of feedback regulation of phosphofructokinase. *Biophys. Chemist*, 116:67–76, 2005.

[12] S.C. Müller. Experiments on Excitation Waves, In: Nonlinear Physics of Complex Systems - Current Status and Future Trends edited by J. Parisi and S.C. Müller and W. Zimmermann. *Springer verlag, Berlin*, pages 133–148, 1996.

[13] J.J. Tyson and J.P Keener. Singular perturbation theory of traveling waves in excitable media. *Physica D*, 32:327–361, 1988.

[14] O. Steinbock, P. Kettunen, and K. Showalter. Chemical wave logic gates. *J. Phys. Chem*, 100:18970–18975, 1996.

[15] T. Mair and S.C. Müller. Propagating waves of biological activity. *Res. Devel. Biophys. Chem*, 1:105–121, 2000.

[16] J. Gorecki, J. N. Gorecka, K. Yoshikawa, Y. Igarashi, and H. Nagahara. Sensing the distance to a source of periodic oscillations in a nonlinear chemical medium with the output information coded in frequency of excitation pulses. *Physical review E*, 72:046201–046207, 2005.

[17] V. G. Fast and A. G. Kleber. Role of wavefront curvature in propagation of cardiac impulse. *Cardiovascular Research*, 33:258–271, 1997.

[18] A.C. Skanes, R. Mandapati, O. Berenfeld, J.M. Davidenko, and J. Jalife. Spatiotemporal periodicity during atrial fibrillation in the isolated sheep heart. *Circulation*, 98:1236–1248, 1998.

[19] K.H.W.J. Ten Tusscher, R. Hren, and A.V. Panfilov. Organization of ventricular fibrillation in the human heart. *Circulation Research*, 100:e87–e101, 2007.

[20] S. Schuchmann, R. Kovacs, O. Kann, U. Heinemann, and K. Buchheim. Monitoring NAD(P)H autofluorescence to assess mitochondrial metabolic functions in rat hippocampal-entorhinal cortex slices. *Brain research protocols*, 7:267–276, 2001.

[21] C.W. Shuttleworth, A.M. Brennan, and J.A. Connor. NAD(P)H fluorescence imaging of postsynaptic neuronal activation in murine hippocampal slices. *Journal of Neuroscience*, 23(8):3196–3208, 2003.

[22] K.A. Kasischke, H.D Vishwasrao, P.J. Fisher, W.R. Zipfel, and W.W. Webb. Neuronal activity triggers neuronal oxidative metabolism followed by astrocytic glycolysis. *Science*, 305:99–103, 2004.

[23] P.J. Magistretti and L.Pellerin. Astrocytes couple synaptic activity to glucose utilization in the brain. *News Physio. Sci.*, 14:177–182, 1999.

[24] L.Pellerin and P.J. Magistretti. Let there be (NADH) light. *Science*, 305:50–52, 2004.

[25] A. Mayevsky, S. Nioka, V.H. Subramanian, and B. Chance. Brain oxidative metabolism of the newborn dog: correlation between 31P NMR spectroscopy and pyridine nucleotide redox state. *J. Cereb Blood Flow Metab.*, 8(2):201–207, 1988.

[26] A. Mayevsky and G. G. Rogatsky. Mitochondrial function in vivo evaluated by NADH fluorescence: from animal models to human studies. am j physiol cell physiol. *Physiol Cell Physiol*, 292(2):C615–640, 2007.

[27] L.Pellerin and P.J. Magistretti. Glutamate uptake into astrocytes stimulates aerobic glycolysis: a mechanism coupling neuronal activity to glucose utilization. *Proc. Natl. Acad. Sci. USA.*, 91:10625–10629, 1994.

[28] M.W. King. Website. `http://dwb4.unl.edu/Chem/CHEM869P/CHEM869PLinks/webindstate.edu/thcme/mwking/glycolysis.html`.

[29] P. Brodal. *The Central Nerve System* . Oxford University Press, New York, 1998.

[30] P.G. Haydon. Glia: listening and talking to the synapese. *Nat. Rev. Neurosci.*, 2:185–193, 2001.

[31] M. Nedergaard, B. Ronsom, and S.A. Goldman. New roles for astrocytes: redefining the functional architeture of the brain. *Trends Neurosci.*, 26:523–530, 2003.

[32] Website. `http://www.alzheimer-adna.com/Images/hippocampus.gif`.

[33] Website. `www.biomedcentral.com`.

[34] R.Z. Zhan, N. Fujiwara, T. Yamakura, K. Taga, S. Fukuda, H. Endoh, and K. Shimoji. NMDA induces a biphasic change in intracellular pH in rat hippocampal slices. *Brain Research*, 760:179–186, 1997.

[35] K.J. Collard, R. Edwards, and Y. Liu. Changes in synaptosomal glutamate release during postnatal development in the rat hippocampus and cortex. *Developmental Brain Research.*, 71:37–43, 1993.

[36] I.E. Kudryashov, M.V. Onufriev, I.V. Kudryashova, and N.V. Gulyaeva. Periods of postnatal maturation of hippocampus: synaptic modifications and neuronal disconnection. *Developmental Brain Research*, 132:113–120, 2001a.

[37] I.E. Kudryashov and I.V. Kudryashova. Ontogeny of synaptic transmission in the rat hippocampus. *Brain Research*, 892:263–268, 2001b.

[38] J.M. Flesselles, A. Belmonte, and V. Gáspár. Dispersion relation for waves in the Belousov-Zhabotinsky reaction. *J. Chem. Soc. Faraday Trans.*, 94:851–855, 1998.

[39] A.F. Taylor, V. Gáspár, B. R. Johnson, and S.K. Scott. Analysis of reaction-diffusion waves in the ferroin-catalysed Belousov-Zhabotinsky reaction. *Phys. Chem. Chem. Phys.*, 1:4595–4599, 1999.

[40] V.S. Zykov. Analytical evaluation of the dependence of the speed of an excitation wave in a two-dimension excitable medium on the curvature of its front. *Biophysics*, 25:906–911, 1980.

[41] J.P. Keener and J.J. Tyson. Spiral waves in the Belousov-Zhabotinskii reaction. *Physica D*, 21:307–324, 1986.

[42] P. Foerster, S.C. Müller, and B. Hess. Curvature and propagation velocity of chemical waves. *Science*, 241:685–687, 1988.

[43] S.C. Müller and T. Plesser. Spiral waves dynamics. In: Chemical waves and patterns, edited by R. Kapral and K. Showalter. *Kluwer Academic Publishers, London*, pages 57–92, 1994.

[44] S.C. Müller, T. Plesser, and B. Hess. The structure of the core of the spiral wave in the Belousov-Zhabotinsky reaction. *Science*, 230:661–663, 1985.

[45] T. Plesser, S.C. Müller, and B. Hess. Spiral wave dynamics as a function of proton concentration in the ferroin-catalyzed Belousov-Zhabotinsky reaction. *J. Phys. Chem.*, 94:7501–7507, 1990.

[46] G.S. Skinner and H.L. Swinney. Periodic to quasiperiodic transition of chemical spiral rotation. *Physica D*, 48:1–16, 1991.

[47] Zs. Nagy-Ungvárai, J. Ungvárai, and S.C. Müller. Complexity in spiral wave dynamics. *Chaos*, 3:15–19, 1993.

[48] G. Li, Q. Ouyang, V. Petrov, and H.L. Swinney. Transition from simple rotating chemical spirals to meandering and traveling spirals. *Phys. Rev. Lett.*, 77:2105–2108, 1996.

[49] N. Manz, B.T. Ginn, and O. Steinbock. Meandering spiral waves in the 1,4-cyclohexanedione Belousov-Zhabotinsky system catalyzed by $Fe[batho(SO_3)_2]_3^{4-/3-}$. *J. Phys. Chem. A*, 107:11008–11012, 2003.

[50] V.S. Zykov. *Simulation of Wave Processes in Excitable Media*. Manchester University Press, Manchester, 1987.

[51] S. Grill, V. S. Zykov, and S.C. Müller. Spiral wave dynamics under pulsatory modulation of excitability. *J. Phys. Chem.*, 100:19082–19088, 1996.

[52] B. Innocenti, V. Parpura, and P.G. Haydon. Imaging extracellular waves of glutamate during calcium signaling in cultured astrocytes. *Journal of Neuroscience*, 20:1800–1808, 2000.

[53] F. Siegert and C.J. Weijer. Digital image processing of optical density wave propagation in *dictyostelium discoideum*. *J. Cell Sci*, 93:325–335, 1989.

[54] M.A. Dahlem and S.C. Müller. Self-induced splitting of spiral-shaped spreading depression waves in chicken retina. *Exp. Brain Res.*, 115:319–324, 1997.

[55] S.C. Müller, T. Mair, and O. Steinbock. Traveling waves in yeast extract and in cultures of *dictyostelium discoideum*. *Biophys. Chem.*, 72:37–47, 1998.

[56] R.A. Gray, A.M. Pertsov, and J. Jalife. Spatial and temporal organization during cardiac fibrillation. *Nature (London)*, 392:75–78, 1998.

[57] A. Ghosh and B. Chance. Oscillations of glycolytic intermediates in yeast cells. *Biochem. Biophys. Res. Commun.*, 16:174–181, 1964.

[58] A. Goldbeter and R. Lefever. Dissipative structures for an allosteric model. application to glycolytic oscillations. *Biophys. J.*, 12:1302–1315., 1972.

[59] L.N. Duysens and J. Amesz. Fluorescence spectrophotometry of reduced phosphopyridine nucleotide in intact cells in the near-ultraviolet and visible region. *Biochim. Biophys. Acta*, 24:19–26, 1957.

[60] B. Chance, B. Hess, and A. Betz. DPNH oscillations in a cell-free extract of S. carlsbergensis. *Biochem. Biophys. Res. Commun.*, 16:182–187, 1964.

[61] B. Hess, K. Brand, and K. Pye. Continuous oscillations in a cell-free extract of S. carlsbergensis. *Biochem. Biophys. Res. Commun.*, 23:102–108, 1966.

[62] A.K. Poulsen, M.O. Petersen, and L.F. Olsen. Single cell studies and simulation of cell-cell interactions using oscillating glycolysis in yeast cells. *Biophys. Chem.*, 125:275–280, 2007.

[63] R. Frenkel. Reduced diphosphopyridine nucleotide oscillations in cellfree extracts from beef heart. *Arch. Biochem. Biophys.*, 115:112–121, 1966.

[64] K. Tornheim and J.M. Lowenstein. The purine nucleotide cycle. 3. oscillations in metabolite concentrations during the operation of the cycle in muscle extracts. *J. Biol. Chem.*, 248:2670–2677, 1973.

[65] B. O'Rourke, B.M. Ramza, D.N. Romashko, and E. Marban. Metabolic oscillations in heart cells. *Adv. Exp. Med. Biol.*, 382:165–174, 1995.

[66] K.H. Ibsen and K.W. Schiller. Oscillations of nucleotides and glycolytic intermediates in aerobic suspensions of ehrlich ascites tumor cells. *Biochim. Biophys. Acta*, 131:405–407, 1967.

[67] H.F. Chou, N. Berman, and E. Ipp. Oscillations of lactate released from islets of langerhans: evidence for oscillatory glycolysis in beta-cells. *Am. J. Physiol*, 262:E800–E805, 1992.

[68] B.E. Corkey, K. Tornheim, J.T. Deeney, M.C. Glennon, J.C. Parker, Matschinsky, N.B. Ruderman, and M. Prentki. Linked oscillations of free Ca^{2+} and the ATP/ADP ratio in permeabilized RINm5F insulinoma cells supplemented with a glycolyzing cell-free muscle extract. *J.Biol. Chem.*, 263:4254–4258, 1988.

[69] T.G. Chasteen. Website. `http://www.shsu.edu/chemistry/ chemiluminescence/JABLONSKI.html`.

[70] Website. `http://probes.invitrogen.com/handbook/`.

[71] K. Braun and M. Segal. Fmrp-involvement in the formation of synaptic connections among cultured hippocampal neurons. *Cerebral Cortex.*, 10:1045–1052, 2000.

[72] Carl Zeiss Advanced Imaging Microscopy. *LSM 510 and LSM 510 META Laser Scanning Microscopes.* 2002.

[73] J. E. Bresenham. Algorithm for computer control of a digital plotter. *IBM Systems Journal*, 4:25–30, 1965.

[74] S.A. Lipton and S.B. Kater. Neurotransmitter regulation of neuronal outgrowth plasticity and survival. *TINS.*, 12:265–270, 1989.

[75] O. Kann, S. Schuchmann, K. Buchheim, and U. Heinemann. Coupling of neuronal activity and mitochondrial metabolism as revealed by NAD(P)H fluorescence signals in organotypic hippocampal slice cultures of the rat. *Neuroscience*, 119:87–100, 2003.

[76] M. Gruss, K. Braun, J.U. Frey, and V. Korz. Maternal separation during a specific postnatal time window prevents reinforcement of hippocampal long-term potentiation in adolescent rats. *Neuroscience*, 152:1–7, 2008.

[77] K. Yamane, K. Yokono, and Y. Okada. Anaerobic glycolysis is crucial for the maintenance of neural activity in guinea pig hippocampal slices. *J. of Neuroscience methods*, 103:163–171, 2000.

[78] S. Kahlert and G. Reiser. Requirement of glycolytic and mitochondrial energy supply for loading of Ca^{2+} stores and InsP3-mediated Ca^{2+} signaling in rat hippocampus astrocytes. 61:409–420, 2000.

[79] R.Z. Zhan, N. Fujiwara, E. Tanaka, and K. Shimoji. Intracellular acidification induced by membrane depolarization in rat hippocampal slices: roles of intracellular Ca^{2+} and glycolysis. *Brain Research*, 780:86–94, 1998.

[80] T. Brune and J.W. Deitmer. Deitmer, intracellular acidification and Ca^{2+} transients in cultured rat cerebellar astrocytes evoked by glutamate agonists and noradrenaline. *Glia*, 14:153–161, 1995.

[81] M. Chesler and R.P. Kraig. Intracellular pH of astrocytes increases rapidly with cortical stimulation. *American Journal of Physiology*, 253:22–24, 1987.

[82] I.I. Grichtchenko and M. Chesler. Depolarization-induced alkalinization of astrocytes in gliotic hippocampal slices. *Neuroscience*, 62:1071–1078, 1994.

[83] G. Boyarsky, B. Ransom, W.R. Schlue, M.B. Davis, and W.F. Boron. Intracellular pH regulation in single cultured astrocytes from rat forebrain. *Glia*, 8:241–248, 1993.

[84] N. Brookes and R.J. Turner. K$^+$-induced alkalinization in mouse cerebral astrocytes mediated by reversal of electrogenic Na$^+$-HCO$_3^-$-cotransport. *American Journal of Physiology*, 267:C1633–C1640, 1994.

[85] M. Stamatakis and N.V. Mantzaris. Modeling of ATP-mediated signal transduction and wave propagation in astrocytic cellular networks. *Journal of Theoretical Biology*, 241:649–668, 2006.

[86] J.W. Dani, A. Chernjavsky, and S.J. Smith. Neuronal activity triggers calcium waves in hippocampal astrocyte networks. *Neuron*, 8:429–440, 1992.

[87] M.O. Bevensee, T.R. Cummins, G.G. Haddad, W.F. Boron, and G. Boyarsky. pH regulation in single CA1 neurons acutely isolated from the hippocampi of immature and mature rats. *Journal of Physiology*, 494:315–328, 1996.

Curriculum Vitae

Personal Details

Name:	Jiraporn Luengviriya
Date of Birth:	13 August 1972
Place of Birth:	Suphanburi, Thailand
Nationality:	Thai

School education

1985–1987:	Upper Primary school, Sa-Nguan Ying, Suphanburi, Thailand
1988–1990:	Upper Secondary school, Sa-Nguan Ying, Suphanburi, Thailand

University education

1991-1994:	Study of physics: Chulalongkorn University, Bangkok, Thailand
1995:	Bachelor of Science (Physics)
1995-1997:	Scientist, Thailand Institute of Scientitic and Technological Research
1997-2000:	Study of physics: Mahidol University, Bangkok, Thailand
2001:	Master of Science (Physics)
	Title of thesis : Laser-Induced Fluorescence Spectrum of Normal and Cancer Breast Tissue
2001-2003:	Lecturer, Department of Industrial Physics and Medical Instrumentation, King Mongkut's University of Technology, North Bangkok, Thailand
2003-2008:	PhD. project: Biophysics Group, Otto-von-Guericke University, Magdeburg, Germany
	Title of thesis : Spatiotemporal metabolic organization during development of brain cell cultures